

Connie Iren Senland Fidje

Corrosion and Tribology Effects on Coatings for Retractable Bow Foils for Ships

June 2019



Norwegian University of
Science and Technology

Corrosion and Tribology Effects on Coatings for Retractable Bow Foils for Ships

Connie Iren Senland Fidje

Material Science and Engineering

Submission date: June 2019

Supervisor: Nuria Espallargas

Co-supervisor: Roy Johnsen
Erlend Vastveit Nærland

Norwegian University of Science and Technology
Department of Mechanical and Industrial Engineering

Preface

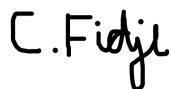
This thesis is written to obtain evaluation in the course TMM4960. The thesis is performed as a part of the Master of Science in Material Science and Engineering at Norwegian University of Science and Technology (NTNU) in Trondheim. The work was performed during spring semester 2019, between January and June.

I would first of all like to thank my supervisor Nuria Espallargas and my co-supervisor Roy Johnsen for providing me guidance and support throughout this semester. I would also like to thank co-supervisor Erlend Vastveit Nærland for his encouragement and continuously following up my work.

Laboratory work at Sealab NTNU and at the Tribology lab at NTNU were performed in association with this thesis. I would like to thank Cristian Torres Rodriguez for the help he has provided me throughout corrosion and tribology experiments conducted. I would also like to thank Wahyu Wijanarko and Hamid Khanmohammadi for interesting discussions and guidance at the Tribology lab.

Finally, I would like to show my gratitude to Åmund Hognestad and my friends and family for giving me support and encouragement.

Trondheim, 11. June 2019.

A handwritten signature in black ink that reads "C. Fidje". The letters are cursive and slightly slanted to the right.

Connie Iren Senland Fidje

Abstract

The concept of foils as a method of increasing performance of sea-faring vessels is well known. However, due to challenges resulting from having a permanent fixed foil attached to the hull, the concept has not seen much use. Solutions to these challenges have been highly sought after, as the potential fuel savings marine vessels will experience are significant. A retractable foil system is currently under development by Wavefoil AS. By using a power screw and nut to extend and retract the foils, Wavefoil intends to solve many of these challenges.

A xylan coated 25 Cr stainless steel (SDSS) power screw with a connecting nickel-aluminium bronze (NAB) nut will provide the translatory movement of the foils. The SDSS power screw and NAB nut will act as sliding surfaces in seawater and will be prone to corrosion and wear degradation. The main objective of this thesis is to provide an insight into the electrochemical and mechanical degradation the materials are facing during operation. The properties of SDSS and NAB have previously been explored by other researchers, but the main uncertainty was how the xylan coating would be affected by being a sliding surface in seawater when cathodically protected. Long term corrosion experiments were performed to study how the materials are affected by being immersed in seawater at open circuit potential (OCP) and when cathodically polarized to a protecting potential. The tribological performance of the materials was explored in dry conditions and in seawater at OCP and when cathodically polarized.

On the basis of the results presented in this thesis, the xylan coating appears to be sensitive towards cathodic disbonding. Hence, it is likely that the sliding movement will occur mainly between the uncoated SDSS power screw and NAB nut. Long term corrosion experiments show that similar current demand is required for SDSS and NAB when cathodically protected with a current density of 80 mA/m^2 and 75 mA/m^2 , respectively. Calcareous deposits were detected on the surfaces by using EDS. This will lower the total mass of sacrificial anodes needed for protection. The tribology results indicated that as long as SDSS is protected by xylan coating, the calcareous deposits are not accumulating extensively on the xylan surface affecting the sliding. While sliding NAB against SDSS calcareous deposits were formed on the SDSS surface increasing the sliding resistance. The COF was measured to be 0.42. The current density demand will be affected by flowing seawater during movement of the vessel, and will affect the number of anodes needed to protect the components. Al sacrificial anodes are mounted on the foil module for protecting the metal surfaces. When assuming that the power screw and nut connection will mainly consist of SDSS and NAB due to degraded coating, the number of sacrificial anodes were estimated to be 186 to achieve full protection throughout the lifetime of 25 years.

Sammendrag

Hydrofoiler har lenge blitt brukt på mindre båter. Men som følge av forskjellige utfordringer, har det ikke til nå vært mulig å bruke foiler på større farttøy. Wavefoil er et firma som har utviklet en uttrekkbar foliemodul som eliminerer utfordringene som har vært kytet til foiler. Drivstofforbruket vil da reduseres ved hjelp av bølgekraft. En xylanbelagt 25 Cr rustfri stål (SDSS) gjengestang med en nikkel-aluminium bronse (NAB) mutter vil gi den translatoriske bevegelsen av foliene.

Metaller som fungerer som glidende overflater i sjøvann vil være utsatt for korrosjon og slitasje. Hovedformålet for denne oppgaven var å gi et innblikk i hva som kan forventes i forhold til korrosjon og tribologisk slitasje under drift. Egenskapene til SDSS og NAB har tidligere blitt utforsket av andre forskere, men den største usikkerheten var oppførselen av katodisk polarisert xylanbelegg i sjøvann. Korrosjonseksperimenter ble utført over lengre tid for å studere hvordan materialene påvirkes ved å bli nedsenket i sjøvann fritt eksponert, og også når metallene er katodisk polarisert til et beskyttelsespotensial. Materialenes tribologiske ytelse ble utforsket i tørr tilstand og katodisk polarisert i sjøvann.

På grunnlag av resultater presentert i denne oppgaven vil xylan belegget bli degradert med tiden på grunn av katodisk avbinding. Dette vil da føre til at SDSS og NAB vil være i glidende kontakt under drift. Langsiktig korrosjonseksperiment viser at SDSS og NAB har omtrent likt strømbehov for å bli katodisk polarisert. Etter å ha vært polarisert over tid ble kalkholdig lag observert på overfalletene som har redusert strømbehovet til henholdsvis, 80 mA/m^2 og 75 mA/m^2 . Tilstedeværelse av dette laget vil redusere antall offeranoder som trengs for beskyttelse. De tribologiske testene indikerer at så lenge SDSS er beskyttet av xylanbelegg, akkumulerer ikke kalkholdige elementer på xylanoverflaten som påvirker glidningen. Men når xylan belegget degraderes og eksponerer SDSS, vil kalkholding lag øke friksjonen under glidning. Friksjonskoeffisienten var målt til å være 0.42. Økende hastighet av sjøvann under forflytning av farttøy vil påvirke strømbehovet til gjengestangen og mutteren, og vil da påvirke mengde anoder som trengs for å oppnå beskyttelse gjennom levetiden. Al offeranoder er montert på foliemodulen for å beskytte metalloverflatene. Når man antar at gjengestangen og mutteren hovedsakelig vil bestå av SDSS og NAB på grunn av degradert belegg, ble en mengde offeranoder anslått til 186 for å beskytte komponentene gjennom hele levetiden på 25 år.

Contents

Preface	I
Abstract	III
Sammendrag	V
Contents	VII
List of Figures	XI
List of Tables	XV
Nomenclature	XVII
1 Introduction	1
1.1 Background	1
1.2 Problem Description	2
1.3 Scope	4

1.3.1	Preliminary Project	4
1.3.2	Master Thesis	4
1.4	Literature Review	7
1.4.1	Corrosion Properties of 25 Cr Stainless Steel in Seawater	7
1.4.2	Corrosion Properties of Nickel-Aluminium Bronze in Seawater	9
1.4.3	Crevice Corrosion	12
1.4.4	Pitting Corrosion	14
1.4.5	Galvanic Corrosion	14
1.4.6	Cathodic Protection	17
1.4.7	Effect of Flowing Seawater on Corrosion	21
1.4.8	Tribological Contact Between Two Surfaces	22
1.4.9	25 Cr Stainless Steel Against Nickel-Aluminium Bronze	27
1.4.10	Xylan Coated 25 Cr Stainless Steel Against Nickel-Aluminium Bronze	28
1.4.11	Xylan Coating	29
1.4.12	Tribocorrosion	29
2	Experimental Work	31
2.1	Material and Sample Preparation	32
2.2	Corrosion Experiments	34
2.2.1	Instruments	34
2.2.2	Test Environment	34
2.2.3	Test Configuration	35
2.3	Tribology Experiments	37
2.3.1	Instruments	37
2.3.2	Test Environment	37
2.3.3	Test Configuration	38
2.4	Surface Characterization	40
2.5	Full-Scale Pilot Project at Fosen	43
3	Results	45
3.1	Long Term Corrosion Experiments	45
3.1.1	Freely Exposed at OCP	46
3.1.2	Cathodically Polarized SDSS, NAB and Xylan Coated SDSS	51
3.1.3	Galvanic Current Development	54
3.2	Tribological Experiments	54
3.2.1	Approximation of the Depth of Maximum Shear Stress	55
3.2.2	Dry wear tests	55
3.2.3	Reciprocal Experiments in Seawater	57

3.3	Full-Scale Pilot Project at Fosen	64
4	Discussion	67
4.1	Corrosion Experiments	67
4.1.1	OCP Development With Time for SDSS and NAB	67
4.1.2	Polarization Curves Obtained for SDSS and NAB	68
4.1.3	Behaviour of SDSS and NAB When Polarized to $-1050 \text{ mV}_{\text{Ag}/\text{AgCl}}$	69
4.1.4	Galvanic Coupling Between SDSS and NAB	70
4.1.5	Behaviour of Xylan Coated SDSS in Seawater	71
4.1.6	Other Concerns Regarding Use of SDSS and NAB in Seawater	72
4.2	Tribology Experiments	73
4.2.1	Tribological Properties of Xylan in Dry Condition	73
4.2.2	Tribological Properties of Xylan and SDSS in Seawater at OCP	75
4.2.3	Tribological Properties of Xylan and SDSS in Seawater at $-1050 \text{ mV}_{\text{Ag}/\text{AgCl}}$	76
4.2.4	Uncertainties During Experiments Performed	79
4.3	Full-Scale Pilot Module	79
5	Conclusion	81
5.1	Conclusion Regarding Corrosion Findings	81
5.2	Conclusion Regarding Tribological Findings	82
6	Further Work	85
	Bibliography	87
	Appendices	93
A	Calculations to Obtain Number of Sacrificial Anodes Required	95
B	Hertzian Contact Pressure Calculations	101
C	Photographs of the Experimental set-up	109

D Photographs of the Material Surfaces After Corrosion Experiments	111
E Datasheet for Xylan 1052	115
F Datasheet for SDSS	119
G Datasheet for Al-Anodes	121

List of Figures

- 1.1 Illustration of the foil module. The foils are shown in extended position [1]. 2
- 1.2 Illustration of the SDSS power screw with connected NAB nut. The power screw is coated with xylan 1052 coating. 3
- 1.3 Pourbaix diagram for Fe where the electrochemical state is displayed for different equilibrium potential and pH [2]. 8
- 1.4 Phase diagram for nickel-aluminium bronze, showing phases present with increasing wt% Al. The diagram is constructed for alloy containing 5% Ni and Fe [3]. 9
- 1.5 Pourbaix diagram for Cu where the electrochemical state is displayed for different equilibrium potential and pH [2]. 11
- 1.6 The initiation of crevice corrosion is illustrated [4] 13
- 1.7 Illustrating the effect on galvanic current when two metals are in metallic contact. The schematic current assumes no potential drop in the electrolyte or at the metal interface [5]. 15
- 1.8 Points of highest localized stresses in a thread are marked as A, B and C [6]. 19
- 1.9 Illustration of how increasing flow rate of seawater will affect the limiting current density with and without coating [5]. 21
- 1.10 Illustration of a typical Gaussian distribution of asperity heights obtained after grinding [7]. 23
- 1.11 The Stribeck curve displays how the lubrication regime depends on the viscosity of the lubricant, sliding speed and applied load [8]. 26
- 1.12 Photograph showing the uncoated SDSS power screw and the NAB nut. 27
- 1.13 Lubrication mechanism of MoS₂ displaying the easy shear property of the material [9]. 29
- 2.1 Illustration of the experimental set-up of the logging system during long term corrosion experiments conducted at SeaLab. 35

2.2	Illustration of the set-up when cathodically protected throughout the test period. This illustration also show the set-up used for obtaining cathodic and anodic polarization curves.	36
2.3	Illustration of the set-up for conducting reciprocal wear test.	38
2.4	Illustration of the set-up for conducting reciprocal wear test in seawater.	39
2.5	Surface profile of two different xylan coated SDSS samples measured by a profilometer.	41
2.6	A coating thickness of $\approx 90 \mu\text{m}$ is observed between the two red lines displayed in the image.	41
2.7	Example of EDS result.	42
3.1	Potential development of SDSS and NAB when immersed in seawater chamber for 157 days, and xylan coated SDSS immersed for 110 days.	46
3.2	Cathodic polarization curves are displayed for freely exposed SDSS and NAB obtained at day 42 (") and day 157 after immersion going from OCP to $-1100 \text{ mV}_{\text{Ag}/\text{AgCl}}$	48
3.3	Cathodic polarization curve for xylan coated SDSS after being freely exposed in seawater for 110 days. The potential was lowered from OCP to $-1100 \text{ mV}_{\text{Ag}/\text{AgCl}}$	49
3.4	Anodic polarization curve of NAB when increasing the potential from $100 \text{ mV}_{\text{Ag}/\text{AgCl}}$ below the measured OCP to $300 \text{ mV}_{\text{Ag}/\text{AgCl}}$ above the OCP. Suggested tafel according to the inclination are displayed providing information about the corrosion properties.	50
3.5	SEM image showing the NAB surface after the anodic polarization curve was obtained going from $100 \text{ mV}_{\text{Ag}/\text{AgCl}}$ below the measured OCP to $300 \text{ mV}_{\text{Ag}/\text{AgCl}}$ above the OCP.	51
3.6	Current density demand measured to sustain the potential at $-1050 \text{ mV}_{\text{Ag}/\text{AgCl}}$ for SDSS and NAB, and $-1080 \text{ mV}_{\text{Ag}/\text{AgCl}}$ for xylan coated SDSS.	52
3.7	Current density demand developed with time to sustain the potential of $-1080 \text{ mV}_{\text{Ag}/\text{AgCl}}$ for xylan coated SDSS sample holding a 2 cm^2 damage.	53
3.8	Galvanic current density and galvanic potential measured during 157 days of electrical contact between SDSS and NAB holding an SDSS/NAB area difference of ≈ 7	54
3.9	Development of the dry COF during reciprocal test between 316 SS and xylan coated SDSS for 1800 s.	56
3.10	Development of the measured dry COF during pin-on-disk experiments between 316 SS sphere and xylan coated SDSS for 1800 s. Rotational speed of 0.01 m/s and 0.1 m/s were used during testing.	57
3.11	Measured COF developed during reciprocal sliding of NAB cylinder against SDSS surface and xylan coated SDSS surface at OCP for 1800 s. A normal load of 10 N was applied.	58

3.12	OCP development measured during reciprocal sliding of NAB cylinder against SDSS surface and xylan coated SDSS surface for 1800 s at OCP. A normal load of 10 N was applied.	59
3.13	COF development during sliding of NAB cylinder against SDSS surface and xylan coated SDSS surface when cathodic polarized $-1050 \text{ mV}_{\text{Ag}/\text{AgCl}}$ for 1800 s. A normal load of 10 N was applied and a sliding speed of 0.01 m/s was used during the experiment.	60
3.14	Current development when sliding NAB cylinder against different surfaces in seawater. The samples were cathodic polarized to $-1050 \text{ mV}_{\text{Ag}/\text{AgCl}}$ during the sliding period.	61
3.15	SEM image of wear track of the spheres used for counter surface during dry reciprocal tribotests and pin-on-disk experiments.	62
3.16	SEM images of wear track obtained on NAB surface after sliding against SDSS and xylan coated SDSS when cathodic polarized to $-1050 \text{ mV}_{\text{Ag}/\text{AgCl}}$	63
3.17	Photograph of the full-scale xylan coated SDSS power screw after operation for 43 days at Fosen harbour. Arrows are given to show examples of areas of degraded coating.	64
3.18	Photograph of the NAB nut and the Al sacrificial anodes mounted on NAB surface after being exposed in seawater for 43 days.	65
4.1	SEM image showing the extent of localized corrosion attacks observed on NAB surface after obtaining the anodic polarization curve.	69
4.2	Comparison of dry COF measured when using reciprocal tribometer and continuous pin-on-disk tribometer for 2 N and 10 N at a speed of 0.01 m/s.	75
4.3	Wear track obtained on SDSS surface when cathodically protected after reciprocal sliding of a NAB cylinder for 1800 s at 0.01 m/s.	77
C1	Photographs of the tribometers used at Tribology lab at NTNU.	109
C2	TE-38 tribometer used for tribocorrosion experiments performed at OCP and when cathodically polarized.	110
C3	Photograph of the experimental set-up during long term experiments performed at SeaLab.	110
D1	Photographs showing NAB surfaces after corrosion experiments performed for 157 days at SeaLab.	112
D2	Photographs of the xylan coated SDSS surfaces after long term corrosion experiment.	113
D3	Photographs of the surfaces after long term corrosion experiment in electrical contact with SDSS with a SDSS/NAB area difference of ≈ 3	113

List of Tables

1.1	Overview of experiments conducted at the Tribology lab at NTNU.	5
1.2	Mechanical properties of 25 Cr stainless steel [10], nickel-aluminium bronze [3], PTFE [11, 12] and 316 stainless steel [13].	28
2.1	Chemical composition of the SDSS alloy used for corrosion and tribocorrosion experiments [14].	32
2.2	Chemical composition of nickel-aluminium bronze alloy [14].	33
2.3	Normal loads used for dry wear tests and the corresponding maximum Hertz contact pressure.	39
2.4	Maximum Hertz contact pressure calculated for line contact against SDSS and xylan surface when applying 10 N.	40
2.5	Anode specifications are obtained from the supplier, Skarpenord.	43
3.1	OCP value measured for SDSS and NAB when first immersed in seawater and after being exposed for 157 days.	47
3.2	OCP value measured for xylan coated SDSS when first immersed in seawater and after being exposed for 110 days.	47
3.3	Corrosion properties approximated by using suggested Tafel lines from anodic polarization curve obtained for freely exposed NAB for 157 days.	50
3.4	Composition of the layer formed on the surface of the polarized samples.	53
3.5	Depth of the maximum shear stress, z , for the different loading scenarios.	55
3.6	Average COF during test period, volume loss and wear rate for reciprocal test. All tests were conducted with a speed of 0.01 m/s.	56
3.7	Average COF during test period, volume loss and wear rate for pin-on-disk tests conducted with 0.1 m/s and 0.01 m/s.	57
3.8	Comparison of COF measured during sliding of NAB cylinder against SDSS surface and xylan surface when applying 10 N at 0.01 m/s for 1800 s. COF obtained at OCP and when cathodically polarized are given. Average values are calculated.	60

3.9	EDS analysis of spheres used for dry tribotests at 0.01 m/s.	62
3.10	EDS analysis of NAB cylinder after performing tribocorrosion experiments in seawater at OCP and when cathodic polarized to $-1050 \text{ mV}_{\text{Ag/AgCl}}$	63
A1	Current densities used during design.	96
A2	Area to be protected in m^2	96
A3	Parameters obtained from the supplier, Skarpenord.	96
A4	Other parameters obtained from DNV-RP-B401 and ISO 15589-2	96
B1	Material properties for materials creating the contacts of interest.	101

Nomenclature

Ag/AgCl	Silver/Silver Chloride electrode
BCC	Body Centered Crystal
COF	Coefficient of Friction
CSCC	Chloride Stress Corrosion Cracking
DFT	Dry Film Thickness
EDS	Energy-dispersive X-ray Spectroscopy
FCC	Face Centered Crystal
FEPA	Federation of European Producers of Abrasives
HISC	Hydrogen Induced Stress Cracking
IFM	Infinite Focus Microscopy
MIC	Microbially Induced Corrosion
NAB	Nickel-aluminium bronze
OCP	Open circuit potential
PFTE	Polytetrafluoroethylene
pH	Expressing the acidity and alkalinity of a solution
PREN	Pitting Resistance Equivalent Number
SDSS	Super Duplex Stainless Steel
SEM	Scanning Electron Microscopy
SRB	Sulfate Reducing Bacteria
SS	Stainless steel

Chapter 1

Introduction

1.1 Background

The concept of foils as a method of increasing performance of sea-faring vessels is well known. However, due to challenges resulting from having a permanent fixed foil attached to the hull, the concept has not seen much use. Solutions to these challenges have been highly sought after, as the potential fuel savings marine vessels will experience are significant. A retractable foil system is currently under development by Wavefoil AS. By using a power screw and nut to extend and retract the foils, Wavefoil intends to solve many of these challenges.

The foil module developed by Wavefoil is designed to be used on larger marine vessels and unlike previous foils, they are designed to use wave force to increase the horizontal movement instead of lifting the hull out of the water. In addition, extra stability in the vertical direction is achieved. The reduced fuel consumption depends on the traveling route, e.g. due to ocean currents [15, 1]. The foils are designed to be extended and retracted by using a power screw with a connecting nut to provide a translatory movement. Illustration of the foil module is given in Figure 1.1, where the foils are shown in extended position.

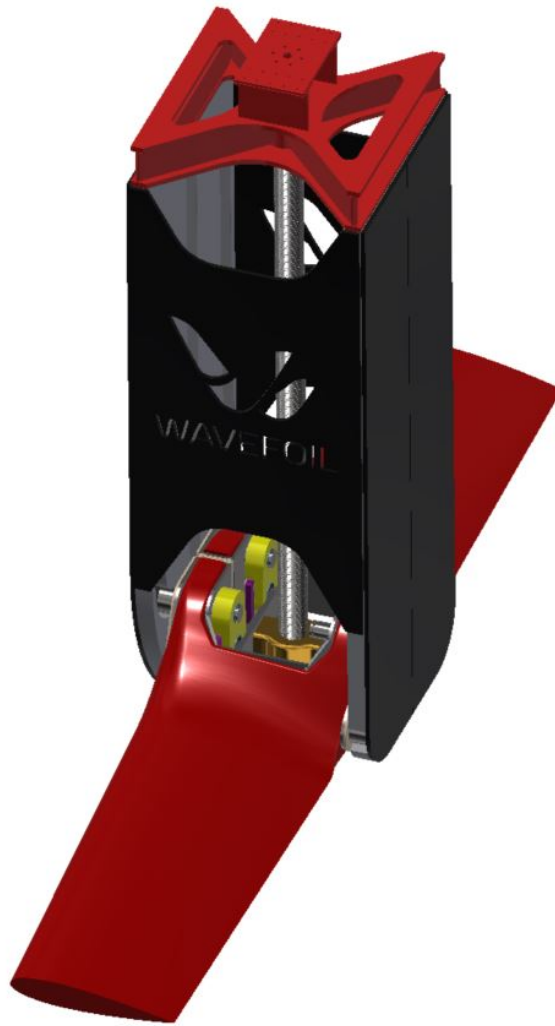


Figure 1.1: Illustration of the foil module. The foils are shown in extended position [1].

1.2 Problem Description

The foil module will be continuously exposed to seawater holding a temperature of 10-15 °C throughout the lifetime of 25 years. The foils will be extended and retracted on an average once per day. A 25 Cr stainless steel (SDSS) power screw and a connecting nickel-aluminium bronze (NAB) nut are installed to provide the translatory movement. Metals exposed to seawater are prone to different corrosion attacks. Mechanisms that are assumed to be relevant for these materials used in this system will be elaborated in more detail during this thesis. Figure 1.2 gives an illustration of the SDSS power screw and the connecting NAB nut.



Figure 1.2: Illustration of the SDSS power screw with connected NAB nut. The power screw is coated with xylan 1052 coating.

For environmental considerations, solid lubrication was preferred instead of liquid lubrication such as oil and grease. Xylan 1052 was chosen on the basis of its low coefficient of friction, and was applied on the SDSS power screw. This will also provide electrical isolation between the SDSS power screw and NAB nut, preventing galvanic corrosion. During daily movement of the foils, sliding contact will arise between the power screw and nut and may lead to wear and degradation of the coating and the metal surfaces. It is beneficial to coat the larger cathode to reduce the current density demand when using cathodic protection. The components are protected from corrosion attacks by using sacrificial anodes. It is therefore of special interest to study how the components will be affected by being cathodically polarized.

1.3 Scope

This work were divided in two parts; preliminary project performed during autumn 2018 and master thesis during spring 2019.

1.3.1 Preliminary Project

During the preliminary work to this master thesis a literature study was performed. The challenges that are assumed to arise in regards to corrosion and tribology during the lifetime of 25 years continuously exposed to seawater were studied. On the basis of literature gathered during this work, it was recommended that cathodic protection was applied on the foil module to obtain protection against corrosion attacks. Coral A-5 Al sacrificial anodes were then mounted on the foil module to obtain corrosion protecting when being exposed to seawater.

The behaviour of SDSS, NAB and xylan coated SDSS when being exposed to seawater for a longer period of time is of special interest when considering corrosion attacks. Therefore long term experiments were commenced at SeaLab NTNU in order to study the potential development and the current demand developed with time.

Corrosion tests commenced at SeaLab were as follows:

- Corrosion of SDSS in seawater
- Corrosion of NAB in seawater
- Galvanic coupling of SDSS and NAB
- Polarized SDSS to $-1050 \text{ mV}_{\text{Ag}/\text{AgCl}}$
- Polarized NAB to $-1050 \text{ mV}_{\text{Ag}/\text{AgCl}}$
- Freely exposed xylan coated SDSS
- Xylan coated SDSS coupled to zinc anode
- Xylan coated SDSS with artificial damage coupled to zinc anode

1.3.2 Master Thesis

The main objective for this master thesis is to obtain an understanding of the degree of degradation that can be expected of the power screw and nut. How the materials are affected in terms of

corrosion attacks and wear are studied. It is of special interest how they will be affected by being cathodically polarized over time.

Main objectives to be studied in this thesis are as follows:

- To analyze the extent of corrosion attacks on SDSS and NAB after being immersed in seawater for longer period of time and when in electrical contact with each other.
- To analyze how xylan coated SDSS is affected by being immersed in seawater at OCP and when cathodically protected.
- To examine the tribological performance of the materials at OCP and when cathodically polarized.
- To obtain an understanding of what can be expected in terms of electrochemical and mechanical wear of the power screw and nut during operation.

In addition to long term corrosion experiments conducted at SeaLab listed above in Section 1.3.1, tribological experiments were performed during Spring 2019 at the Tribology lab at NTNU. The tribological performance of the materials was studied in dry condition and when immersed in seawater. It was of special interest to examine how the materials behaved when cathodically polarized. An overview of the tribological experiments conducted is given in Table 1.1.

Table 1.1: Overview of experiments conducted at the Tribology lab at NTNU.

Freely exposed in SW	NAB sliding against Xylan coated SDSS NAB sliding against SDSS
Cathodically protected	NAB sliding against Xylan coated SDSS NAB sliding against SDSS NAB sliding against damaged xylan coated SDSS

1.4 Literature Review

This section contains information about the corrosion mechanisms that is assumed to may affect the SDSS power screw and NAB nut in the foil module. In addition some information is given about mechanical degradation that can be expected as the power screw and nut will act as sliding surfaces. SDSS and NAB are subjected to different corrosion mechanisms and will in electrical contact with each other experience galvanic corrosion. The SDSS and NAB components are designed to be protected by using sacrificial anodes. Literature regarding challenges that may occur when using cathodic protection will also be given. The sliding system studied is designed with a lifetime of 25 years immersed in seawater at approximately 10-15 °C with daily extension and retraction of the foils.

1.4.1 Corrosion Properties of 25 Cr Stainless Steel in Seawater

25 Cr stainless steel (SDSS) consists of a microstructure with approximately 50/50 of austenite and ferrite. Chromium (Cr) content in steels must exceed 12 wt % in order to be defined as stainless steel. Cr will in contact with atmosphere react with oxygen (O₂), forming a protective chromium oxide (Cr₂O₃) layer. The superior corrosion resistance of SDSS is due to high Cr content, exceeding 25 wt% [16, 5]. The oxide layer does not precipitate on the surface, but according to Bardal (1994) it forms as an extension of the metal structure [5]. As the structure of the oxide layer is similar to the metal, it holds low resistance against electron movement in the oxide layer and therefore does not hamper reduction reaction occurring on the oxide layer. Hence the oxide layer protects the metal against corrosion attacks by resisting movement of metal ions [5].

Passive metals are prone to localized corrosion attacks. Weak areas in the oxide layer (i.e. grain boundaries and inclusions) may in presence of chlorides be degraded creating a small anodic area while the intact passive layer will act as cathode [5]. This will be explained in more detail in Section 1.9 and Section 1.4.4. How resistant a metal is against localized corrosion attacks when exposed to seawater is measured by an empirical pitting resistance equivalent number (PREN) which takes into account the content of chromium (Cr), molybdenum (Mo) and nitrogen (N) [16]. The equation is shown by Equation 1.1

$$PREN = wt\%Cr + 3.3 * wtMo\% + 30 * wt\%N \quad (1.1)$$

Higher PREN number is equivalent to higher corrosion resistance. When considering corrosion properties, the electrochemical potential if the material is essential. Compere and Le Bozec (1997) presents graphs showing potential development of stainless steel UNS S32654 exposed to

natural seawater at different geographical sites. Graphs presented shows a trend where potential increases rapidly within the first few days immersed in seawater, before reaching a steady state value. Tests performed in Trondheim in 1993 during winter season have shown a stabilized potential of approximately +300 mV_{SCE}, which is equivalent to +345 mV_{Ag/AgCl}. The increase of potential was ascribed by the authors to be due to biofilm formed by bacteria in seawater adhering to the metal surface [17]. Metals holding a passive layer experience an ennoblement of corrosion potential after biofilm formation. The increased potential is being assumed to be due to increased oxygen reduction reaction on the biofilm [17]. Bergel, Fèron and Mollica (2005) have in their research studied the catalytic effect of biofilm on oxygen reduction reaction on stainless steel. Their findings supports the theory about the biofilms ability to enhance oxygen reduction in seawater [18].

Pourbaix diagram of iron (Fe) is given in Figure 1.3 showing how the equilibrium potential of the metal is affected by changing the potential and pH. The potential is displayed versus standard hydrogen electrode, where 0 V_{SHE} is equivalent to -0.2 V_{SHE}. The upper striped line show the O₂ reduction while the lower striped line show at which potentials the H₂ is included in the reduction reaction. The pH of seawater is usually in the range of 8-8.3 [5].

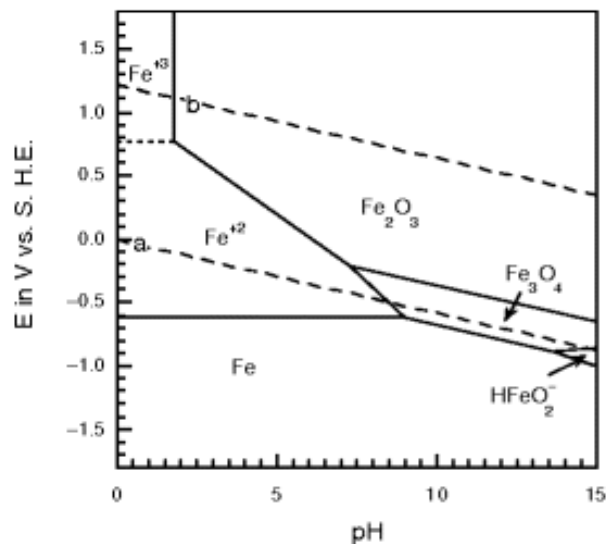


Figure 1.3: Pourbaix diagram for Fe where the electrochemical state is displayed for different equilibrium potential and pH [2].

In the presence of corrosive environment and when subjected to high stresses, chloride stress corrosion cracking (CSCC) must be considered as a possible mechanisms [19, 20]. CSCC is possible when metals are subjected to a combination of a high amount of chloride and elevated temperatures when subjected to stress. Design temperature limits for stainless steel is given by NORSOK M-001. Limiting temperature for SDSS in saliferous marine environments is defined as $< 110^{\circ}\text{C}$, and immersed in seawater the maximum temperature is 20°C , when in the presence of a crevice (e.g. threads) [21].

1.4.2 Corrosion Properties of Nickel-Aluminium Bronze in Seawater

Nickel-aluminium bronze (NAB) is a copper-based alloy (Cu), containing up to 14 wt% aluminium (Al) as the main alloying element. A smaller fraction of nickel (Ni), manganese (Mn) and iron (Fe) are added and contribute with different properties to the material. The intermetallic phases present in NAB influences the corrosion properties of the metal. The alloy used in this thesis has a Al content of 9.44 %.

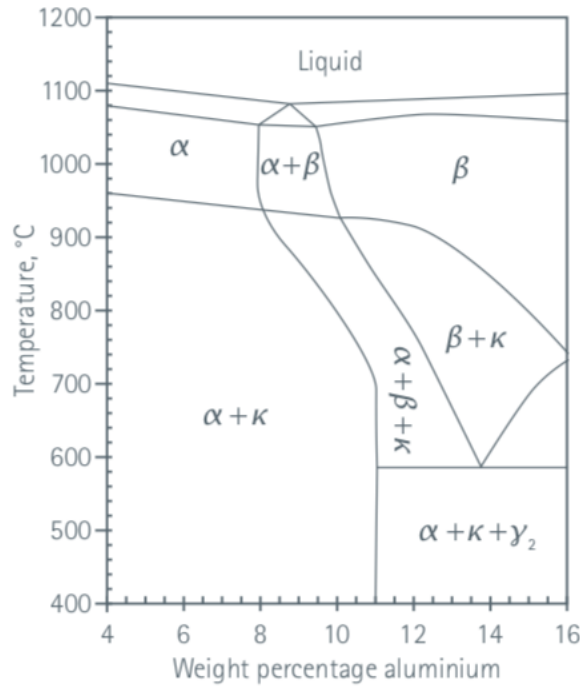


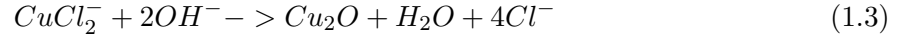
Figure 1.4: Phase diagram for nickel-aluminium bronze, showing phases present with increasing wt% Al. The diagram is constructed for alloy containing 5% Ni and Fe [3].

NAB is sensitive to selective corrosion due to intermetallic phases containing different phase compositions. α -phase consisting of a Cu-matrix with Al particles in solid solution, will corrode in the presence of seawater, while κ -phases having Fe-rich and Ni-rich phases, act as reduction sites [14]. When chloride ions are present, α -phase will corrode according to:



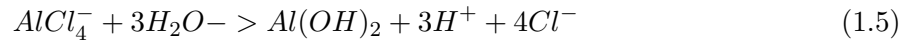
When exposed to seawater, NAB forms an oxide layer with a Cu-based layer and Al-based layer, where the two layers protect by different mechanism [22]. Schüssler and Exner (1993) have presented results showing that the protective layer is enriched in Cu-rich phases in the outer part of the oxide layer, while the inner part is enriched with Al-rich phases [23]

Cupric chloride (CuCl_2^-) will during oxidation process accumulate on the metal surface and form a porous solid layer. This layer will after reacting with hydroxides (OH^-) form a dense protective cuprous oxide (Cu_2O) according to Equation 1.3 [14]:



Schüssler and Exner (1993) have proposed mechanisms for the protective performance of the Cu-rich oxide layer which was assumed to be due to the ability of Cu_2O to reduce the cathodic reduction reaction of O_2 [23].

The protective mechanism of the Al-rich oxide layer has been suggested by the same authors to be due to its barrier property resisting ion transportation through the oxide layer [23]. Formation of Al oxide occurs according to reactions given by Equation 1.4 and Equation 1.5.



Al hydroxide ($\text{Al}(\text{OH})_3$) will further react and precipitate Al oxide (Al_2O_3), and together with Cu_2O will form the protective layer on NAB [14]. Hence, NAB is protected against corrosion by hamper both cathodic and anodic reactions occurring. The protective layer formed on NAB has shown to reduce the corrosion rate by a factor between 20-30 [23]. NAB has been preferred in applications where high flow velocity is expected, due to the alloys high critical flow velocity. NAB is experienced to have a critical velocity of 20-25 m/s when subjected to a flow of pure water (i.e. particle concentration is negligible) [24].

When being exposed to seawater for a longer period of time, bacteria and organisms will accumulate on the surface altering the potential of the metal. Experiments studying the change in the potential of freely exposed NAB in natural seawater have been performed by Krogstad and Johnsen (2017). They present results showing how the electrochemical kinetics develops with time exposed in seawater. Their study shows that potential of NAB increases with time (i.e. ennoblement) going from $-230 \text{ mV}_{\text{Ag}/\text{AgCl}}$ up to $-200 \text{ mV}_{\text{Ag}/\text{AgCl}}$ reaching a potential of $-150 \text{ mV}_{\text{Ag}/\text{AgCl}}$ after 20 days of exposure. The authors proposed that the first increase of potential was due to biofilm formation enhancing the cathodic reaction occurring on the surface [25].

The pourbaix diagram of the main element of NAB, Cu, is presented in Figure 1.5, where areas when the metal is active, passive and immune are displayed for the different pH and potential. The potential is displayed versus standard hydrogen electrode, where 0 V_{SHE} is equivalent to

$-0.2 V_{SHE}$.

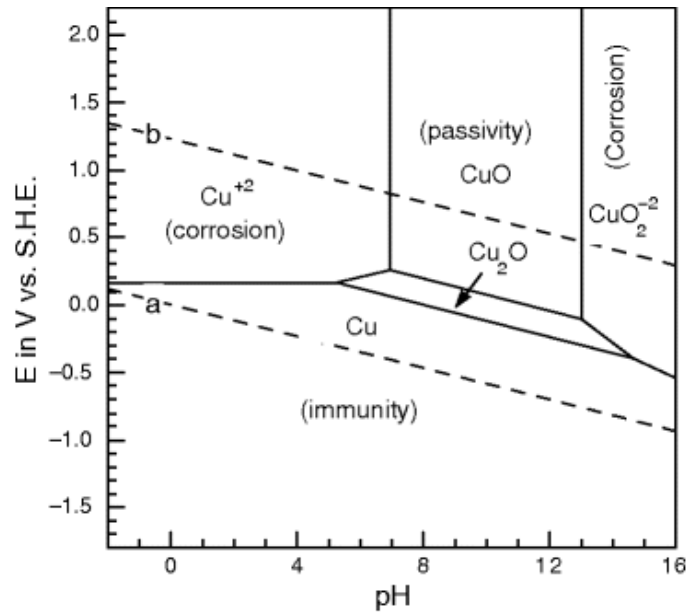


Figure 1.5: Pourbaix diagram for Cu where the electrochemical state is displayed for different equilibrium potential and pH [2].

Uniform Corrosion

Oakley et al. (2007) have performed long term corrosion tests of NAB in seawater showing that NAB is sensitive to uniform corrosion when exposed to running fresh seawater [26]. The general corrosion rate of NAB in un-polluted seawater is estimated to be in the range of 0.002-0.02 mm/year [24], given that the velocity does not exceed the limiting velocity of 20-25 m/s [22].

Corrosion rate in mm/year can be calculated when the current density is measured by using Faradys law given in Equation 1.6.

$$\frac{\Delta s}{\Delta t} = 3268 * \frac{i_{corr} M}{z \rho} \left[\frac{mm}{year} \right] \quad (1.6)$$

M is the atomic mass, z is the amount of electrons in the equilibrium reaction and ρ is the density [5]. This gives the corrosion rate in millimeter per year uniformly distributed over the whole surface.

Corrosion in Polluted Seawater

Cu-ions in the oxide layer can in the presence of sulfides form Cu monosulfide (CuS). This is a porous layer, and will reduce the protective ability of the layer [14]. CuS will also in the case of aerated water accelerate the corrosion process due to its catalytic ability on the oxygen reduction [27].

Research performed on NAB is scarce, though a 90 Cu-10 Ni and 70 Cu-30 Ni alloy has been tested in aerated polluted seawater to study how sulfides affect the protective oxide layer on copper-alloys [28]. The corrosion rate is shown to increase markedly when exposed to stirred sulfide-polluted seawater compared to sulfide-polluted stagnant seawater. A corrosion rate of 5.58 mm/year and 0.58 mm/year was measured for stirred and stagnant condition, respectively [28]. Syrett (1981) has previously studied the effects of sulfide-polluted seawater on the degradation of copper-alloys. He presented results showing that corrosion attacks did not occur while being exposed to polluted seawater, but when exposed to fresh seawater subsequent to being exposed to polluted seawater. This was a result of the protective ability of the oxide layer being reduced [29]. In aerated polluted seawater reaction between O_2 and sulfides will arise converging O_2 concentration towards zero. Hence the reduction process in polluted seawater will diminish. When pre-exposed to polluted seawater before exposed to un-polluted seawater the metal experience severe corrosion attacks for some time as a result of a degraded oxide layer. As the anodic dissolution continues, the passive layer will be restored when Cu-ions released forms Cu_2O [29].

1.4.3 Crevice Corrosion

In presence of a crevice (e.g. threads), holding an opening such that seawater is allowed to enter the crevice, but is too shallow for seawater to be recycled, stagnant seawater may result in corrosion attacks. This mechanism is illustrated in Figure 1.6.

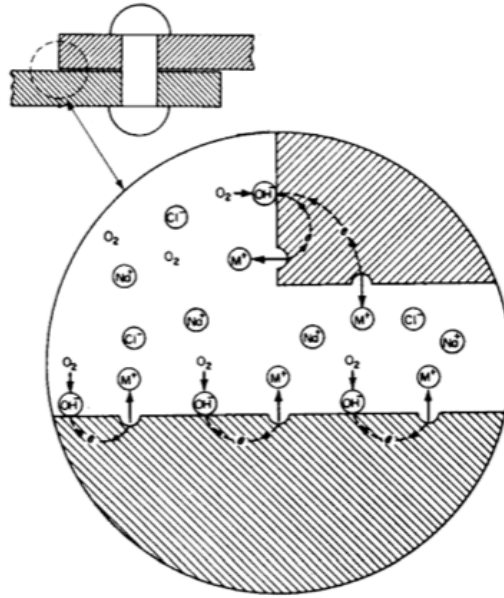


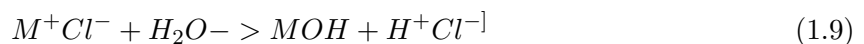
Figure 1.6: The initiation of crevice corrosion is illustrated [4]

Inside the crevice, anodic and cathodic reactions will at first occur simultaneously on the surface. When the O_2 concentration convergence zero, the reduction process will occur outside the crevice to accommodate the anodic reaction inside. This leads to an unfavorable cathodic to anodic area relationship.



As a result of ceased cathodic reaction inside the crevice, OH^{-} will no longer be produced. Hence chloride will migrate due to electroneutrality creating an aggressive environment. Metals holding a passive layer is specially sensitive to this form of corrosion. Aggressive ions such as chlorides may cause the oxide layer to break at certain areas exposing the metal. These areas will act anodic while the intact oxide layer acts as cathode. This creates an unfavorable anode/cathode area, thus localized corrosion attacks will occur.

M^{2+} and OH^{-} will in the presence of seawater, react and form metal hydroxide and hydrochloric acid (HCl) according to Equation 1.9:

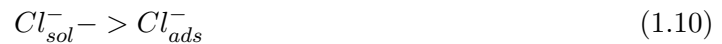


Formation of hydrochloric acid will lower the pH inside the crevice and accelerate the corrosion process [5]. As a result of the increased corrosion rate, the migration of chloride ions into the crevice will continue, and crevice corrosion is as such an autocatalytic process.

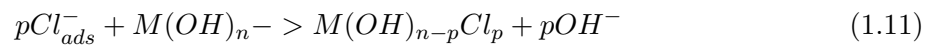
1.4.4 Pitting Corrosion

Pitting corrosion can be divided into two stages; Pitting initiation and pitting growth. Different mechanisms behind the initiation have been presented. According to Bardal (1994), pitting may be initiated by diffusion of halogen ions such as chloride ions through the oxide layer. Irregularities in the oxide layer such as metal grains or inclusions can be such points where diffusion occurs, causing localized corrosion attacks [5]. When the pit is initiated, the pitting growth commences through mechanism equivalent as explained for crevice corrosion above.

According to theory described by Bardal (1994) the initiation occurs according to Equation 1.10 and Equation 1.11 [5]:



Equation 1.10 shows the formation between being chloride ions in the seawater to be ions adsorbed on the metal surface. When chloride ions are adsorbed to the surface they are able to react with the oxide layer according to Equation 1.11 [5].



For pitting to initiate, the potential of the material must exceed a critical pitting potential, depending on temperature, chloride concentration and pH in the seawater. Figure 1.3 and Figure 1.5 gives Pourbaix diagram for Fe and Cu, respectively. How the pH affect the state of the metals is shown for different potentials.

1.4.5 Galvanic Corrosion

Electrical contact between two different metals in presence of an electrolyte holds a relative electrochemical potential. This potential may be arranged in a galvanic series, where the metal with the most positive potential has the highest reduction potential, hence is the noblest. Electrical contact between a noble metal with a less noble metal will create a galvanic current.

Electrons will then move from the less noble metal to be reduced on the surface of the noble metal. Simultaneously as the electrons are moved, metal ions are released due to electroneutrality resulting in a corrosion reaction. For galvanic corrosion to occur some conditions must be met; electric contact between the materials with a certain potential difference and both materials must be in contact with the same electrolyte [5]. In Figure 1.7 the change in current when electrical contact between two different metals is displayed.

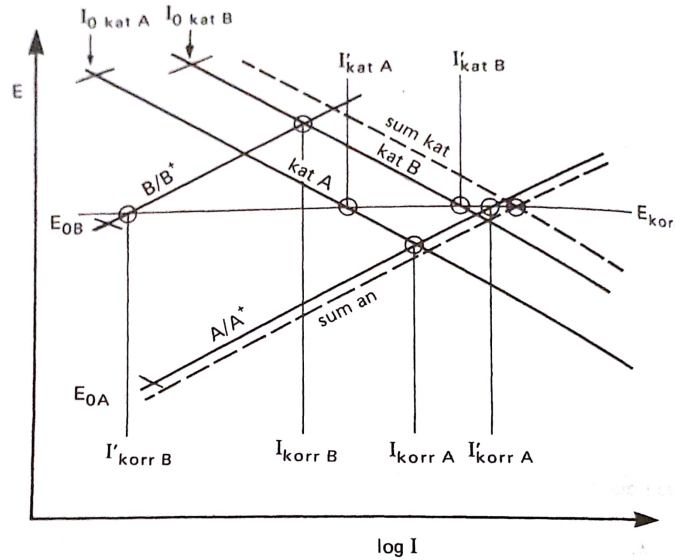


Figure 1.7: Illustrating the effect on galvanic current when two metals are in metallic contact. The schematic current assumes no potential drop in the electrolyte or at the metal interface [5].

Where I'_{korrrA} and I'_{katB} shows the total anodic and cathodic current, respectively. The figure illustrates that the anodic current for the less noble material, I'_{korrrA} , increases as a result of the combination of self-corrosion and galvanic corrosion. Simultaneously, the corrosion rate of the more noble material, I'_{katB} , is reduced.

When considering galvanic corrosion, a large area difference between the anode and cathode is unfavorable as this will lead to high anodic current to accommodate the higher cathodic current. The corrosion reaction equilibrium is shown by Equation 1.12:

$$\sum I_{anode} = \sum I_{cathode} \tag{1.12}$$

By considering anodic and cathodic current on both materials, Equation 1.13 is obtained.

$$I_{galv} = I'_{korrrA} - I'_{katA} = I'_{korrrB} - I'_{katB} \tag{1.13}$$

The anodic current on B will be small due to protection from A, hence it can be neglected. In addition, the anodic current will be significantly higher on A compared to cathodic current on B, hence this may be neglected. By using these assumptions, Equation 1.14 is obtained.

$$I'_{korrA} = I'_{katB} \quad (1.14)$$

Where I' takes into account the current density and the area. By using Equation 1.12, the severity of the area difference is given by Equation 1.15:

$$i_{anode} = i_{cathode} * \frac{A_{anode}}{A_{cathode}} \quad (1.15)$$

Equation 1.15 reveals that the anodic current density increases with the reduced anodic area and increased cathodic area [5].

A potential difference of minimum 50 mV between two metals in regards to the galvanic series is accepted as the limit before galvanic corrosion must be considered [5]. SDSS has a corrosion potential of approximately +345 mV_{Ag/AgCl} in presence of biofilm [17], while NAB has shown to have a corrosion potential of -150 mV_{Ag/AgCl} when exposed to seawater for a certain amount of time to ensure biofilm formation [25]. This creates sufficient driving force between the metals, and NAB is therefore expected to be sacrificed on behalf of SDSS.

Galvanic corrosion test between stainless steel (SS) and NAB with a 1:1 area ratio in seawater has been performed by Krogstad and Johnsen (2017). They present the development of potential with time after coupling, where an increase in corrosion potential is seen as a function of time. This was attributed to biofilm formation on SS where the cathodic reaction increases, and as a result, NAB degrades faster to accommodate the cathodic reaction on SS [25]. When the biofilm is formed, the increased cathodic efficiency of SDSS moves the polarization curve to higher galvanic current density [30]. Their results revealed that when reaching a galvanic potential of approximately -150 mV_{Ag/AgCl}, the galvanic potential is increased significantly, while the galvanic current density remains unchanged. It is proposed by the authors that this is due to the formation of an oxide layer on NAB which protects by preventing an anodic and cathodic reaction, resulting in the galvanic potential to change in noble direction [14]. The increasing potential has further been suggested to allow pitting corrosion where a sharp increase in current density was observed at the potential of -50 mV_{Ag/AgCl}. This attributes to the consequence of the degraded oxide layer on NAB [25]. Similar results have previously been presented by Francis (1999), research performed on galvanic corrosion of NAB and SDSS, where galvanic tests were performed in natural seawater with area ratios of 1:1 and 1:10 of NAB/SDSS, respectively. Results obtained revealed that NAB was prone to localized corrosion attacks on the open surface when in an electric contact to a more noble material. The extent of localized attacks was enhanced with

increased NAB/SDSS area ratio [30].

1.4.6 Cathodic Protection

Cathodic protection by using sacrificial anodes is often used in order to protect metals exposed to seawater when a long lifetime of the materials is desired. The amount of anodes needed can be estimated by using DNVGL-RP-B401 standard [31]. When having coated surfaces, a coating breakdown factor (CBF) must be included in the calculations. Challenges such as hydrogen induced stress cracking (HISC) and cathodic disbonding may affect materials being cathodically polarized over time [5, 32]. When cathodically protected, the advantageous calcareous deposits will be formed reducing the current density needed from the anodes. Sacrificial anodes will protect the metal by using less noble metal to be degraded on behalf of the protected metal. Al-anodes are according to DNVGL-RP-B401 often preferred due to higher electrochemical capacity [Ah/kg] compared to Zn-anodes [31]. Al-anodes have an open circuit potential (OCP) of $-1090 \text{ mV}_{\text{Ag}/\text{AgCl}}$ in seawater, see datasheet for Al-anodes in Appendix G.

Sacrificial anodes will be degraded according to Equation 1.16. The accompanying reduction reaction on SDSS and NAB will be according to Equation 1.17 in alkaline aerated seawater and according to Equation 1.18 in acidic seawater and at low potentials.



According to ISO 15589-2, duplex stainless steels are protected at potentials lower than $-500 \text{ mV}_{\text{Ag}/\text{AgCl}}$. At this potential the hydrogen evolution is included in the cathodic reaction at pH 8, see Pourabix diagram in Figure 1.3. According to Bardal (1994), the cathodic reaction will be limited as it is activation controlled when first polarized in cathodic direction from OCP. When continuing to lower the potential, a certain potential will be reached where the reaction process will occur faster than the O_2 diffusion towards the surface occurs. Hence, the reaction is being concentration controlled. When the reaction is activation controlled, the relation between the current density and overpotential is given by the Tafel equation. This equation may be approximated by extrapolating the overpotential curve obtained during polarization. At lower

potentials, hydrogen evolution may dominate the cathodic reaction even at alkali pH levels, and will increase the overall cathodic reaction [5].

Hydrogen Induced Stress Cracking

When couple a metal to a sacrificial anode, its potential will be lowered in cathodic reaction. As previously explained, hydrogen evolution occurs at lower potentials according to Pourbaix diagram. Reduction reaction when cathodically protected will be according to Equation 1.19.



In presence of hydrogen ions, hydrogen gas H_2 will evolve on the cathode. Some hydrogen atoms will be formed as H_2 , while Some atoms will be adsorbed on to the metal surface and diffuse into the metal structure [5]. SDSS is a duplex stainless steel which consists of both BCC and FCC microstructure when in room temperature. The FCC structure has low solubility of hydrogen atoms, and when the saturation limit is reached the mechanical properties of the metal will be altered. The metal will experience reduced toughness [33]. SDSS is according to DNVGL-RP-F112 exposed to HISC at potentials lower than $-800 \text{ mV}_{\text{Ag}/\text{AgCl}}$ [34], which can be related to the amount of hydrogen available on the surface at low potentials.

Some given conditions must be present for HISC to be initiated [35]:

1. Hydrogen present
2. Microstructure that is susceptible to HISC
3. A certain level of stress, either external or residual stress

When applying a certain amount of stress on metal, the surface may be deformed such that new sites are formed. This creates more sites where the cathodic reaction can occur and increases the risk of HISC [33]. The power screw is designed to have ACME threads with a certain angle. Figure 1.8 illustrates points where the highest localized stress is likely to occur.

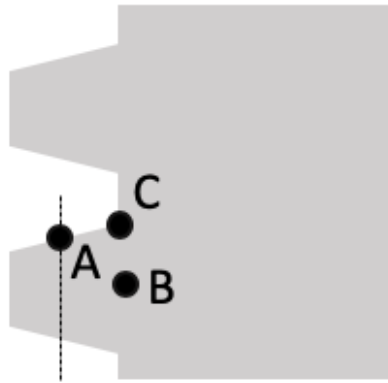


Figure 1.8: Points of highest localized stresses in a thread are marked as A, B and C [6].

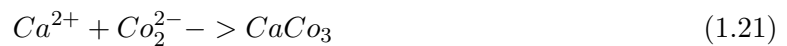
Calcareous Deposits

Reduction reaction will in aerated seawater occur according to Equation 1.20:



OH^- produced on the metal surface will increase the pH adjacent to the surface, leading to the precipitation of calcium carbonate ($CaCO_3$) and magnesium hydroxide ($Mg(OH)_2$). $CaCO_3$ and $Mg(OH)_2$ will participate at different pH levels, and pH level at which they are formed can be calculated by using the solubility constant. This has been performed by Yang, Scantlebury and Koroleva (2015) [36].

Their calculations showed that the concentration of hydroxide ions will be sufficient and form calcium carbonate ions at pH above 7.5, and the precipitation will occur according to Equation 1.21 [36].



While magnesium hydroxide will be formed at pH above 10. The reaction is shown in Equation 1.22 [36].



As these compounds precipitate on the surface, they will act as a protective layer, lowering the oxygen reaching the metal surface. The current demand needed for protection will decrease accordingly [37]. In systems being protected by sacrificial anodes, the total mass of anode required will be decreased according to the decreased current demand. This is beneficial in terms of weight and cost, and is desired in many systems [31].

Nickel-Aluminium Bronze With Cathodic Protection

Cu-alloys are known for its macrofouling resistance when immersed in seawater due to the continuous release of toxic Cu-ions. When cathodically protected surfaces are prevented from releasing Cu-ions, its anti-fouling resistance will, as a result, be prevented [14]. When biofouling accumulates on a metal surface, seawater may be trapped between the sediments and metal surface resulting in stagnant conditions. In seawater sulfate-reducing bacteria (SRB) can be naturally present, and will in stagnant condition cause microbial induced corrosion (MIC). SRB is a bacteria that prefer environments that are free of O_2 , e.g. under fouling or in crevices where stagnant conditions will occur [5]. Sulfate occurs naturally in seawater and will in presence of SRB be included in its metabolism process and be reduced to sulfide [38]. The protecting ability of NAB will then be altered as sulfides continue to react with Cu-ions in the oxide layer and form porous CuS layer [14]. Long term experiments performed by Oakley et al. (2007) revealed severe localized corrosion attacks up to 580 μm when removed fouling on the surface [26]. Research provided by Krogstad and Johnsen (2017) shows that the formation of bacterial cells that forms biofilm was more pronounced when cathodic polarized to $-430 \text{ mV}_{\text{Ag}/\text{AgCl}}$. This was ascribed as a result of the reduced amount of Cu-ions released when cathodically protected which enhances the biofilm formation [25].

Coating With Cathodic Protection

Cathodic protection in combination with coating may cause cathodic disbonding of the coating reducing the adherence between coating and metal surface. Different mechanisms have been proposed to be the cause of cathodic disbonding; oxide reduction, alkaline hydrolysis and interfacial failure [39]. Watts (1989) writes that the different mechanisms have in common that the production of alkalis increases the pH under the coating, which in turn causes loss of adhesion in the substrate/coating interface [39].

Knudsen and Skar (2008) have studied parameters affecting the performance of coatings, where they presented results showing that O_2 concentration and potential affects the degree of cathodic disbonding. Decreasing O_2 concentration resulted in decreased disbondment. While decreasing

the electrode potential resulted in increased disbondment down to $-1400 \text{ mV}_{\text{SCE}}$ corresponding to $-1350 \text{ mV}_{\text{Ag/AgCl}}$. This is a direct result of increased cathodic reaction. The degree of disbonding has shown to be time-dependent, and authors have previously reported a linear relationship between degree disbonding and time [32].

1.4.7 Effect of Flowing Seawater on Corrosion

The cathodic reaction may either be controlled by activation of the reduction reaction or the concentration of O_2 available at the surface vicinity limiting the reaction. As O_2 reduction continues the concentration converges zero, and thus will limit the corrosion process. Flowing seawater will increase the O_2 diffusion towards the surface increasing the O_2 concentration at surface vicinity. This will increase the corrosion rate on a bare metal surface.

In Figure 1.9 the current density dependence on increasing flow rate is shown. The straight part illustrates the limiting current density.

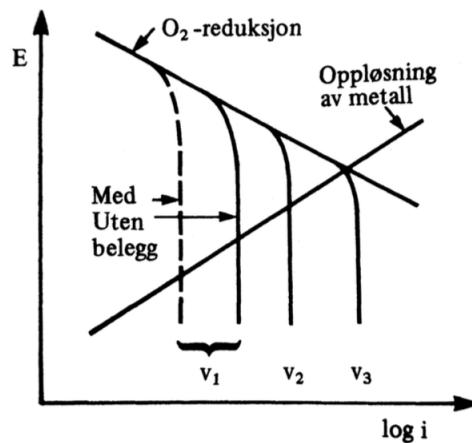


Figure 1.9: Illustration of how increasing flow rate of seawater will affect the limiting current density with and without coating [5].

The limiting current density is expressed in Equation 1.23.

$$i_g = DzF \frac{c_B}{\delta} \quad (1.23)$$

Where, D is the diffusion coefficient, z the amount of electrons in the equilibrium equation, c_B is the O_2 bulk concentration and δ is the thickness of the diffusion layer.

The coating will act as a barrier between seawater and the metal surface, and how resistant the coating is against diffusion of ions will dominate the corrosion rate. The dashed line in Figure 1.9

illustrates that coated surfaces are not affected by increased flow velocity [5]. While in the case of metal surfaces, Figure 1.9 shows that with increasing flow rate the corrosion current density will increase simultaneously [5].

For passive metals, such as SDSS and NAB, the oxide layer will protect the metal surface against increasing O₂ diffusion affecting the corrosion rate. When reaching a certain flow rate the shear stress may be sufficient to degrade the oxide layer and the high flow rate will cause erosion degradation [40]. Critical velocity for NAB is approximately 25 m/s, while a velocity limit for SDSS was difficult to obtain from literature. According to an experiment performed on SDSS with flowing seawater up to 30 m/s in 30 °C showed no signs of corrosion attacks on the surface after 30 days of exposure [41].

High flow velocity may affect both biofilm formation and calcareous deposits when cathodically protected. The critical velocity for biofilm formed was suggested by Compere and Le Bozec (1997) to be approximately 2 m/s [17]. After immersing materials to seawater, the formation of biofilm will lead to slowly increasing potential. The time before reaching steady potential was experienced to be longer for turbulent flow than for laminar flow. A potential difference of about 50 mV was found between the two flowing conditions, showing turbulent flow has the lowest value. This indicates the formation of biofilm is limited by the increasing flow velocity, i.e. lower ennoblement of the material [17]. Research presented by Li, Ciu and Du (2015) shows that carbon steel experienced increased corrosion potential when subjected to a higher flow rate of seawater, attributing to that the calcareous formation on the surface was hampered by the flowing seawater [42].

1.4.8 Tribological Contact Between Two Surfaces

According to Muñoz and Espallargas (2011), sliding contact is defined as two surfaces in continuous movement relative to each other. Two surfaces in contact are defined as two-body contact. While when using a coating the system is defined as three body contact [43]. Tribological contact between two surfaces is characterized by operational and material parameters, environmental conditions and lubricant properties [44]. Sliding motion between two bare metal surfaces can cause challenges like wear, heat generation in the metal and energy loss due to friction between the surfaces [9].

Friction

Friction will arise as a consequence of shear forces acting in the opposite direction of the sliding motion. Friction can be divided into static and dynamic friction. Static friction is often found

to be higher upon sliding commences due to adhesive forces, thereafter dynamic friction will dominate, and the overall resistance will decrease [45]. Higher static friction compared to dynamic friction will promote stick-slip motion. This occurs as the surfaces are subjected to continuously adhesion as the sliding proceeds, this will give an oscillating coefficient of friction (COF) [45]. The degree of friction is characterized by using COF which is a dimensionless value, that is defined as a relationship between friction force and normal load [46]. The dynamic friction is expressed in Equation 1.24 including deformation and an adhesion term.

$$\mu_{tot} = \mu_{pl} + \mu_{ad} \quad (1.24)$$

COF is dependent on the system parameters and environmental conditions during testing, and it is as such not a material parameter [45]. Guillaume Amontons published in 1699 an empirical law found for friction in sliding contact saying that tangential frictional force is proportional to the applied normal force that attributes to elastic deformation of the contact [47, 48]. Research performed by Bowden and Tabor (1938) revealed that not only elastic deformation of the asperities occurs, but they are plastically deformed when being exposed against a sliding counter surface. They found that as plastic deformation carries on the real contact area increases. This was then used to explain Amontons's observation about increased friction with increased applied load [48]. It has also been found that friction is close to independent to sliding velocity when the sliding is dominated by dynamic friction [45].

All surfaces hold a certain surface roughness giving a real contact area, even after being carefully prepared. Figure 1.10 illustrates the surface morphology of a ground sample. It is seen that the real contact area is significantly smaller compared to the apparent contact area due to asperities.

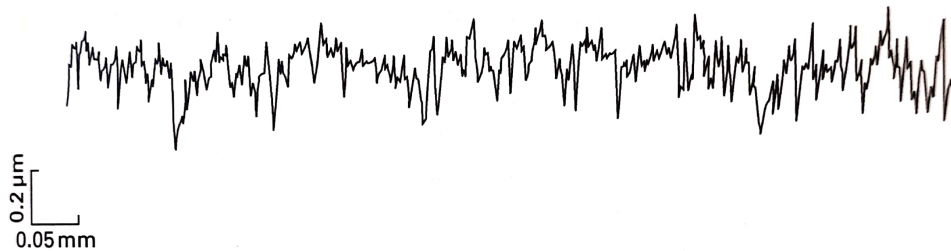


Figure 1.10: Illustration of a typical Gaussian distribution of asperity heights obtained after grinding [7].

To define the extent of surface roughness, an average value (R_A) and a root mean square (R_q) is used. R_A and R_q are closely related, but R_q is more sensitive to peaks and valleys as seen from Equation 1.25 [45].

$$R_q = \sqrt{\frac{1}{n} \sum_{i=1}^n (z_i - z)^2} \quad (1.25)$$

The degree of friction is dependent on the materials mechanical properties and the state of the surfaces. Harder materials such as metal against metal will give lower real contact area, while softer materials such as polymers will yield easier, hence give higher real contact area [47]. Friction has shown to reach steady-state after some time attributing to a running-in period where asperities are worn off giving a smoother surface, this gives lower contact pressure and decreased local temperature as asperity interaction is reduced [44].

Hertzian Contact Pressure

A combination of elastic and plastic deformation of asperities is expected during sliding. Hertzian contact pressure is used to approximate the contact pressure when assuming elastic deformation will occur in the contact [7]. In order to use Hertzian stress equations, reduced elastic modulus (E') and reduced radius of curvature (R') must be found. E' and R' can be found by using Equation 1.26 and Equation 1.27, respectively.

$$\frac{1}{E'} = \frac{1}{E_x} + \frac{1}{E_y} \quad (1.26)$$

$$\frac{1}{R'} = \frac{1}{R_a} + \frac{1}{R_b} \quad (1.27)$$

The elastic stress depends on the type of contact, where the shape of the surfaces will decide the type of contact. Maximum stress can be found by using formulas in Equation 1.28 for point contact and Equation 1.30 for line contact.

$$P_{max} = \frac{3W}{2\pi a^2} \quad (1.28)$$

W is the normal load and a is the elastic contact area which can be calculated from Equation 1.29.

$$a = \left(\frac{3WR'}{E'}\right)^{\frac{1}{3}} \quad (1.29)$$

For line contact Equation 1.30 and Equation 1.31 are used.

$$P_{max} = \frac{W}{\pi bl} \quad (1.30)$$

$$b = \left(\frac{4WR'}{\pi l E'} \right)^{\frac{1}{2}} \quad (1.31)$$

Where b is the half width of the contact rectangle and i is the half length of the contact rectangle. During sliding, the maximum shear stress acting in the material is of interest. If shear stress converges the yield strength the material may be subjected to plastic deformations. Hertzian contact pressure is used to calculate the maximum shear stress, and thereafter the depth at where the maximum shear stress will occur can be approximated [9]. When having coating on top of substrate, the location of the maximum shear stress can be of particular interest, as the yield strength of coating and substrate can be significantly different. Maximum shear stress inside the substrate or in the substrate-coating interface may induce detachment of the coating (i.e. adhesive wear). While maximum shear stress inside the coating or on coating surface will induce fracture of the coating (i.e. cohesive wear) [49].

Maximum shear stress and the location of the maximum shear stress can be found by using Equation 1.32 for point contact and Equation 1.33 for line contact.

$$\tau_{max} = 0.33P_{max} \quad z = 0.63a \quad (1.32)$$

$$\tau_{max} = 0.3P_{max} \quad z = 0.78b \quad (1.33)$$

Wear and Lubrication Regime

The extent of wear of materials is critical in terms of the materials lifetime. Wear is often divided into four main wear mechanisms: adhesive, abrasion, fatigue and tribochemical wear [43].

Archard's formulae given in Equation 1.34 can be used to express the extent of wear per applied force, i.e. wear rate.

$$w_s = \frac{V}{WL} \left[\frac{mm^3}{Nmm} \right] \quad (1.34)$$

Wear is, same as COF, a system parameter. Wear rate is expressed by volume loss (V), applied force (W) and total sliding length (L). In presence of seawater acting as a liquid lubricant, Stribeck curve presented in Figure 1.11 can be used to determine the lubrication regime expected [8]. The lubrication regime dominating in a sliding system will determine the extent of wear expected, depending on system parameters such as viscosity of the lubricant, sliding speed and pressure. Though it should be noted that the Stribeck curve is based on smooth surfaces (i.e. grinded and polished) and without plastic deformation. In the hydrodynamic lubrication regime, a lubrication film separates the sliding surfaces leading to reduced wear. While in boundary regime and mixed lubrication regime the lubrication film is not sufficient to completely separate the two surfaces, hence wear is expected. High contact pressure and low sliding speed will be dominated by boundary regime or mixed regime [8].

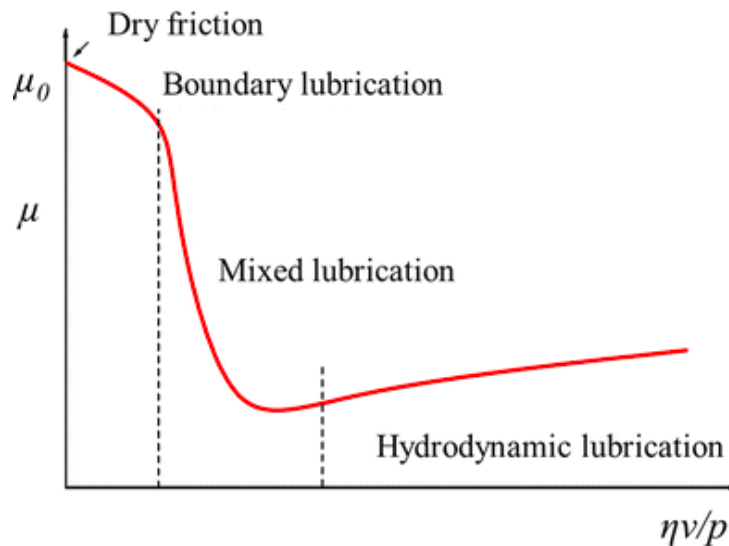


Figure 1.11: The Stribeck curve displays how the lubrication regime depends on the viscosity of the lubricant, sliding speed and applied load [8].

The relationship between the degree of friction and Sommerfeldt number is used to obtain different regimes. μ is the friction, η is in this case viscosity of seawater, ν is sliding speed and

p is pressure [8]. Increasing normal load will enhance the extent of wear due to increased real contact area, though this also depends on the hardness of the material. Higher hardness gives higher resistance against abrasion [45].

1.4.9 25 Cr Stainless Steel Against Nickel-Aluminium Bronze

Adhesive forces will dominate the contact during metal against metal sliding. Metallurgical compatible metals should as such be avoided to reduce the adhesive wear. Base metals in SDSS and NAB, Fe and Cu, respectively, are only partially compatible [7]. Lubrication in the sliding contact will further decrease the adhesive forces occurring. An oxidation layer will, in addition, hamper adhesion between the surfaces [44]. Figure 1.12 shows a photograph of the uncoated SDSS power screw and the NAB nut.



Figure 1.12: Photograph showing the uncoated SDSS power screw and the NAB nut.

Research performed by Jin et al. (2016) tested the tribological behavior of a Cu-alloy against AISI 52100 steel surface immersed in seawater at various loads and sliding speed. The Cu-alloy used was Cu-9Al-5Ni-4Fe-Mn alloy, similar to that used in the nut. Lower COF appeared for the Cu-alloy, but showed higher wear rate when increasing the load from 10 N to 30 N. For increased sliding speed both COF and wear rate were reduced up to the maximum speed tests, approximately 0.085 m/s. CaCO_3 and $\text{Mg}(\text{OH})$ were detected on the Cu-alloy surface after being tested in seawater. This was ascribed to contribute to the reduced COF and wear rate as these compounds will separate the two metals and will reduce ploughing of the softer metal. In

addition, Cu and Al were detected on the steel surface forming a transfer layer with the softer parts of the alloy, which will contribute to lower the COF and wear rate [50].

1.4.10 Xylan Coated 25 Cr Stainless Steel Against Nickel-Aluminium Bronze

Tribological contact containing polymer surface differs from metal against metal contact and will experience different wear mechanisms. The ploughing term in Equation 1.24 is related to the ploughing of hard asperities into the softer material. Adhesion will occur between the asperities creating the real contact area during sliding and junctions will be formed. The resistance against further sliding will depend on the shear strength of the junctions. When applying lower loads, ploughing contribution to the friction can be neglected. Then the friction is explained only by the junctions formed [51]. The cohesive force of the polymer may be lower than the strength of the formed junction, resulting in fracture of bulk polymer [52].

In contact between a polymer and a harder metal surface, a layer of polymer may transfer onto the opposing surface forming a transfer layer. This will affect the friction, leading to a steady-state COF [53]. Formation of transfer film depends on the adhesion of the wear particles onto the opposing surface. Adhesion can be obtained by either mechanical interlocking of particles into valleys of the metal or chemical reaction between the particles and metal surface [54]. In tribological contacts, a thin and soft coating on a harder substrate is advantageous to combine the wanted properties of both materials. Mechanical properties of the substrate will dominate the contact ensuring low real contact area simultaneously as a thin soft coating will provide lubrication [9]. Mechanical properties for the materials are provided in Table 1.2 showing a beneficial tribological contact. According to the producer's datasheet provided in Appendix E, xylan 1052 coating should withstand a pressure of 150 000 psi, corresponding to approximately 1 GPa.

Table 1.2: Mechanical properties of 25 Cr stainless steel [10], nickel-aluminium bronze [3], PTFE [11, 12] and 316 stainless steel [13].

Materials	Elastic Modulus [GPa]	Poisson Ratio	Hardness [HRB]
Super duplex	200	0.3	303
NiAl bronze	125	0.32	93
PTFE	0.54	0.42	20-40
316 SS	193	0.3	95

1.4.11 Xylan Coating

Xylan 1052 is a composite with organic polytetrafluoroethylene (PTFE) matrix filled with inorganic molybdenum disulfide MoS_2 . PTFE acts as a lubricant by being a low surface energy material consisting of a partly crystalline structure where parts of the crystalline structure are surrounded by amorphous structure. The amorphous structure is a relatively weak layer providing the lubrication property of PTFE due to low COF but suffers from high wear rate when used without additives [9]. According to Shibo Wang et al. (2013), the high wear rate for pure PTFE is a result of low surface energy which hinders transfer film formation on the opposing surface [55]. While according to research published by Wang and Yan (2006), PTFE produces bigger wear debris compared to PTFE composites, forming a discontinuous patched transfer film when using a reciprocating tribotest. The research concluded that particles from pure PTFE were bigger and were then moved out from the wear track before creating a transfer film. While after adding MoS_2 the particles were smaller and more easily formed a transfer film. In addition, adhesion of the film formed was enhanced, contributing to the increased wear life [56]. Wear rate of 15 vol% MoS_2 filled PTFE showed to be more than 6 times more wear resistant compared to pure PTFE. MoS_2 is a transition metal dichalcogenides where the transition metal (Mo) is surrounded by dichalcogenides (S) forming a hexagonal structure. Weak van der Waals between the layers in the structure provides the easy shear property. This mechanism is illustrated in Figure 1.13.

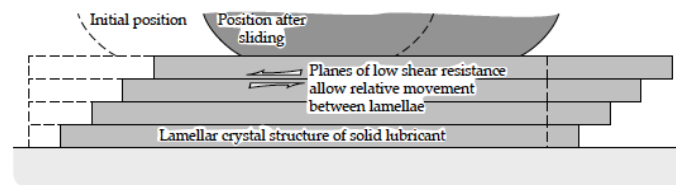


Figure 1.13: Lubrication mechanism of MoS_2 displaying the easy shear property of the material [9].

During the reciprocating test, MoS_2 filled PTFE had a COF of approximately 0.15, subjected to a sudden increase in COF after 4500 cycles, this increase occurred immediately after sliding commenced for pure PTFE when applying 44 MPa normal load. Xylan 1052 is according to the producer used to provide low friction in heavily loaded systems where the sliding speed is low, see datasheet in Appendix E.

1.4.12 Tribocorrosion

Total wear of sliding contact between two bare metal surfaces immersed in seawater must be considered with the combined effect from mechanical wear and degradation due to electrochemical

reactions [43]. During sliding against passive metals, the passive layer will be degraded exposing active metal surface to the seawater. The wear track will then be active acting as anode, while the passive layer around is still intact and act as cathode. Anodic dissolution of the metal will again form the passive layer is formed again i.e. repassivation [43].

Experience from the industry where an uncoated SDSS rod was used as a piston rod, has shown to hold high resistance against tribocorrosion degradation. Johnsen and von der Ohe (2011) presents two different examples where uncoated SDSS rod was installed as a piston rod in 2004 and 2007 which still remains intact. The authors proposed that this was due to the ability of SDSS to form a stable passive film in seawater [57]. As NAB also holds a passive layer in seawater, transition from passive to active state is expected during sliding. This is supported by Zhang, Wang, Yuan, and Yan (2017) [58]. Results when studying tribocorrosion behavior between NAB and aluminium oxide (Al_2O_3) at different pH in artificial seawater was studied. Fluctuating polarization curve for NAB exposed to tribocorrosion is obtained, where the fluctuation was ascribed as a result of the removal and repassivation of the passive film during the pin-on-disk test. Corrosion current density for the static condition was observed to be 40.1 mA m^{-2} and during wear 340.6 mA m^{-2} at pH of 8.2. This is a significant increase in corrosion rate with a combination of corrosion and wear, but due to fluctuations in the polarization curve, the high degree of corrosion may be assumed to occur for only a short period, before repassivating [58].

Chapter 2

Experimental Work

This chapter describes the corrosion experiments conducted at SeaLab NTNU and tribological experiments conducted at Tribology lab at NTNU. Section 2.1 provides information about the materials used and how they were prepared prior to the experiments. Description of instruments used, test environment and configuration of experiments conducted and characterization of test samples are given in Section 2.2 for corrosion experiments and in Section 2.3 for tribology experiments.

Tribology and corrosion experiments have been the main work conducted in order to gather information about what to expect in terms of mechanical and electrochemical degradation of the materials. Long term corrosion experiments were commenced as a part of the preliminary project to study how the materials are affected with time at OCP and when cathodically protected. An effort to simulate the real system has been done to obtain results that can be extrapolated from laboratory results to what to expect when operating the foils over a longer period of time in seawater.

2.1 Material and Sample Preparation

Material specification of material used for corrosion experiments are given in Table 2.1 and Table 2.2 for SDSS and NAB, respectively. Substrate of the xylan coated samples is of the same kind as given in Table 2.1. Datasheet for the xylan 1052 coating is given in Appendix E.

25 Cr Stainless Steel

5x5 cm² tests samples of the type UNS S32750 were used for corrosion and tribocorrosion experiments. Electrical contact when immersed in seawater chamber was obtained by using a platina (Pt) wire throughout the corrosion experiments. Chemical composition of the alloy is given in Table 2.1, and the material certificate is provided in Appendix F. 25 Cr stainless steel samples used for tribocorrosion were grinded with a FEPA P500 grinding paper due to significantly uneven surface.

Table 2.1: Chemical composition of the SDSS alloy used for corrosion and tribocorrosion experiments [14].

Element	Cr	Ni	Mo	C	Si
wt.%	25.02	6.87	3.79	0.17	0.38
Element	Mn	Cu	N	P	S
wt.%	0.75	0.27	0.276	0.029	0.001

Nickel-Aluminium Bronze

Material used for corrosion experiments is equivalent to material used in PhD experiments performed by Hedda Nordby Krogstad (2017), and the material specification is gathered from this publication [14]. Nickel-aluminium plates with dimension of 4x4 cm² was immersed in seawater chamber by using steel sample pins. Isolation strap and Loctite 5926 blue silicone were used to ensure isolation from seawater. NAB samples used in galvanic contact with SDSS were grinded by hand using FEPA P100 and FEPA P500 thereafter they were painted to obtain an SDSS/NAB area relationship between of ≈ 3 .

Production of the nickel-aluminium bronze alloy was according to Krogstad (2017) as follows: NAB alloy was sand cast and cooled to room temperature in the mould. No additional heat treatment was performed [14]. Information about the chemical composition of nickel-aluminium bronze is given in Table 2.2.

Table 2.2: Chemical composition of nickel-aluminium bronze alloy [14].

Element	Cu	Al	Fe	Ni	Cr	Mg
wt.%	80.52	9.44	4.23	5.04	<0.005	<0.01
Element	Mn	Pb	Sn	Zn	Si	
wt.%	0.72	<0.01	0.01	0.03	0.02	

Xylan Coated 25 Cr Stainless Steel

5x5 cm² SDSS plates were coated with xylan 1052 by Kaefer Energy AS. A 2x1 cm² artificial defect was made in the coating of two parallels. The damaged area was created by using a knife to manually scrape off the coating and exposing SDSS surface.

For tribology tests, samples were cut into 2.5x2.5 cm². An A Accutom-50 precision saw was used in order to retain the coating. For experiments performed in seawater, a conductive wire was soldered to the exposed SDSS surface on the edge. The edges were then painted for corrosion protection, in addition Loctite 5926 blue silicone was used for further protection.

Counter Surface During Tribology Experiments

Dry tribology experiments were performed by using a 316 SS sphere against SDSS and xylan coated SDSS explained above. The spheres had a diameter of 6 mm. Tribocorrosion experiments were performed by using a NAB cylinder with a diameter of 8 mm and with a length of 15 mm. The material composition is unknown, but is expected to be similar of the composition given for nickel-aluminium bronze samples used for corrosion experiments. Due to the impossibility of obtaining NAB spheres, dry tribotests were performed by using 316 SS spheres.

2.2 Corrosion Experiments

Long term corrosion tests were performed in a seawater chamber at SeaLab NTNU. SDSS and NAB samples were immersed for 157 days, while xylan coated SDSS samples were immersed for 110 days. Samples of each material were freely exposed in the seawater chamber for the whole testing period where the potential development was monitored. SDSS and NAB samples were also cathodically polarized to $-1050 \text{ mV}_{\text{Ag}/\text{AgCl}}$ by the use of a potentiostat to simulate being cathodically protected. While xylan coated SDSS samples were polarized by being coupled to a sacrificial Zn-anode during test period. Xylan coated SDSS was exposed with intact coating and with a $2 \times 1 \text{ cm}^2$ damage in the coating. Galvanic corrosion between SDSS and NAB was tested by creating electric contact between the two materials. Two parallel experiments were performed for each test.

2.2.1 Instruments

Long term corrosion tests were monitored by a datalogger at SeaLab NTNU. A potentiostat MP-75 was used to cathodically polarize the samples to $-1050 \text{ mV}_{\text{Ag}/\text{AgCl}}$ during the test period. A Gamry 600+ potentiostat was used to obtain cathodic and anodic polarization curves. The corroded surfaces were further analyzed by using scanning electron microscope (SEM) along with visual inspection. Pictures were taken by using second electron detector (SED). Elements present on the corroded surfaces were detected by using Energy-dispersive x-ray spectroscopy (EDS). More detailed explanation about the characterization performed is given in Section 2.4.

2.2.2 Test Environment

Experiments were performed in a seawater chamber at SeaLab, localized at the Trondheim Harbour. Natural seawater from Trondheim harbour was used during test period, and was continuously renewed with a flow rate of approximately 0.001 m/s . The seawater inlet to the laboratory is at 80 m depth, providing seawater with a temperature of $10^\circ\text{C} \pm 4^\circ\text{C}$. By using seawater from such a depth minimizes the seasonal variations of the temperature. Salinity of the seawater was 3.4% and with a pH in the range of $7.5 < \text{pH} < 8.2$. The values were not measured throughout the test period, but is assumed to be similar to the information about test environment provided in PhD thesis by Hedda Nordby Krogstad [14].

2.2.3 Test Configuration

How the corrosion experiments were performed is described in this section along with sketches showing the experimental set-up. Photograph of the long term corrosion experimental set-up is given in Appendix C.

Long Term Corrosion Experiments

Each sample were monitored by using a datalogger throughout the test period to obtain information about the potential development. Illustration of the experimental set-up of the logging system during test period is shown in Figure 2.1. The samples were coupled to a resistor providing a resistance to the circuit, before being coupled to the logging system. $1\ \Omega$ and $10\ \Omega$ was used. The freely exposed samples were coupled directly through the resistor and to the logging system. The potential development was measured against a Ag/AgCl reference electrode. A corrosion cell was created by using a Pt counter electrode in order to cathodically polarize. The samples were then coupled through the resistor and in addition coupled to the MP-75 potentiostat depressing the potential to $-1050\ \text{mV}_{\text{Ag/AgCl}}$. Galvanic current and potential developed was measured by creating electrical contact between SDSS and NAB samples.

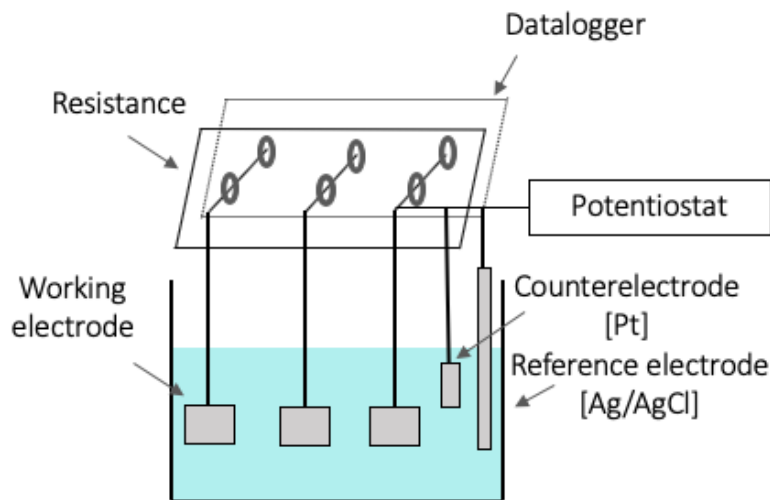


Figure 2.1: Illustration of the experimental set-up of the logging system during long term corrosion experiments conducted at SeaLab.

Polarization Curves

Polarization curves were obtained for SDSS and NAB after being immersed in seawater chamber for 157 days. Illustration of the experimental set-up is shown in Figure 2.2. The corrosion cell contains working electrode (SDSS and NAB), a Pt counter electrode and a Ag/AgCl reference electrode. A Gamry 600+ potentiostat was used to change the potential of the samples in cathodic and in anodic direction in order to measure the correlated current density. For freely exposed SDSS, NAB and xylan coated SDSS, the polarization curves were commenced at the measured OCP over time. The potential was changed with a rate of 600 mV/h from OCP down to $-1100 \text{ mV}_{\text{Ag/AgCl}}$. For the second NAB parallel being freely exposed, anodic polarization curve was obtained by moving the potential from $100 \text{ mV}_{\text{Ag/AgCl}}$ below the measured OCP over time up to $300 \text{ mV}_{\text{Ag/AgCl}}$ above the OCP with a rate of 600 mV/h.

Following polarization curves were obtained:

1. Cathodic polarization of freely exposed SDSS from measured OCP to $-1100 \text{ mV}_{\text{Ag/AgCl}}$.
2. Cathodic polarization of freely exposed NAB from measured OCP to $-1100 \text{ mV}_{\text{Ag/AgCl}}$.
3. Cathodic polarization of freely exposed xylan coated SDSS, from measured OCP to $-1100 \text{ mV}_{\text{Ag/AgCl}}$.
4. Anodic polarization of freely exposed NAB sample from $100 \text{ mV}_{\text{Ag/AgCl}}$ below OCP to $300 \text{ mV}_{\text{Ag/AgCl}}$ above OCP.

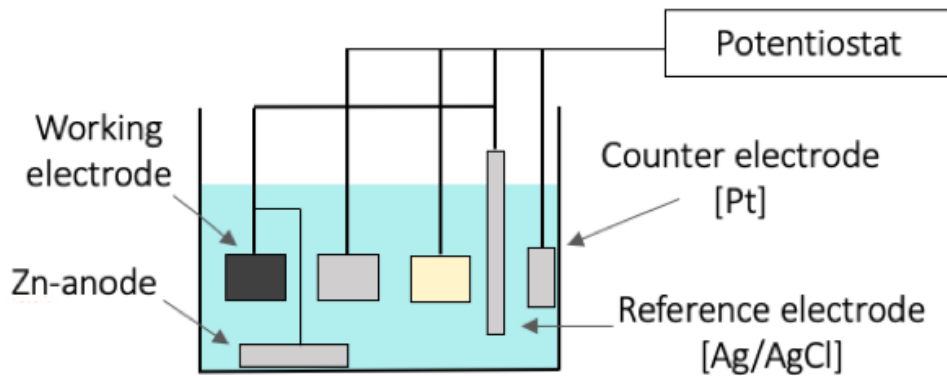


Figure 2.2: Illustration of the set-up when cathodically protected throughout the test period. This illustration also show the set-up used for obtaining cathodic and anodic polarization curves.

2.3 Tribology Experiments

The tribological performance of SDSS, NAB and xylan coated xylan were investigated at the Tribology lab at NTNU. Experiments were performed to obtain an overview of the tribological performance of the coating, and in case of degraded coating, the performance of SDSS and NAB. Reciprocal tests were performed in dry condition and with natural seawater to obtain similar operational condition as expected in full scale. Experiments were performed at OCP and when cathodically polarized. Continuous pin-on-disk experiments were performed to measure dry continuous COF and wear loss at different velocities. Two parallel tests were conducted. If deviating results were measured, more tests were performed.

2.3.1 Instruments

Linear reciprocating wear experiments were performed by using a ResMat Tribocorr machine and TE-38 tribometer at the Tribology lab at NTNU. Experiments were performed in dry condition and when immersed in seawater. Potential development was measured at OCP against a Ag/AgCl reference electrode, while a three electrode corrosion cell was created with a Ag/AgCl reference electrode along with platinum (Pt) counter electrode to measure the current development with time when cathodic polarized to $-1050 \text{ mV}_{\text{Ag/AgCl}}$. A Gamry +600 potentiostat was used for the tribotests. To compare the start/stop-motion with continuous motion, pin-on-disk tests were performed with a CSM Tribometer. Photographs of the different tribometers used are given in Appendix C. Characterization of the worn surfaces were performed by using IFM along with imaging in SEM. Wear profiles obtained in IFM were further used in MountainsMap to obtain the total volume loss of the wear track. Transfer layer on the counter surface were analyzed by using EDS in SEM. Further detailed explanation is given in Section 2.4

2.3.2 Test Environment

The experiments were performed at the Tribology lab at NTNU, with a temperature kept constant at 21°C . Natural seawater from Trondheim harbour was used. Temperature of sample surface was measured continuously to be $\approx 16^\circ\text{C}$ during tribocorrosion experiments conducted in seawater.

2.3.3 Test Configuration

The different experiments conducted at Tribology Lab and the approach will be explained in more detail during this section. Some sketches of the experiments are given. Photographs of the different tribometers and set-up are given in Appendix C.

Dry wear tests

Dry tribology tests were performed with a reciprocal ResMat Tribocorr machine and a continuous CSM pin-on-disk Tribometer to obtain information about the tribological performance of the xylan 1052 coating when applying different loads. An illustration of the set-up of the reciprocal wear test is given in Figure 2.3. 316 stainless steel sphere with a diameter of 6 mm was used as counter surface. The loads used and the corresponding maximum Hertz contact pressure are provided in Table 2.3. Calculations performed to obtain the maximum Hertz contact pressure for point contact are given in Appendix B.

The reciprocal tests were performed with a sliding speed of 0.01 m/s for 1800 s, corresponding to 900 cycles, when applying normal load of 2 N, 10 N, 65 N and 77 N. COF was measured for each cycle. A sketch of the set-up is given in Figure 2.3. To compare the reciprocal movement with continuous movement, pin-on-disk tests were conducted. 2 N and 10 were used for 1800 s, against a 6 mm 316 SS sphere. Tests were performed at 10 rpm and 100 rpm, corresponding to 0.01 m/s and 0.1 m/s, respectively.

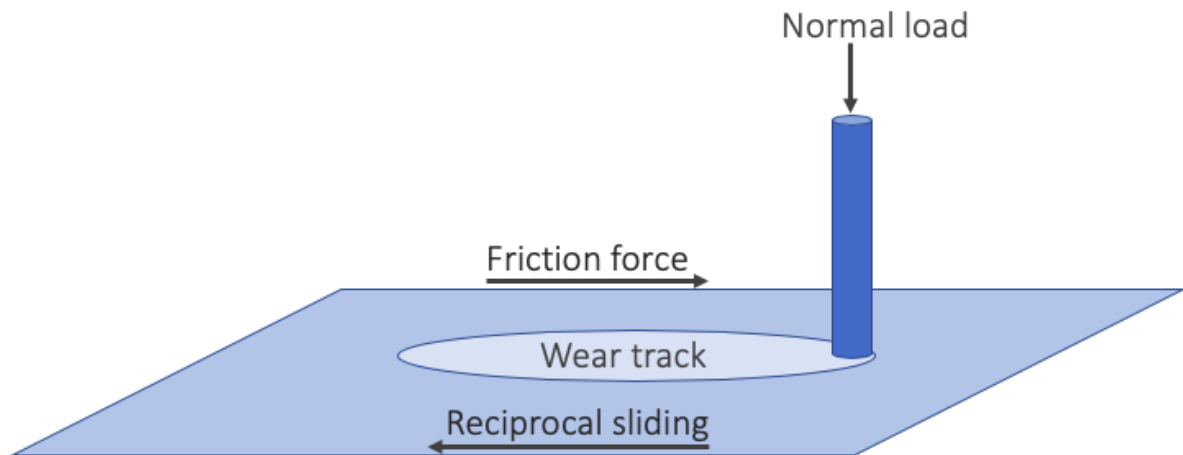


Figure 2.3: Illustration of the set-up for conducting reciprocal wear test.

Table 2.3: Normal loads used for dry wear tests and the corresponding maximum Hertz contact pressure.

Normal load [N]	Hertz contact pressure [MPa]	
	316 SS against Xylan	316 SS against SDSS
2	26.5	779
10	43.8	1371
65	52	1580
77	56	1630

Tribocorrosion

To obtain information about the electrochemical activity of the materials during sliding motion, tribocorrosion tests were conducted with natural seawater. Illustration of the set-up is given in Figure 2.4. Potential development when sliding a NAB cylinder against SDSS surface and xylan coated SDSS surface were measured against a Ag/AgCl reference electrode. A three-electrode cell was created by using a Pt counter electrode to cathodic polarize the materials to $-1050 \text{ mV}_{\text{Ag/AgCl}}$ against a Ag/AgCl reference electrode in order to simulate being cathodically protected. The tribocorrosion experiments were performed by using a TE-38 machine, where the corrosion cell was created inside a custom made PTFE holder for electrical isolation. The tribocorrosion tests were conducted at 10 N with a sliding speed of 0.01 m/s. COF and current density development were measured throughout the test period. Maximum Hertz contact pressure corresponding to the normal load applied when assuming line contact against SDSS and xylan surface are given in Table 2.4. The calculations are provided in Appendix B.

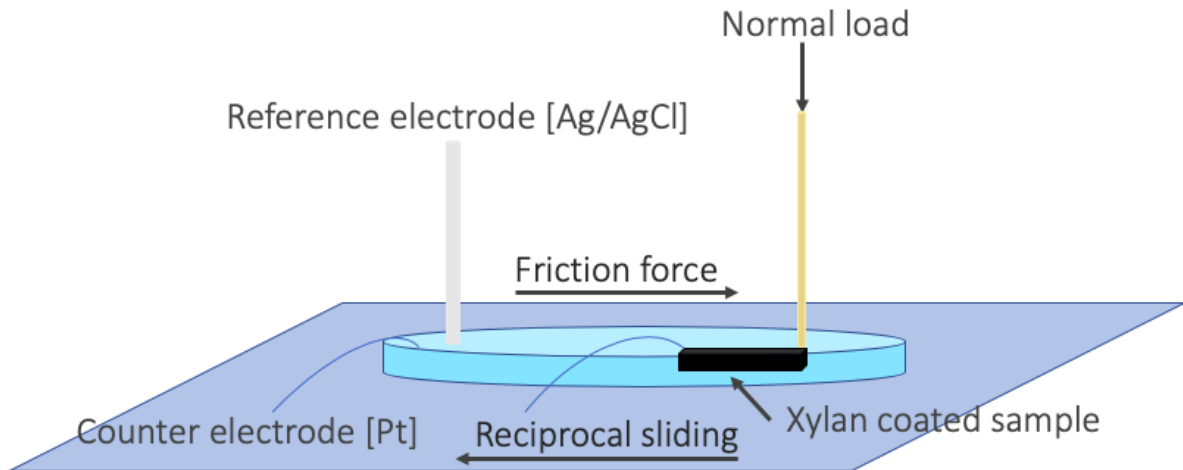


Figure 2.4: Illustration of the set-up for conducting reciprocal wear test in seawater.

Table 2.4: Maximum Hertz contact pressure calculated for line contact against SDSS and xylan surface when applying 10 N.

Material	Hertz contact pressure [MPa]
NAB against xylan	5.89
NAB against SDSS	33.7

2.4 Surface Characterization

IFM was used to obtain an image of the worn surfaces and to measure the depth of the wear track. An average of 2000 points were used to obtain the depth of the wear track. Wear track after pin-on-disk test was only measured for a part of the wear track. This average was then extrapolated to the whole wear track. The wear profile was further used to calculate the volume loss with the help from the software MountainsMap[®] 7. By the use of volume loss the wear rate was calculated by using Equation 1.34. Surface roughness was measured on samples used for reciprocal tribotest at 2 N, and used for pin-on-disk tribotest at 2 N at 0.01 m/s. Figure 1.10 show the surface profile measured for the two samples by using a profilometer. A needle is used to scan the surface roughness to obtain a surface profile showing the real surface roughness and providing information about the average roughness and the root mean square value. The average surface roughness (R_a) and root mean square (R_q) was measured to be 1.07 μm and 1.36 μm , respectively for the upper surface profile, and 1.17 μm and 1.44 μm , respectively for the lower surface profile.

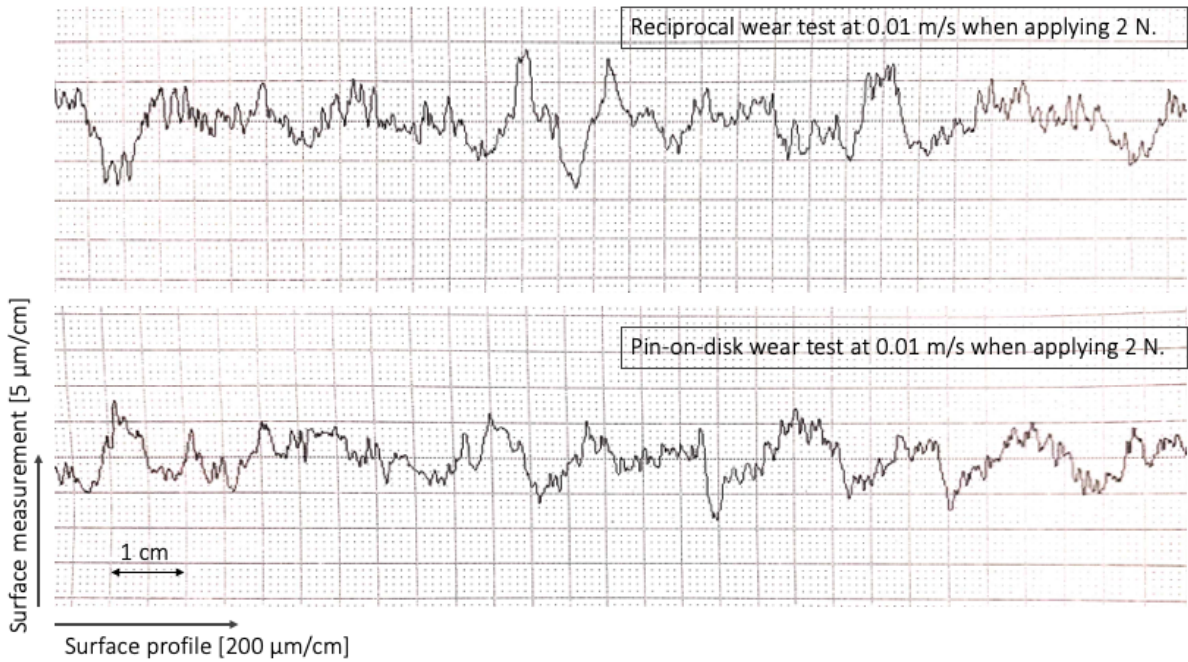


Figure 2.5: Surface profile of two different xylan coated SDSS samples measured by a profilometer.

The coating thickness was further measured in a light microscope after being mounted by epoxy resin. The coating thickness is approximated to be $90\ \mu\text{m}$. The coating is seen between the two red lines displayed on the image.

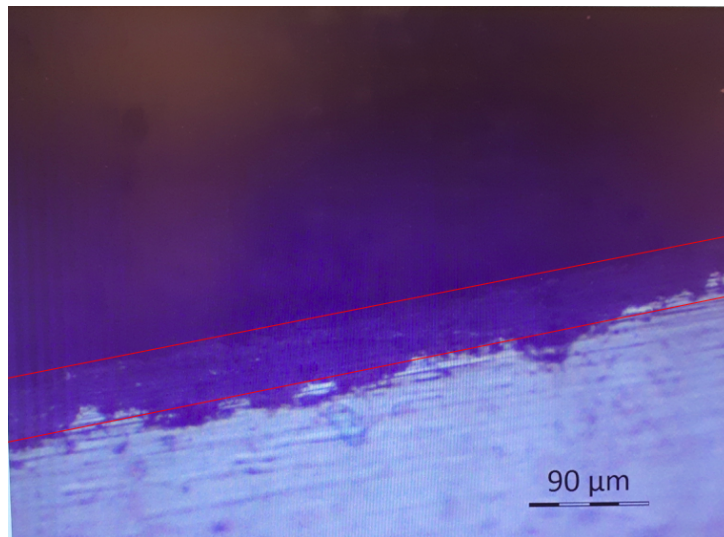


Figure 2.6: A coating thickness of $\approx 90\ \mu\text{m}$ is observed between the two red lines displayed in the image.

SEM Imaging of the Surfaces

The corroded surfaces and wear tracks were imaged by the use of a scanning electron microscope (SEM). The samples were prior to imaging properly cleaned by using ethanol to remove corrosion products, salt particles and other contamination particles. Parameters of the SEM during imaging of the corroded surfaces were as follows: Accelerating voltage of the electron beam was 20 kV, working distance was 10 mm, aperture size was 30 mm and spot size was 3 mm. Image of localized attacks on NAB were obtained at 1000x and 2000x. During imaging of the wear track spot size of 5 mm was used. Images were obtained at 100x and 109x.

EDS analysis

Energy-dispersive X-ray spectroscopy (EDS) was used to detect elements of interest on samples being long term cathodically polarized, and on the counter surfaces used for tribotests. Parameters used during analyzing were as follows: Accelerating voltage of the electron beam was 20 kV, working distance was 10 mm, aperture size was 50 mm and spot size was 5 mm. Figure 2.7 gives an example of EDS analysis showing the main elements present on the surface of a SDSS sample. For cathodically polarized samples the main elements of interest were calcium (Ca) and magnesium (Mg), while for spheres and cylinder used for tribotesting, Molybdenum (Mo), sulphur (S), fluor (F) and carbon (C) forming the xylan coating, were of interest. The SDSS surface was analyzed after tribotest against NAB cylinder when cathodically protected in order to detect Cu elements on the surface.

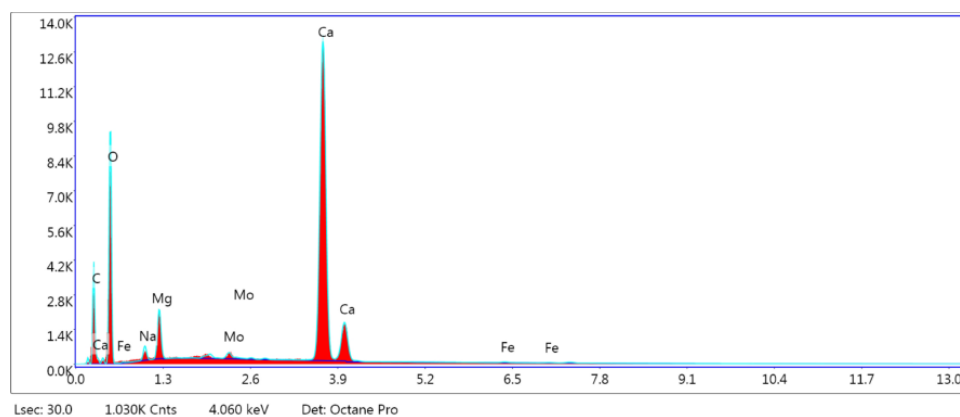


Figure 2.7: Example of EDS result.

2.5 Full-Scale Pilot Project at Fosen

The foil module described in this thesis was mounted on a barge at Fosen harbour on April 9, 2019 by Wavefoil. Information regarding the experiment was given by Erlend Vastveit Nærland at Wavefoil AS. The foils are submerged in seawater and is expected to be extended and retracted on a daily basis. According to Wavefoil, the foils will be extended and retracted with a rotation speed up to 3.4 m/s. Rectangular Al sacrificial anodes are mounted on the module for cathodic protection. The type Coral A-5 type from Skarpenord is used. Anode specifications are given in Table 2.5. Datasheet for the Al-anode is provided in Appendix G.

Table 2.5: Anode specifications are obtained from the supplier, Skarpenord.

Dimensions	L=120 mm, W=70 mm, H=20 mm
Weight (net mass)	0.4 kg
Anode capacity	2585 Ah/kg
Closed circuit potential	-1090 mV _{Ag/AgCl}

Chapter 3

Results

This chapter presents results obtained after performance of corrosion experiments and tribology experiments described in Chapter 2. Section 3.1 contains results from corrosion experiments and Section 3.2 presents results from tribology experiments.

3.1 Long Term Corrosion Experiments

Long term corrosion experiments were performed at SeaLab NTNU in a seawater chamber. The objective of the experiments were to gather information about the properties of SDSS, NAB and xylan coated SDSS when being immersed in seawater over a longer period of time. SDSS and NAB were exposed for 157 days, while xylan coated SDSS were exposed for 110 days. How the materials reacted when being immersed in seawater for a longer period of time at OCP, when cathodically protected and in electrical contact were of special interest. SDSS and NAB where in electrical contact with an area relationship of ≈ 3 .

3.1.1 Freely Exposed at OCP

Potential development of the materials were logged throughout the exposure time, and is plotted against time in Figure 3.1. Measurements of SDSS, NAB and xylan coated SDSS are plotted in same graph for easier comparison. Initial potential and final potential are given in Table 3.1 for SDSS and NAB and in Table 3.2 for xylan coated SDSS. Potential of SDSS when first immersed in seawater chamber was approximately $+160 \text{ mV}_{\text{Ag}/\text{AgCl}}$, but a steep increase in potential is measured immediately after being immersed from day 0 up to day 10. Thereafter, the potential is mildly increasing, converging a potential of $+400 \text{ mV}_{\text{Ag}/\text{AgCl}}$. Xylan coated SDSS shows, similar to SDSS, a steep increase of potential first days of immersion going from $-50 \text{ mV}_{\text{Ag}/\text{AgCl}}$ up to approximately $+180 \text{ mV}_{\text{Ag}/\text{AgCl}}$. Only a mild increase in potential is seen through the test period, reaching a potential of approximately $+200 \text{ mV}_{\text{Ag}/\text{AgCl}}$. Potential of NAB was measured to be $-200 \text{ mV}_{\text{Ag}/\text{AgCl}}$ when first immersed before a mild increase in potential is seen up to day 35. Two notable increase in potential is measured at day 35 and again at day 47. Thereafter, the potential only has a mild increase up to day 157 reaching a potential of approximately $-70 \text{ mV}_{\text{Ag}/\text{AgCl}}$.

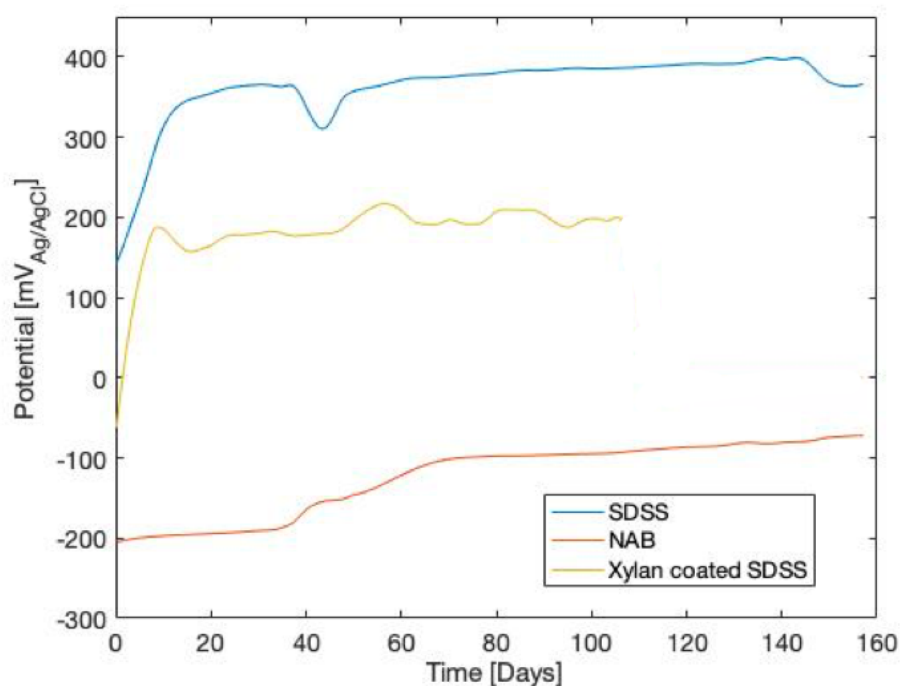


Figure 3.1: Potential development of SDSS and NAB when immersed in seawater chamber for 157 days, and xylan coated SDSS immersed for 110 days.

Table 3.1: OCP value measured for SDSS and NAB when first immersed in seawater and after being exposed for 157 days.

Material	Initial potential	Potential after 157 days
SDSS	+160 mV _{Ag/AgCl}	≈ +400 mV _{Ag/AgCl}
NAB	-200 mV _{Ag/AgCl}	≈ -70 mV _{Ag/AgCl}

Table 3.2: OCP value measured for xylan coated SDSS when first immersed in seawater and after being exposed for 110 days.

Material	Initial potential	Potential after 110 days
Xylan coated SDSS	-50 mV _{Ag/AgCl}	≈ +200 mV _{Ag/AgCl}

Cathodic Polarization Curves

Polarization curves were obtained for SDSS and NAB after 157 days of immersion time, see Figure 3.2. Current density measured when depressing the potential from OCP to -1100 mV_{Ag/AgCl} at a rate of 600 mV/h is plotted in Figure 3.2. Polarization curves obtained at day 42 during preliminary project are marked as SDSS'' and NAB'', while curves obtained at day 157 is marked as SDSS and NAB. SDSS show a more constant increase in current density when depressing the potential from OCP until reaching -500 mV_{Ag/AgCl}. Between -500 mV_{Ag/AgCl} and -900 mV_{Ag/AgCl} the corrosion rate appears to have reached the limiting current density where the current density is not significantly changed. The current density for SDSS'' is measured to mildly increase in this region, while SDSS has a negligible current density change holding a limiting current density of ≈ 100 mA/m². The current density development for NAB is similar to SDSS when depressing the potential from OCP until reaching -400 mV_{Ag/AgCl}. Both NAB and NAB'' holds a similar current density development between -400 mV_{Ag/AgCl} and -800 mV_{Ag/AgCl} with approximately the same limiting current density as SDSS of approximately 100 mA/m². At -800 mV_{Ag/AgCl} and -900 mV_{Ag/AgCl}, the current density increases for NAB and SDSS, respectively. A current density of 700 mA/m² for SDSS and 1100 mA/m² for NAB is measured when holding a potential of -1100 mV_{Ag/AgCl}.

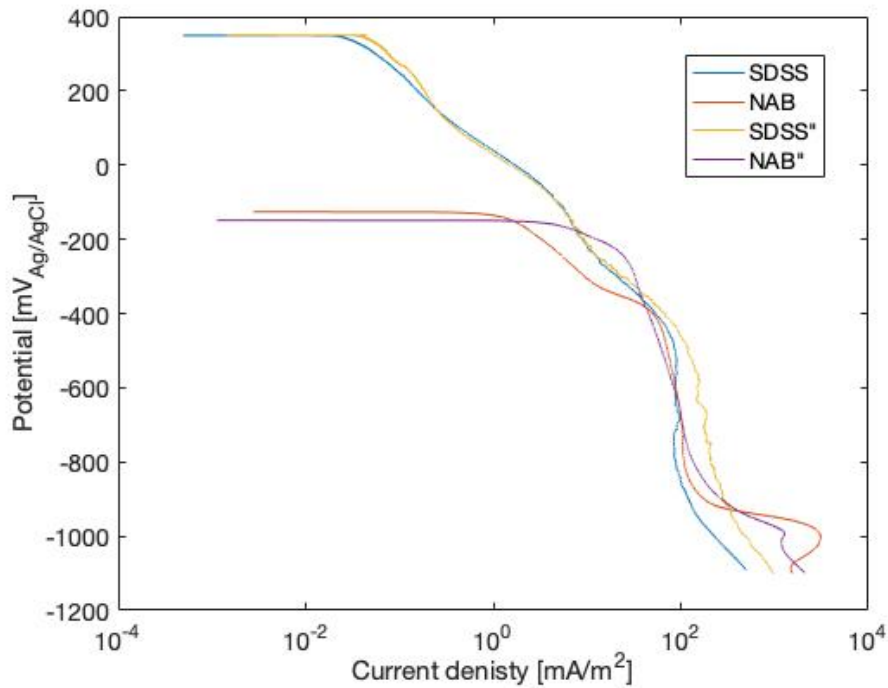


Figure 3.2: Cathodic polarization curves are displayed for freely exposed SDSS and NAB obtained at day 42 (") and day 157 after immersion going from OCP to -1100 mV_{Ag/AgCl}.

Polarization curve for the xylan coated SDSS is given in Figure 3.3. From measured OCP at +200 mV_{Ag/AgCl}, the current density has a constant decrease until reaching -500 mV_{Ag/AgCl} where a shift in potential is measured. Between -500 mV_{Ag/AgCl} and -1000 mV_{Ag/AgCl} an average limiting current density is measured to be 3 mA/m² before a small increase is seen reaching 6 mA/m² at -1100 mV_{Ag/AgCl}. The limiting current density is not as prominent as measured for SDSS and NAB.

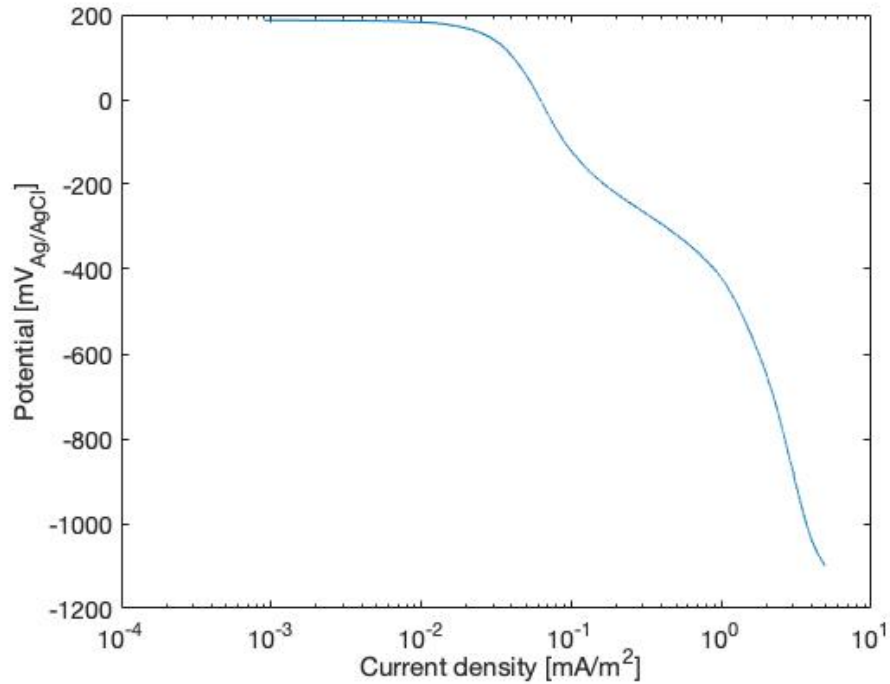


Figure 3.3: Cathodic polarization curve for xylan coated SDSS after being freely exposed in seawater for 110 days. The potential was lowered from OCP to -1100 mV_{Ag/AgCl}.

Anodic Polarization of NAB

The second parallel of freely exposed NAB was anodic polarized at day 157 from 100 mV_{Ag/AgCl} below the measured OCP over time to 300 mV_{Ag/AgCl} above the OCP, see Figure 3.4. Tafel lines were extrapolated from the polarization curve giving information about the corrosion property of NAB provided in Table 3.3. The approximated corrosion current density given by Figure 3.4 was used to calculate the corrosion rate that may be expected. By assuming Cu as the main element, the corrosion rate was calculated by using Faradays law given by Equation 1.6 to be 0.017 mm/year. SEM image of the corroded surface is given in Figure 3.5.

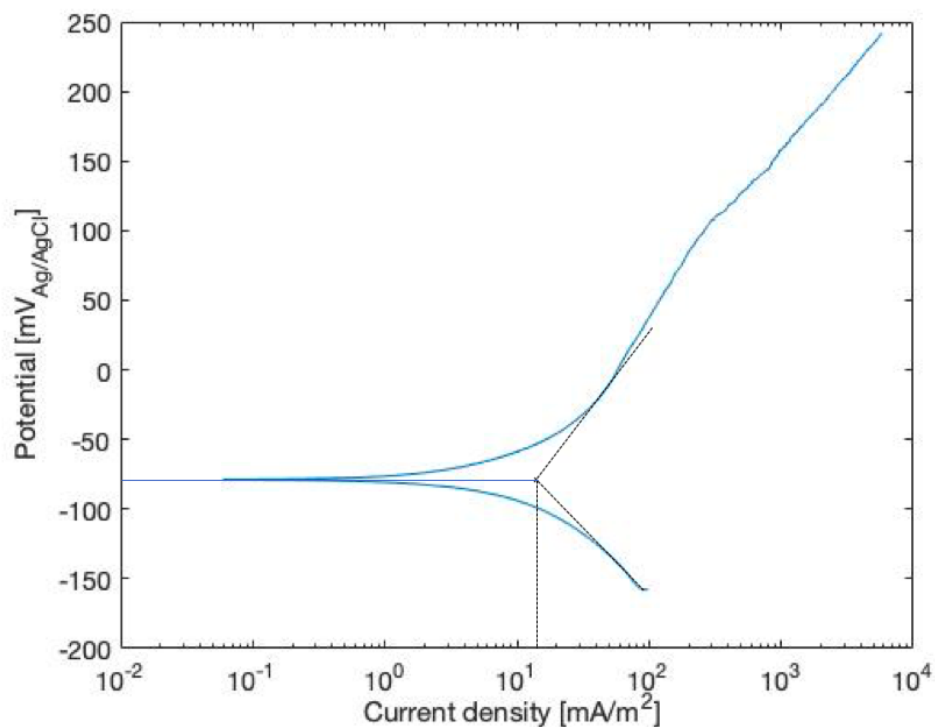


Figure 3.4: Anodic polarization curve of NAB when increasing the potential from 100 mV_{Ag/AgCl} below the measured OCP to 300 mV_{Ag/AgCl} above the OCP. Suggested tafel according to the inclination are displayed providing information about the corrosion properties.

Table 3.3: Corrosion properties approximated by using suggested Tafel lines from anodic polarization curve obtained for freely exposed NAB for 157 days.

Corrosion potential	-80 mV _{Ag/AgCl}
Corrosion current density	15 mA/m ²
Corrosion rate	0.017 mm/year

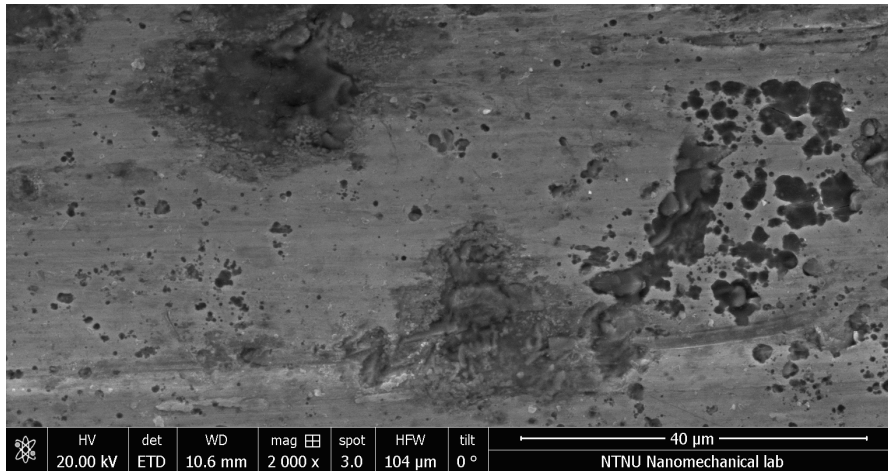


Figure 3.5: SEM image showing the NAB surface after the anodic polarization curve was obtained going from $100 \text{ mV}_{\text{Ag}/\text{AgCl}}$ below the measured OCP to $300 \text{ mV}_{\text{Ag}/\text{AgCl}}$ above the OCP.

3.1.2 Cathodically Polarized SDSS, NAB and Xylan Coated SDSS

SDSS and NAB were polarized to $-1050 \text{ mV}_{\text{Ag}/\text{AgCl}}$ for 157 days to simulate being cathodically protected by using a MP-75 potentiostat. Xylan coated SDSS samples were polarized by being coupled to a Zn-anode. The potential of the Zn-anode was measured to an average of $-1080 \text{ mV}_{\text{Ag}/\text{AgCl}}$ throughout the test period.

Polarized SDSS, NAB and Xylan Coated SDSS

Current density developed for the materials when cathodically polarized is plotted with time in Figure 3.6. The current demand shows a steep decreasing inclination for both SDSS and NAB from day 0, before reaching a more stable value at approximately day 30. Average current density the last 7 days of exposure was $80 \text{ mA}/\text{m}^2$ for SDSS and $75 \text{ mA}/\text{m}^2$ for NAB. Current demand for xylan coated SDSS when coupled to a Zn-anode experienced an increase from day 0 until reaching a stabilized value at day 10. The average current demand measured throughout the test period was $\approx 16 \text{ mA}/\text{m}^2$. Photographs of NAB surface and xylan coated SDSS after being polarized for 157 days and 110 days, respectively are given in Appendix D.

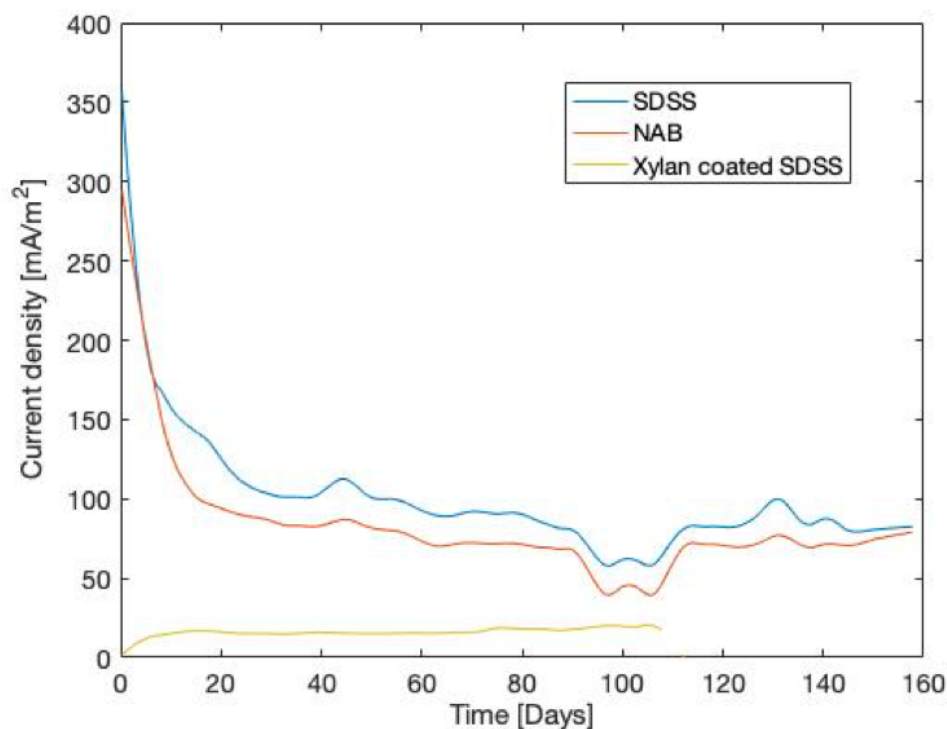


Figure 3.6: Current density demand measured to sustain the potential at $-1050 \text{ mV}_{\text{Ag}/\text{AgCl}}$ for SDSS and NAB, and $-1080 \text{ mV}_{\text{Ag}/\text{AgCl}}$ for xylan coated SDSS.

Xylan 1052 Coated SDSS With Damage Coupled to Zn-Anode

Cathodic current density measured for xylan coated SDSS having a 2 cm^2 damage in the coating is plotted against time in Figure 3.7. The area where the current acts is assumed to be a combination of the xylan surface and exposed SDSS surface. The average current measured is plotted against time, with an average current of $19 \text{ mA}/\text{m}^2$. Photograph showing the surface after being immersed in seawater for 110 days when cathodically protected is given in Appendix D.

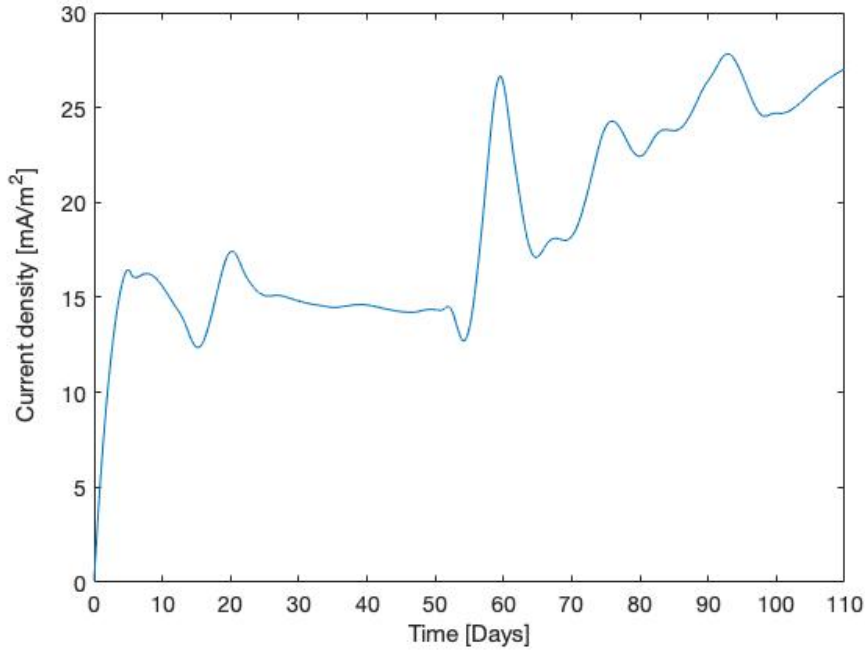


Figure 3.7: Current density demand developed with time to sustain the potential of $-1080 \text{ mV}_{\text{Ag}/\text{AgCl}}$ for xylan coated SDSS sample holding a 2 cm^2 damage.

EDS Measurements

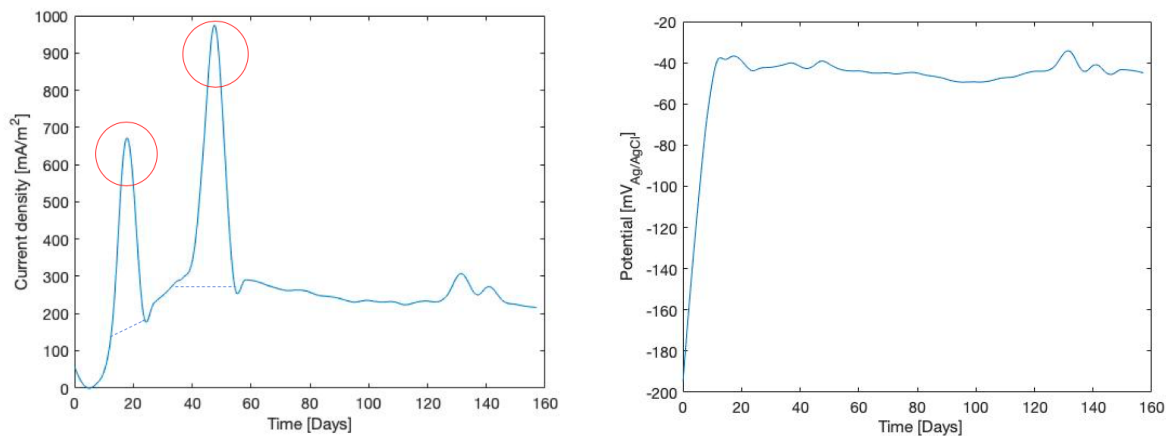
Table 3.4 gives the weight percentage of the elements detected on the samples being cathodically protected. High level of calcium (Ca) was detected on all the polarized surfaces. Highest weight percentage is measured on SDSS with 32.03 wt %. NAB had 30.95 wt % and the damaged area on xylan coated SDSS had 26.17 wt %. The magnesium (Mg) content was significantly lower compared to Ca. On NAB no Mg was detected, while on SDSS there was detected 3.14 wt % and 1.25 wt % for bare SDSS and xylan coated SDSS, respectively. Highest weight percentage was measured for O and a significantly amount of C on the all the surfaces, see Table 3.4.

Table 3.4: Composition of the layer formed on the surface of the polarized samples.

Material	Ca [wt %]	Mg [wt %]	O [wt %]	C [wt %]
SDSS	32.03 ± 0.47	3.14 ± 0.24	49.82 ± 4.95	12.48 ± 0.97
NAB	30.95 ± 0.47	-	53.13 ± 5.25	14.73 ± 1.06
Xylan coated SDSS w/damage	26.17 ± 0.49	1.25 ± 0.13	51.76 ± 5.25	14.98 ± 1.3

3.1.3 Galvanic Current Development

SDSS and NAB were in electric contact with an cathode/anode area ratio of ≈ 3 during the exposure time of 157 days. Galvanic current developed during time is presented in Figure 3.14b. Peaks marked with red are assumed to be measuring error as these peaks are not reflected in the potential development seen in Figure 3.8b. The current development is assumed to be similar to the striped line given in the plot. The average galvanic current measured between day 60 and day 157 is 247 mA/m^2 . By using Cu as the main element in NAB, the corrosion rate was found by using Faradays law provided in Equation 1.6. The corrosion rate was calculated to be 0.28 mm/year . Photographs showing the two parallels are given in Appendix D.



(a) Galvanic current density between SDSS and NAB developed over time. Peaks that are marked red, are assumed to be a measuring error that can be neglected. (b) Galvanic potential developed between SDSS and NAB over time.

Figure 3.8: Galvanic current density and galvanic potential measured during 157 days of electrical contact between SDSS and NAB holding an SDSS/NAB area difference of ≈ 7 .

3.2 Tribological Experiments

Tribology experiments were performed at Tribology lab at NTNU. Dry tests were performed in order to get a better understanding of how the xylan coating reacts when subjected to sliding contact. Tests conducted in seawater were performed at OCP and when cathodic polarized to $-1050 \text{ mV}_{\text{Ag}/\text{AgCl}}$. The actual contact pressure the materials will be exposed to is unknown, therefore an effort has been made to test in different scenarios to provide an overview of what can be expected.

3.2.1 Approximation of the Depth of Maximum Shear Stress

The depth where the maximum shear stress will act can be approximated by using equations for Hertz contact pressure given in Section 1.4.8. The calculated depth of maximum shear stress is provided in Table 3.5. Calculations are provided in Appendix B.

Table 3.5: Depth of the maximum shear stress, z , for the different loading scenarios.

Material contact	2 N	10 N	65 N	77 N
Point load				
316 SS against Xylan	120 μm	208 μm	490 μm	510 μm
316 SS against SDSS	22 μm	37 μm	80 μm	90 μm
Line contact				
NAB against xylan in SW	-	56 μm	-	-
NAB against SDSS in SW	-	4.9 μm	-	-

3.2.2 Dry wear tests

Dry friction of xylan 1052 was tested against 316 SS sphere. COF was measured by applying different normal load, and measuring the corresponding friction load. Reciprocal wear tests and uniform wear tests were conducted to see the effect of having start/stop motion compared to continuous movement.

The measured COF development during the reciprocal tests for different normal loads are shown in Figure 3.9. Applying 2 N normal force appears to provide the highest COF of $\mu=1.7$. One parallel when applying 2 N load show a sudden increase in COF when sliding is commenced. The measurements show that lower COF is obtained for higher contact load. The average COF for the two parallels when applying different loads are given in Table 3.6 along with volume loss and wear rate. Wear rate was calculated by using volume loss obtained from MountainsMap by using Equation 1.34. Increased volume loss is measured from 2 N to 77 N, except 10 N and 65 N measured same volume loss. No clear tendency is seen for the calculated wear rate. Highest wear rate was calculated for 2 N while lowest for 65 N.

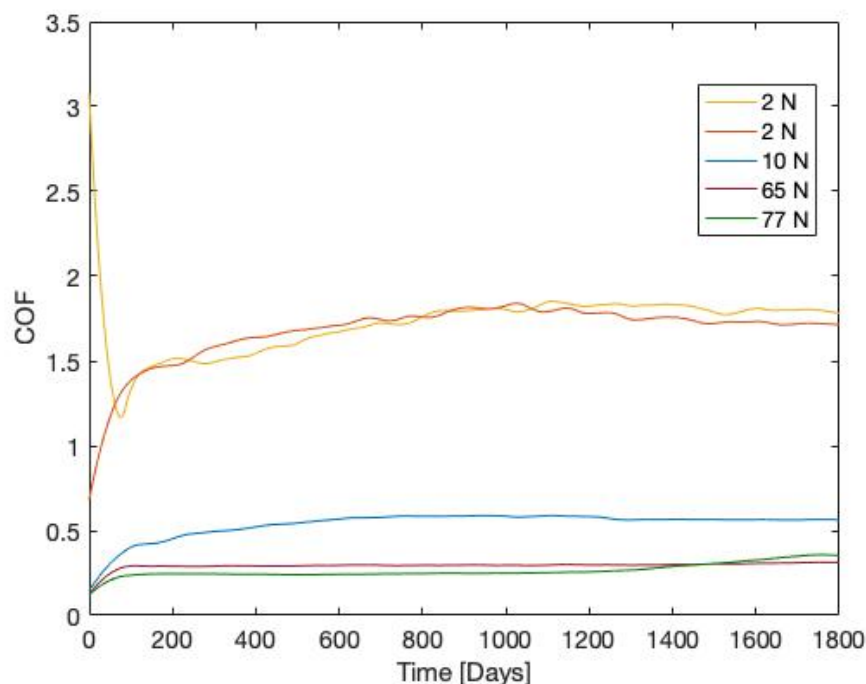


Figure 3.9: Development of the dry COF during reciprocal test between 316 SS and xylan coated SDSS for 1800 s.

Table 3.6: Average COF during test period, volume loss and wear rate for reciprocal test. All tests were conducted with a speed of 0.01 m/s.

Normal force [N]	Reciprocal COF	Volume loss [mm ³]	Wear rate [mm ³ /Nm]
2	1.7	0.048	6.65×10^{-3}
10	0.5	0.07	1.9×10^{-3}
65	0.29	0.069	2.9×10^{-4}
77	0.26	0.47	1.7×10^{-3}

Figure 3.10 gives the COF measured during 1800 s test period for pin-on-disk experiments. Highest COF is measured for for higher rotational speed, and also higher normal load applied. The average COF of two parallels are provided in Table 3.7 for the different parameters used. 100 rpm experience a more prominent increase in COF in the beginning of the test period compared to 10 rpm. When applying 2 N load, lower rotational speed appears to give the highest volume loss, while for 10 N higher rotational speed gives a significant increased volume loss. Lower wear rate is calculated for higher rotational speed, no clear tendency is seen for the wear rate when considering the applied load.

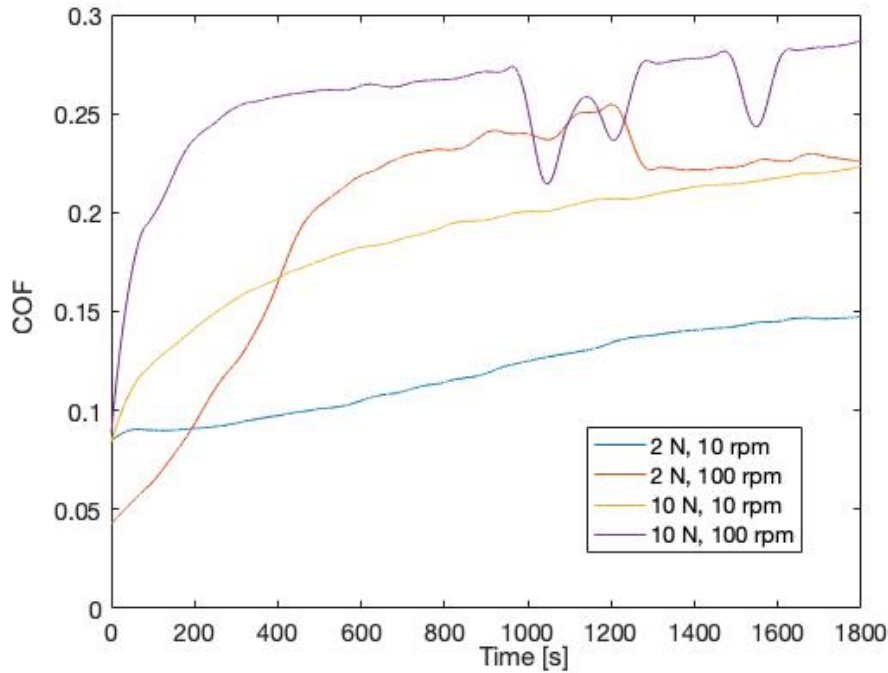


Figure 3.10: Development of the measured dry COF during pin-on-disk experiments between 316 SS sphere and xylan coated SDSS for 1800 s. Rotational speed of 0.01 m/s and 0.1 m/s were used during testing.

Table 3.7: Average COF during test period, volume loss and wear rate for pin-on-disk tests conducted with 0.1 m/s and 0.01 m/s.

Normal force [N]	Speed [m/s]	COF	Volume loss [mm ³]	Wear rate [mm ³ /Nm]
2	0.01	0.12	0.034	9.4×10^{-4}
2	0.1	0.2	0.02	5.5×10^{-5}
10	0.01	0.19	0.047	2.6×10^{-4}
10	0.1	0.26	0.22	1.22×10^{-4}

3.2.3 Reciprocal Experiments in Seawater

Tribocorrosion Experiments Performed at OCP

Development of COF measured during sliding NAB cylinder over the SDSS and xylan coated surface is shown in Figure 3.11. While the measured potential development during sliding is shown in Figure 3.12. Increasing COF is measured for SDSS and xylan coated SDSS during sliding. Average COF was calculated to be 0.23 and 0.25 when sliding NAB cylinder against

SDSS and xylan coated SDSS, respectively. The measured OCP drops to a lower potential when the sliding is commenced after 300 s for both SDSS and xylan coated SDSS. The average OCP during sliding is measured to be approximately $-350 \text{ mV}_{\text{Ag}/\text{AgCl}}$ for SDSS and $-270 \text{ mV}_{\text{Ag}/\text{AgCl}}$ for xylan coated SDSS. The OCP is seen to increase rapidly as the sliding stops.

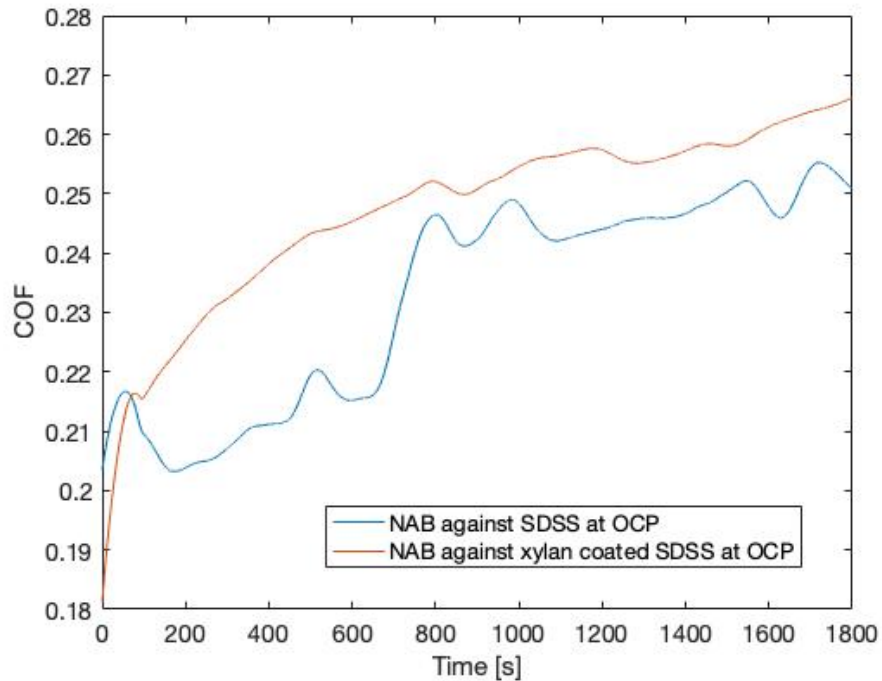


Figure 3.11: Measured COF developed during reciprocal sliding of NAB cylinder against SDSS surface and xylan coated SDSS surface at OCP for 1800 s. A normal load of 10 N was applied.

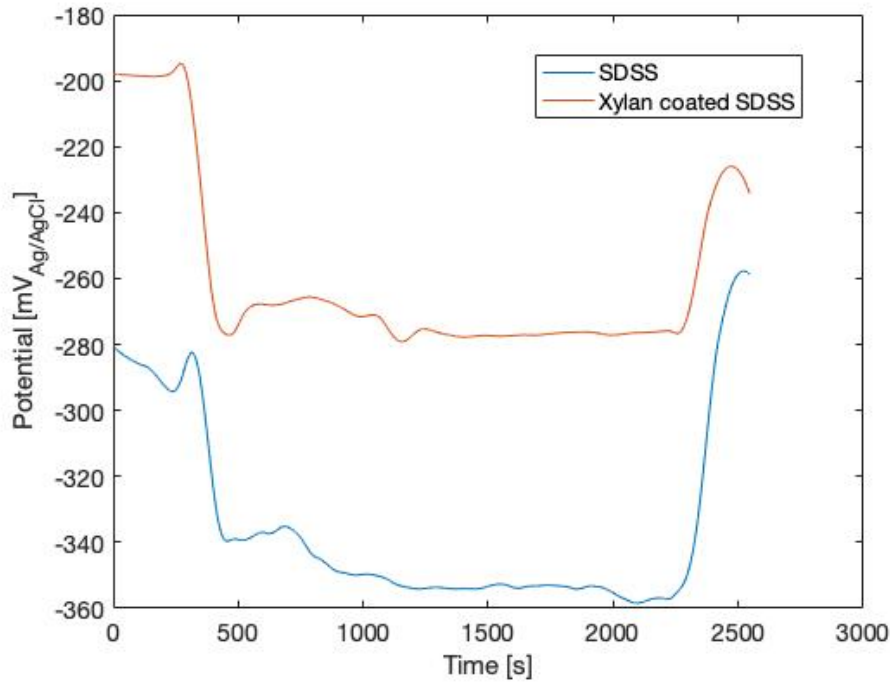


Figure 3.12: OCP development measured during reciprocal sliding of NAB cylinder against SDSS surface and xylan coated SDSS surface for 1800 s at OCP. A normal load of 10 N was applied.

Tribocorrosion Experiments Performed at $-1050 \text{ mV}_{\text{Ag}/\text{AgCl}}$

COF developed during sliding NAB against SDSS and xylan when applying a load of 10 N is presented in Figure 3.13 when cathodic polarized to $-1050 \text{ mV}_{\text{Ag}/\text{AgCl}}$. Table 3.8 gives the average COF during the 1800 s sliding period, where COF for NAB against SDSS was 0.42, while NAB against xylan gave a COF of 0.27. The current needed to keep the potential at $-1050 \text{ mV}_{\text{Ag}/\text{AgCl}}$ is plotted against time for the different surfaces in Figure 3.14. Highest current is measured between NAB and SDSS surface reaching a more stable value at approximately 10 mA. NAB against xylan coating measured a higher current demand compared to NAB against xylan coated SDSS with a damage on the side of the coating, with an average current of 0.78 mA and 0.15 mA, respectively. In addition a test where NAB cylinder slid against xylan coated samples having a damaged area located in the wear track were performed. Average current measured was $6.5 \times 10^{-5} \text{ mA}$ during 1800 s of sliding.

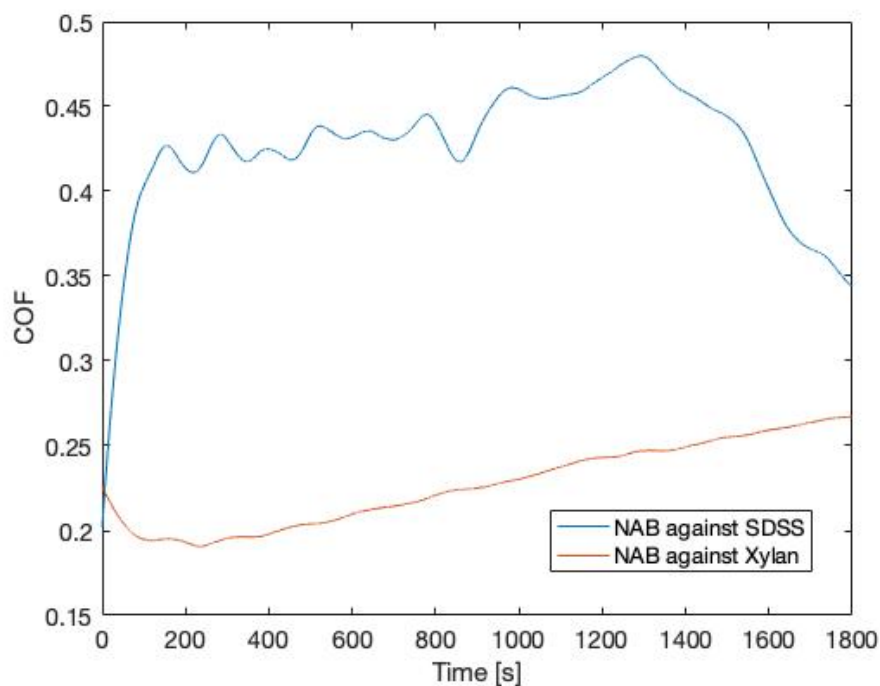
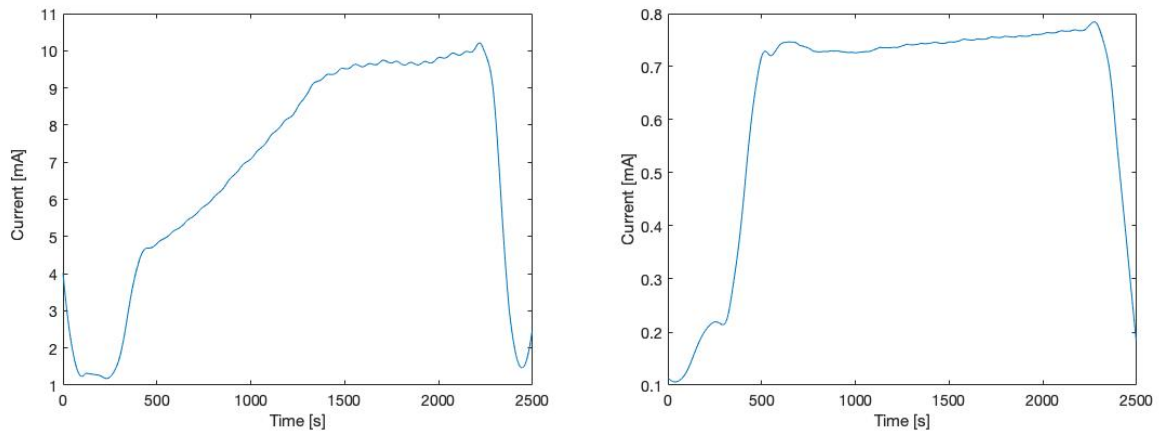


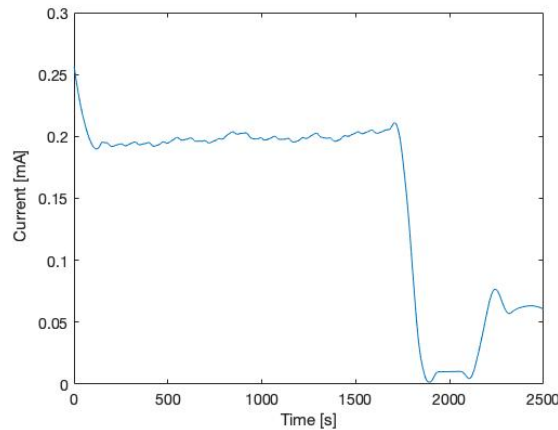
Figure 3.13: COF development during sliding of NAB cylinder against SDSS surface and xylan coated SDSS surface when cathodic polarized $-1050 \text{ mV}_{\text{Ag}/\text{AgCl}}$ for 1800 s. A normal load of 10 N was applied and a sliding speed of 0.01 m/s was used during the experiment.

Table 3.8: Comparison of COF measured during sliding of NAB cylinder against SDSS surface and xylan surface when applying 10 N at 0.01 m/s for 1800 s. COF obtained at OCP and when cathodically protected are given. Average values are calculated.

Material	COF	
	At OCP	When cathodically protected
NAB against SDSS	0.23	0.42
NAB against xylan coating	0.25	0.27



(a) Current measured during sliding contact between NAB and SDSS. (b) Current measured during sliding between NAB and xylan coated SDSS.

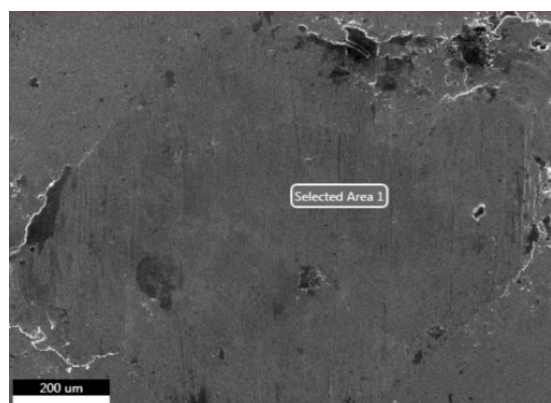


(c) Current measured between NAB and xylan coated SDSS with damaged coating.

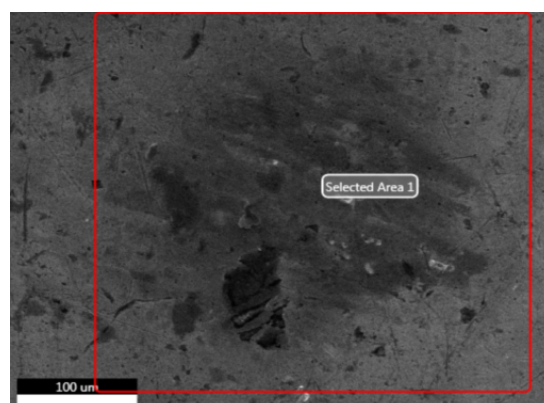
Figure 3.14: Current development when sliding NAB cylinder against different surfaces in seawater. The samples were cathodic polarized to $-1050 \text{ mV}_{\text{Ag}/\text{AgCl}}$ during the sliding period.

Analysis of the Surface of 316 SS Sphere and NAB Cylinder

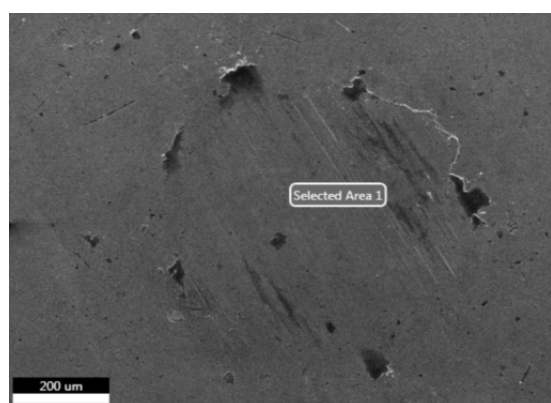
SEM image of the wear track produced on the spheres during dry tribotests are given in Figure 3.15. The images show that different wear tracks are produced during reciprocal movement compared to continuous movement in a pin-on-disk test. A more pronounced wear track is observed for pin-on-disk experiments.



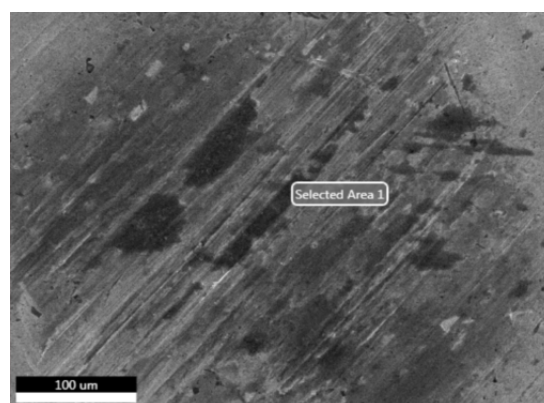
(a) 2 N normal load during dry reciprocal tribotest at 0.01 m/s.



(b) 2 N normal load during dry pin-on-disk tests at 0.01 m/s.



(c) 10 N normal load during dry reciprocal tribotest at 0.01 m/s.



(d) 10 N normal load during dry pin-on-disk tests at 0.01 m/s.

Figure 3.15: SEM image of wear track of the spheres used for counter surface during dry reciprocal tribotests and pin-on-disk experiments.

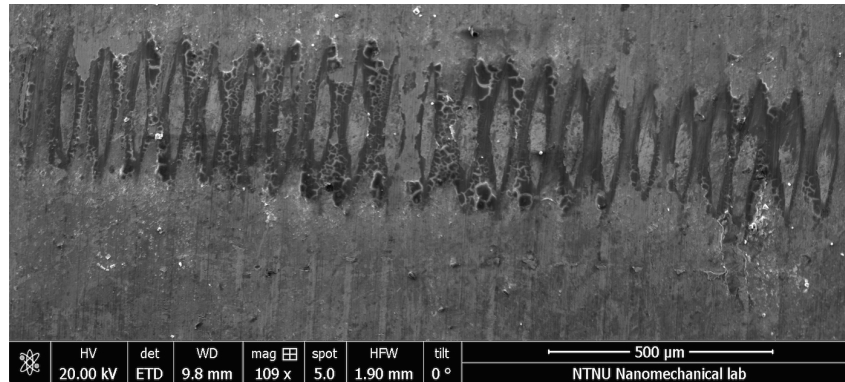
EDS analysis were performed on the spheres and cylinders used for testing at 0.01 m/s. Table 3.9 presents weight percentage of elements detected on the surface of spheres used for dry reciprocal tribotest and continuous pin-on-disk tribotest. The elements of interest were Mo, S, F and C. Higher amount Mo was detected for continuous pin-on-disk test, and increasing amount was detected for higher applied load. No amount of S were detected on any of the samples, while C content showed a more stable weight percentage.

Table 3.9: EDS analysis of spheres used for dry tribotests at 0.01 m/s.

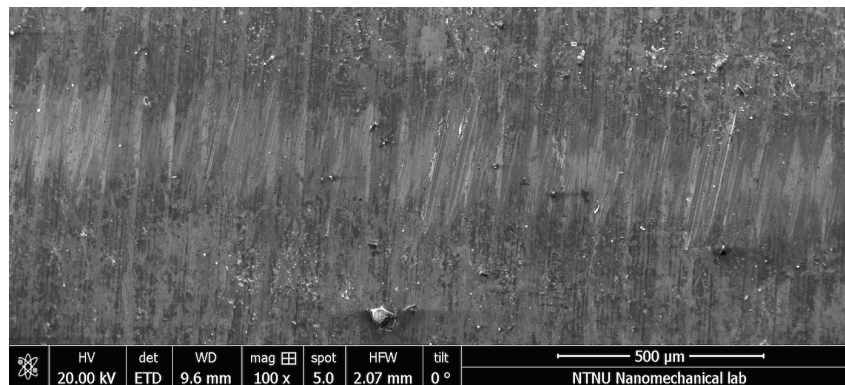
Experiment	Mo [wt %]	S [wt %]	F [wt %]	C [wt %]
Reciprocal test subjected to 2 N	1.88 ± 0.55	-	-	9.37 ± 1.58
Reciprocal test subjected to 10 N	1.86 ± 0.52	-	2.73 ± 0.575	6.27 ± 1.15
Pin-on-disk test subjected to 2 N	2.55 ± 0.54	-	2.11 ± 0.47	9.84 ± 1.6
Pin-on-disk test subjected to 10 N	3.64 ± 0.63	-	1.19 ± 0.36	9.65 ± 1.59

SEM image of the wear track on NAB cylinder surface after reciprocal sliding against SDSS and

xylan are given in Figure 3.16a and Figure 3.16b, respectively. A more pronounced wear track is observed on NAB surface after sliding against SDSS, but a more discontinuous pattern is shown. Wear track of NAB after sliding against xylan is less prominent in the images, but is shown to have created a more continuous wear track. Weight percentage for the detected elements of interest after reciprocal tribocorrosion experiments performed when cathodic polarized to $-1050 \text{ mV}_{\text{Ag}/\text{AgCl}}$ are given in Table 3.10. EDS analysis was in addition performed on the SDSS surface after tribocorrosion experiment against NAB when cathodically protected. The main elements of interest were Cu and Mg. $1.09 \text{ wt}\% \pm 0.16$ of Mg was measured, but no Cu was detected.



(a) Wear track after sliding NAB cylinder against SDSS surface.



(b) Wear track after sliding NAB cylinder against xylan coated SDSS surface.

Figure 3.16: SEM images of wear track obtained on NAB surface after sliding against SDSS and xylan coated SDSS when cathodic polarized to $-1050 \text{ mV}_{\text{Ag}/\text{AgCl}}$.

Table 3.10: EDS analysis of NAB cylinder after performing tribocorrosion experiments in seawater at OCP and when cathodic polarized to $-1050 \text{ mV}_{\text{Ag}/\text{AgCl}}$.

Experiment	Mo [wt %]	S [wt %]	F [wt %]	C [wt %]	Mg [wt %]
NAB against SDSS when CP	-	-	-	-	7.52 ± 0.76
NAB against xylan when CP	-	-	-	9.9 ± 1.09	1.02 ± 0.18

3.3 Full-Scale Pilot Project at Fosen

Photograph of xylan coated power screw after being operated at Fosen harbour for 43 days in seawater is given in Figure 3.17. Information about the full-scale project was obtained from Erlend Vastveit Nærland. Damage from the extension and retraction of the foils are shown on the threads. Figure 3.18 show the NAB nut with Al sacrificial anodes mounted on the nut. The amount sacrificial anodes needed for protecting the SDSS power screw and NAB nut can be approximated by using DNVGL-RP-B401 standard for cathodic protection. Calculations were performed with a coating breakdown factor of 0.84 and when assuming SDSS power screw without coating. Calculations were done by using a conservative current density of 200 mA/m^2 . Coral A-5 Al-anodes with a net mass of 0.4 kg are mounted on the foil module to provide cathodic protection. Average anode mass to protect the NAB nut for 25 years was calculated to be 22. While for the xylan coated SDSS power screw a total amount of 138 anodes are needed when using a breakdown factor of 0.84, while 164 anodes are needed to protect SDSS power screw in case of prematurely degraded xylan coating. The calculations performed are provided in Appendix A.



Figure 3.17: Photograph of the full-scale xylan coated SDSS power screw after operation for 43 days at Fosen harbour. Arrows are given to show examples of areas of degraded coating.

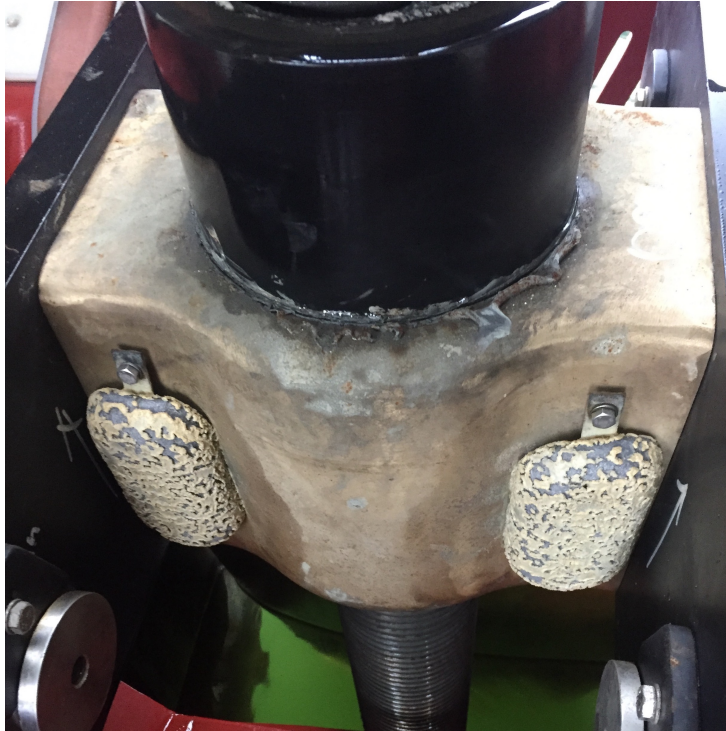


Figure 3.18: Photograph of the NAB nut and the Al sacrificial anodes mounted on NAB surface after being exposed in seawater for 43 days.

Chapter 4

Discussion

In this chapter results presented in Chapter 3 will be discussed according to theory presented in Chapter 1.4. Section 4.1 provides discussion of the corrosion results and discussion about tribology results is given in Section 4.2.

The aim of this discussion is to provide the reader insight into what to expect in terms of corrosion and wear when using xylan coated SDSS power screw connected to a NAB nut in sliding contact when cathodically protected in seawater.

4.1 Corrosion Experiments

SDSS and NAB samples were freely exposed in fresh running seawater from Trondheim harbour for 157 days. Xylan coated SDSS was exposed for 110 days.

4.1.1 OCP Development With Time for SDSS and NAB

The measured potential development for SDSS show a prominent increase in OCP when first immersed in seawater, going from $+160 \text{ mV}_{\text{Ag}/\text{AgCl}}$ to $+400 \text{ mV}_{\text{Ag}/\text{AgCl}}$. This ennoblement is

ascribed to bacteria cells forming on the surface. The bacteria act catalytically on the cathodic reaction, and move the potential curve in the less noble direction accordingly as the cathodic reaction increases. The material is then more vulnerable against corrosion attacks as the arising potential moves closer to the pitting potential. Increased potential of NAB is also measured throughout the test period going from $-200 \text{ mV}_{\text{Ag}/\text{AgCl}}$ up to $-70 \text{ mV}_{\text{Ag}/\text{AgCl}}$. This is in accordance with ennoblement observed by Johnsen and Krogstad (2017). This was attributed by the authors to bacterial cells formed on the surface [25]. However, Figure 3.1 shows that the ennoblement occurs more rapidly for SDSS than for NAB.

4.1.2 Polarization Curves Obtained for SDSS and NAB

Cathodic polarization curves obtained for SDSS at day 42 (marked as SDSS^{''}) and at day 157 (marked as SDSS) show a constant increase in current density when lowering the potential from OCP, see Figure 3.2. This implies that the rate of the corrosion reaction is not limited by the amount O_2 in the vicinity of the sample surface. Hence the corrosion reaction is activation controlled. Biofilm formed on the surface enhances the cathodic reaction and an increase in current density will as such be expected. At $-500 \text{ mV}_{\text{Ag}/\text{AgCl}}$, a shift in potential is seen when reaching the limiting current density. A more prominent potential drop is measured between $-500 \text{ mV}_{\text{Ag}/\text{AgCl}}$ and $-900 \text{ mV}_{\text{Ag}/\text{AgCl}}$. In this region the corrosion reaction is limited by the amount of O_2 available for the cathodic reaction, hence the corrosion reaction is concentration controlled. The polarization curve obtained for SDSS at day 157 show a more defined limiting current density compared to the curve obtained for SDSS^{''} on day 42. This implies that a more pronounced biofilm has been formed acting as a diffusion layer and thus reducing the limiting current density, see Equation 1.23. At lower potentials, according to the Pourbaix diagram, see Figure 1.3 for SDSS, the hydrogen evolution is included in the cathodic reaction. This is seen at about $-900 \text{ mV}_{\text{Ag}/\text{AgCl}}$ where the cathodic current increases.

Current density measured for NAB exhibit a similar tendency as SDSS when decreasing the potential from OCP to $-500 \text{ mV}_{\text{Ag}/\text{AgCl}}$. Ennoblement observed at day 35 during logging of the potential development at OCP is attributed to biofilm formation enhancing the cathodic reaction on the surface. Similar limiting current density is measured when obtaining polarization curves at day 42 (marked as NAB^{''}) and day 157 (marked as NAB) implying that the second ennoblement observed at day 48 during logging of the potential is not due to further biofilm formation. Similar to SDSS, NAB experienced increased current density at lower potentials due to the contribution of hydrogen evolution, see Pourbaix for Cu in Figure 1.5.

Anodic polarization of NAB revealed a corrosion current density of $15 \text{ mA}/\text{m}^2$. By using Faraday's law, a corresponding corrosion rate of $0.017 \text{ m}/\text{year}$ was calculated, see Equation 1.6. By using this equation, the corrosion rate is assumed to occur uniformly on the sample surface. However, the corrosion attacks were observed to mainly act locally. The extent of the corrosion attacks

can be seen in Figure 4.1. NAB contains different intermetallic phases, where the α -phase will act anodic in the presence of seawater and κ -phase will act cathodic. Therefore the calculated corrosion rate of 0.017 mm/year will be superseded to act only in certain areas.

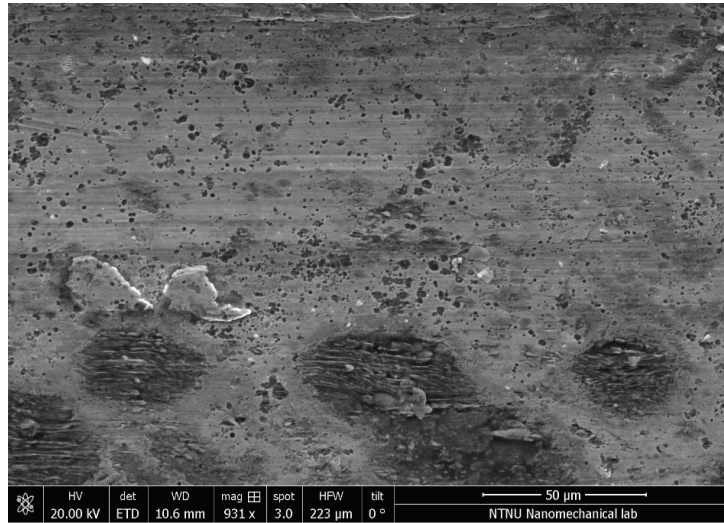


Figure 4.1: SEM image showing the extent of localized corrosion attacks observed on NAB surface after obtaining the anodic polarization curve.

4.1.3 Behaviour of SDSS and NAB When Polarized to $-1050 \text{ mV}_{\text{Ag}/\text{AgCl}}$

Test samples of SDSS and NAB were cathodic polarized to $-1050 \text{ mV}_{\text{Ag}/\text{AgCl}}$ for 157 days. Both SDSS and NAB show a steep decreasing inclination in current density demand from day 0 until day 30. This is designated to calcareous deposits forming on the surfaces. EDS analysis conducted on the surfaces detected a significant weight percentage of Ca on SDSS and NAB surface but Mg was detected only on the SDSS surface, see Table 3.4. CaCO_3 precipitates at a pH level of 7.5, while $\text{Mg}(\text{OH})_2$ precipitates at pH above 10. Hence, a lower amount of Mg is expected. Metal surfaces may exhibit different cathodic efficiency. Current density demand measured during polarization of freely exposed SDSS and NAB was 700 mA/m^2 and 1100 mA/m^2 at a potential of $-1100 \text{ mV}_{\text{Ag}/\text{AgCl}}$. While after being cathodic polarized to $-1050 \text{ mV}_{\text{Ag}/\text{AgCl}}$ for 157 days the current density measured was reduced to 80 mA/m^2 and 75 mA/m^2 for SDSS and NAB, respectively. The lower current demand emphasizes the protective ability of the deposits by inhibiting O_2 from reaching the metal surface. This will then reduce the current density demand needed from the sacrificial anodes. The number of anodes needed for protection can be calculated by using recommended practice, DNVGL-RP-B401, published by DNV [31]. A current density of 200 mA/m^2 was used to have a conservative approach due to the increased limiting current density expected during the movement of the vessel. The higher flow rate of the seawater will move the limiting current density curve to higher current as fresh seawater saturated with O_2 will be available at the surface to be included in the cathodic reaction, see Figure 1.9. In

addition, calcareous deposits protecting the surface may be affected and will increase the current density needed to protect the materials. Anode mass needed to sustain protection throughout 25 years with a current density of 200 mA/m^2 was calculated to be 65.7 kg to protect SDSS and 8.7 kg for NAB. Al-anodes of the type Coral A-5 from Skarpenord has been mounted on the foil module with a net mass of 0.4 kg. This corresponds to a total amount of 186 anodes needed to obtain full corrosion protection for 25 years. Anode mass needed for protection when considering the presence of xylan coating was calculated to be 55 kg. The mean coating breakdown factor (CBF) calculated gave higher value than 1, indicating that the lifetime for the coating is shorter than for the desired lifetime for SDSS and NAB. The CBF was then calculated to be 0.84, see Appendix A for calculations. Number of anodes needed when using CBF of 0.84 was estimated to be 160.

When using NAB with cathodic protection, the antifouling property of the metal will be reduced accordingly as the amount of Cu-ions released is reduced. Biofouling was not observed on the surface by visual inspection, thus it does not appear to be a problem after being protected for 157 days in seawater. This may be a problem at a later point and can cause a challenge in regard to localized corrosion attacks. When sediments accumulate on the surface, seawater between the sediments and the metal surface will not be renewed, i.e. it will cause a stagnant condition. The cathodic reaction under the fouling will proceed until the O_2 concentration converges to zero. If chloride ions are allowed to diffuse through the sediments due to electroneutrality, the metal ions and chlorides will react with water and form HCl acid, see Equation 1.9. This will reduce the pH, creating an aggressive environment, and accelerating the corrosion reaction. SRB bacteria present in seawater may also contribute to the corrosion reaction. SRB will in a stagnant condition reduce sulfate to sulfides. This will, equivalent to when exposed to polluted seawater, transform the passive layer to a porous layer reducing its protective ability.

4.1.4 Galvanic Coupling Between SDSS and NAB

The galvanic current arising between SDSS and NAB was measured to be approximately 70 mA/m^2 . By using Faraday's law, a corrosion rate of 0.28 mm/year was calculated. The area ratio between SDSS and NAB was approximately 3 and showed to promote severe corrosion attacks on the NAB surface. The SDSS surface will be transformed to a cathodic surface in electric contact with NAB. Where a large cathodic surface will result in a high anodic dissolution on the smaller anodic surface. Corrosion products were observed accumulating on the NAB surface throughout the test period. The corrosion products will create an area with stagnant seawater and accelerate the corrosion process further, similar to what explained in Section 4.1.3 for fouling. Corrosion attack with a depth of $592 \mu\text{m}$ was measured on the NAB surface. This is similar to the corrosion attacks of $580 \mu\text{m}$ observed by Oakley (2017) under fouling of protected Cu-alloy. In the foil module, the SDSS power screw has a surface area more than 7

times larger than the NAB nut, and will thus result in higher galvanic current than measured in this experiment. This was also observed by Francis (1999) when comparing 10:1 and 1:1 cathode/anode area relationship. More severe localized attacks were observed for higher area differences. Calcareous deposits will precipitate on the cathodic surface and decrease the galvanic current. This is reflected in the potential development where the potential curve is moved in the noble direction.

The SDSS power screw is coated with xylan 1052 and will when it is intact reduce the cathodic reaction on the power screw surface. During long term experiments, a current of 16 mA/m^2 was measured, and will thus create a galvanic current in connection with NAB. However, the galvanic current will only occur if the cathodic protection for some reason is not sufficient. As long as the materials are cathodically polarized to a potential below its protecting potential the galvanic current will not occur.

4.1.5 Behaviour of Xylan Coated SDSS in Seawater

OCP development for xylan coated SDSS is seen to increase rapidly when first immersed in seawater. This is assumed to be a result of seawater diffusing through the coating, creating an electrochemical potential on the SDSS surface. The initial and final potential measured is provided in Table 3.2.

The polarization curve obtained for xylan coated SDSS is seen to be similar to the curve obtained for SDSS, and the steps throughout the polarization can be explained as for SDSS in Section 4.1.3. The extent of biofilm formation on the xylan surface was not examined. However, it is assumed that some biofilm is formed, which can be seen by the increasing cathodic current measured when lowering the potential from OCP. Lower limiting current density of 3 mA/m^2 was measured for xylan coated SDSS compared to 100 mA/m^2 on SDSS. This reduced limiting current density is assumed to mainly be a result of the coating acting as a diffusion layer. The contribution of the biofilm layer is unknown.

Samples being cathodically polarized throughout the test period developed an average current density of 16 mA/m^2 . The current density measured is higher than the current density measured during cathodic polarization of freely exposed sample of 6 mA/m^2 . Bubble formation was observed on the xylan surface caused by cathodic disbonding of the coating. When acting as cathodic surfaces, the reduction of O_2 will produce OH^- creating an alkali environment. This is assumed by researchers to cause the coating to detach from the surface [39]. The increased current density demand is therefore ascribed as a result of the degree of disbondment of the coating observed, which will reduce the protection of the SDSS surface.

The average cathodic current measured for the different samples after being cathodically polarized for 157 days at $-1050 \text{ mV}_{\text{Ag}/\text{AgCl}}$ is as follows:

Polarized with intact coating : $i_{corr} = 16 \text{ mA/m}^2$

Polarized with damage : $i_{corr} = 19 \text{ mA/m}^2$

Polarized SDSS : $i_{corr} = 80 \text{ mA/m}^2$

Polarized NAB : $i_{corr} = 75 \text{ mA/m}^2$

Bubble formation was also observed on samples having a 2 cm^2 damage in the coating. No delamination of the coating was found around the edge of the damaged area, indicating that the cathodic disbonding occurs mainly from seawater diffusing through the coating. Increasing O_2 concentration and reduced electrode potential have shown to increase the degree of cathodic disbonding. This is related to the rate of cathodic reaction on the surface. Calcareous deposits were detected in the damaged area, which will reduce the cathodic current. This may be reason for the lack of cathodic disbonding at the edge of the coating. The cathodic current measured on the samples having damage in the coating is assumed to be a combination of cathodic current acting on the exposed SDSS area and the cathodic current arising when seawater diffuse through the coating. An average current density of 19 mA/m^2 appears to be a reasonable current density in regards to the area relation between the xylan surface and SDSS.

4.1.6 Other Concerns Regarding Use of SDSS and NAB in Seawater

The materials may be exposed to different corrosion mechanisms during a lifetime of 25 years exposed to seawater. The scope of this thesis includes only some corrosion scenarios that may arise in the SDSS power screw and NAB nut system. However, the components are exposed to some other mechanisms that will be briefly mentioned in this section.

Crevice corrosion can be a concern if the power screw and nut are in the same position over a longer period of time. Stagnant water may cause reduced pH of the stagnant seawater, resulting in localized corrosion attacks on both SDSS and NAB. Passive metals are sensitive against this corrosion form due to the passive layer acting as cathode creating an unfavorable cathode/anode area.

To ensure the 25 years lifetime of the materials, Al-anodes are mounted on the foil module. The design potential when using Al-anodes as cathodic protection is $-1050 \text{ mV}_{\text{Ag}/\text{AgCl}}$. According to DNVGL-RP-F112, SDSS is exposed to HISC when polarized to potentials lower than $-800 \text{ mV}_{\text{Ag}/\text{AgCl}}$, when all the criteria are fulfilled, see Section 1.4.6. The stress the materials may be subjected to is uncertain, but when the foils are in the extended position the stress may be

significant. The power screw may be subjected to HISC, especially at points **A**, **B** and **C** shown in Figure 1.8.

Using NAB is advantageous for parts exposed to higher flow velocity due to its high critical velocity before being sensitive to erosion. But Cu is vulnerable to sulfides that may be present in some areas due to pollution. Ships with these foils may in shorter period travel in polluted seawater containing sulfides. When pre-exposed to polluted seawater before un-polluted seawater, the corrosion rate will be high due to the presence of O_2 . However, this is assumed to only occur for a shorter period of time as a dense Cu_2O will be formed as Cu-ions is released when corroding.

During movement of the vessel, higher flow rate of seawater on the materials may affect them in different ways. Increased velocity will directly affect the limiting current density as a result of a higher supply of O_2 . The high flow rate will also affect the localized corrosion attacks on the material surfaces. Higher flow velocity has been found to lower the extent of corrosion attacks on the surface as the higher velocity will provide a higher probability of renewing seawater inside the pits. But has also shown to increase the probability of initiation of localized attacks on the surface.

4.2 Tribology Experiments

The main objective of the tribology part is to provide an overview of how the coating behaves in sliding contact in seawater when cathodically protected. During this thesis, different experiments have been performed by using a reciprocal tribometer with a point- and line contact in dry condition and when immersed in seawater at OCP and when cathodically polarized. In addition, some dry continuous pin-on-disk experiments were conducted.

4.2.1 Tribological Properties of Xylan in Dry Condition

As mentioned earlier, the load that the power screw and nut will be subjected to during operation is unknown, hence different loads were applied during dry reciprocal tribotest. Coating thickness will affect whether the maximum shear stress acts inside the coating or in the substrate. A coated sample was checked in a light microscope where the coating thickness was measured to be $90\ \mu\text{m}$. Calculations have been performed to find the Hertzian contact pressure and the depth of the maximum shear stress at different loads, see Table 2.3 for point contact and Table 2.4 for line contact. Table 3.5 provides the calculated depth of maximum shear stress.

Results obtained reveals that maximum contact pressure and depth of maximum shear stress depends on the type of substrate. Depth of the maximum shear stress is calculated to be inside the SDSS substrate, i.e. higher than 90 μm , for all the loads applied when assuming the sliding acts against xylan surface. Using SDSS as the substrate, all loads gave a depth of maximum shear stress acting inside the coating, i.e. lower than 90 μm . Except for when applying 77 N corresponding to 1.63 GPa where a depth of 90 μm was calculated. Maximum shear stress inside the substrate indicates that the coating will experience adhesive wear and being detached from the substrate. This is in line with the surface observed after applying 77 N. The coating was removed from the wear track during sliding and a total volume loss of 0.47 mm^3 was measured exposing the SDSS surface. While when applying 65 N, corresponding to 1.58 GPa a maximum depth of 80 μm was calculated. The thickness of the coating will vary over the sample surface due to surface roughness, but it is assumed that 80 μm will be inside the coating. The volume loss at this load was 0.069 mm^3 reflecting only the loss of xylan coating during sliding that was observed on the surface. This is in line with maximum shear stress acting inside the coating resulting in cohesive wear. The SDSS substrate has a thickness of approximately 2820 μm , while the coating thickness is measured to be 90 μm . When correlating the depth of maximum shear stress to the wear track observed, the coating appears to be a thin coating. Hence, the mechanical properties of the SDSS substrate such as the hardness and elastic modulus are then applied while the thin coating provides the low friction property.

COF measured for reciprocal and pin-on-disk tribotests are plotted in the same graph for easier comparison in Figure 4.2. Higher COF measured for reciprocal movement indicates that the start/stop motion produces higher friction compared to continuous movement. The higher COF for reciprocal movement is assumed to be a result of adhesive forces arising. Higher volume loss and wear rate were also measured. No clear tendency is seen between volume loss and wear rate for different loads. This is assumed to be caused by different wear mechanisms dominating the interface. At lower loads, adhesion is more likely to dominate the interaction, while at higher loads ploughing will dominate. Highest COF was measured for reciprocal tribotest when applying a load of 2 N, corresponding to 779 MPa against SDSS. A COF of 1.7 was measured compared to 0.12 for pin-on-disk tribotest. The high COF was first believed to occur as a result of the applied load being too low to smooth the surface. Hence, the friction was assumed to be affected to a larger extent by the asperity heights. The surface roughness of samples used for these tribotests was in addition measured, see Figure 2.5. Similar R_q was measured with 1.36 μm and 1.44 μm , for reciprocal and pin-on-disk tribotests, respectively. Based on similar R_q measured, high COF would also be expected for the pin-on-disk experiments if surface roughness affected the sliding. In addition higher volume loss was measured for reciprocal movement at this load. The high COF is therefore believed to be more likely a result of adhesive forces arising when changing the sliding direction.

The low friction of the PTFE based coatings is due to a transfer film being formed on the counter surface. A more pronounced wear track is observed after pin-on-disk compared to reciprocal tribotests when applying the same load. This correlates well with the higher weight percentage

Mo detected on the surfaces subjected to the continuous pin-on-disk wear test. While lower F was detected. Decreasing COF measured for reciprocal tribotest when increasing the load is in correlation with the easy shear property of the coating is activated. While results obtained for pin-on-disk tribotest is in contradiction to this. Where higher COF is measured for increasing loads. This may be a result of lower weight percentage F present. The lubricant properties of the different elements should be studied closer to obtain a better understanding.

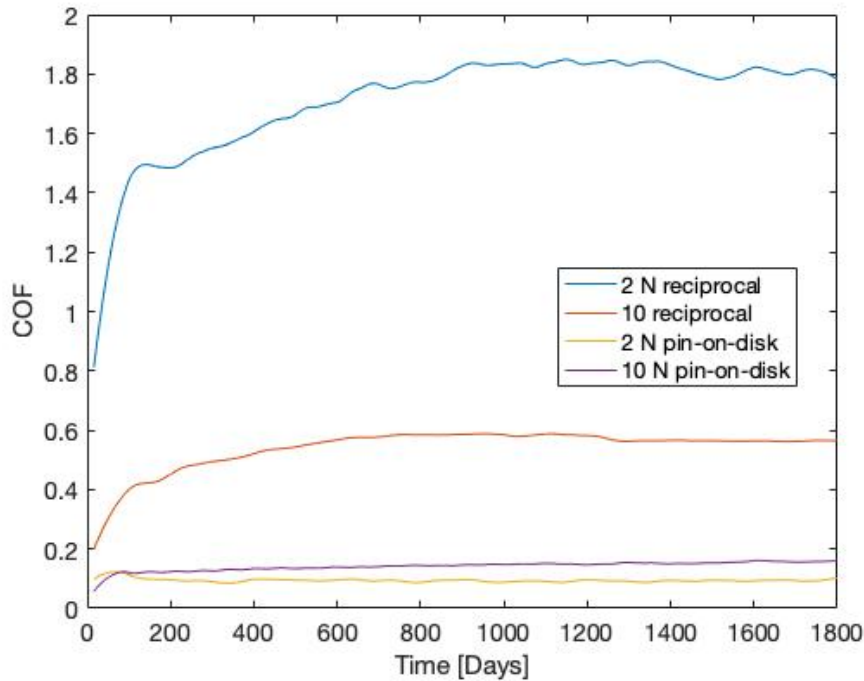


Figure 4.2: Comparison of dry COF measured when using reciprocal tribometer and continuous pin-on-disk tribometer for 2 N and 10 N at a speed of 0.01 m/s.

Based on these results it is assumed that the outer part of the power screw is more likely to experience higher friction and wear. This also implies that lower degradation of the materials can be expected in the middle part of the power screw where continuous movement occurs. The level of friction and wear that the SDSS and NAB threads will experience will also depend on the surface roughness obtained during machining of the threads.

4.2.2 Tribological Properties of Xylan and SDSS in Seawater at OCP

Tribocorrosion experiments were performed by sliding a NAB cylinder against a SDSS and xylan coated SDSS surface. 40 % difference in COF was measured when sliding NAB cylinder against xylan surface at OCP, hence the COF was not reproducible. This attributes to variation in surface roughness affecting the friction during sliding. The NAB cylinder creates a line contact

during sliding and will thus have a larger contact area being affected by the roughness compared to point contact.

A hydrodynamic layer can be formed during sliding between surfaces in the presence of liquids. The sliding surfaces are then separated reducing the COF. During the reciprocal movement, the start/stop motion is assumed to prevent the hydrodynamic layer from being formed. How COF depends on the sliding speed, viscosity, and applied load is given by the Stribeck curve, see Figure 1.11. Sliding of the NAB cylinder against the xylan coated surface at OCP promoted higher COF compared to when sliding the NAB cylinder against the SDSS surface with a COF of 0.25 and 0.23, respectively. The difference may be arbitrary due to the difference in surface roughness. The SDSS surface was ground with a P500 paper due to an uneven surface. This may contribute to the lower COF. Lower COF may also be a result of the lower hardness of xylan compared to SDSS, see Table 1.2. The real contact area will then be higher during sliding between NAB and xylan, and therefore promote higher resistance against the movement. To obtain more dependable results, the same surfaces should be used for the SDSS surface as used for the SDSS substrate under xylan coating.

A bathtub shaped potential curve was as expected obtained when sliding a NAB cylinder against SDSS and xylan coated SDSS at OCP. The effect of sliding on the potential of the materials is easily seen, see Figure 3.12. The reduced potential measured when sliding the NAB cylinder against the xylan coated SDSS is assumed to be a combination of the degradation of the passive layer on NAB and the wear of xylan coating reducing its protective ability. The lower potential was measured when sliding NAB against the SDSS surface. This is expected due to the degradation of the passive layer on NAB and SDSS transforming the wear track from passive to anodic on both surfaces.

4.2.3 Tribological Properties of Xylan and SDSS in Seawater at $-1050 \text{ mV}_{Ag/AgCl}$

Image of the SDSS surface after being subjected to sliding by a NAB cylinder when cathodically polarized is shown in Figure 4.3. Wear tracks are observed sporadically over the sample surface which is attributed to surface roughness creating areas being more affected by the sliding. Volume loss was difficult to obtain due to the sporadic wear track. Highest COF was measured for NAB against SDSS, with an average value of 0.42, while during OCP the COF measured was 0.23. EDS analysis of the SDSS surface showed no signs of Cu elements, implying that a transfer layer of the more ductile Cu, on the SDSS surface, had not been formed during sliding. Calcareous deposits elements were detected on the surface and are assumed to be the cause of the increased friction during sliding. This contradicts results published by Jin et al. (2016) where they obtained reduced COF, attributed to the present of CaCO_3 and $\text{Mg}(\text{OH})_2$ [50]. SEM images of the wear tracks on the NAB cylinder showed a more pronounced wear track after sliding against SDSS. After sliding against the xylan surface a more continuous wear track is observed, see Figure 3.16.

This is assumed to be a result of xylan having a lower hardness compared to SDSS. The larger contact area is then expected to create a more continuous wear track. This has been previously discussed in Section 4.2.2 in regards to the difference in COF measured at OCP.

EDS analysis of NAB cylinder after sliding against xylan surface detected only C on the surface, see Table 3.10. Thus a transfer layer is not formed to the same extent in seawater as in dry conditions. Seawater preventing adhesion of the transfer particles to the surface is believed to cause the absence of the transfer layer. Calcareous deposits are assumed not to be well formed on xylan surface, and only a weight percentage of Mg of 1.02 wt% was detected on the NAB cylinder compared to 7.52 wt% after sliding against SDSS surface. Similar COF was measured when cathodically polarized and at OCP when sliding the NAB cylinder against xylan coated SDSS. This is assumed to be caused by the absent of calcareous deposits detected on the xylan surface. The low amount of Mg measured is in accordance with the low surface energy of the xylan coating.



Figure 4.3: Wear track obtained on SDSS surface when cathodically protected after reciprocal sliding of a NAB cylinder for 1800 s at 0.01 m/s.

Dry reciprocal experiments between NAB cylinder and SDSS and xylan coated SDSS surface were not conducted. This should have been performed for easier comparison of the COF measured during dry tribotests and during tribocorrosion experiments. During dry reciprocal tribotest, a COF of 0.5 was measured between a 316 SS sphere and xylan surface. COF of 0.27 was measured between NAB cylinder against xylan surface in seawater when cathodically polarized. Higher COF is expected when using a cylinder due to the line contact, and a COF higher than 0.5 would be expected to be measured in dry condition. Despite the lack of formation of a transfer layer on the NAB surface in seawater, the COF is lower. This is attributed to the ability of seawater to hinder adhesion between asperities. This may also imply that the effect of seawater on the degree of friction during sliding is higher than the effect of a transfer layer in dry conditions.

This should be investigated closer if a better understanding is desired, though this was not in the scope of this thesis.

Higher current demand was measured during sliding to sustain the protecting potential. This is assumed to be caused by the passive layer being degraded or completely removed from the wear track and then being transformed to an anodic surface. A small anodic area is created inside the wear track, accompanied by cathodic reactions occurring on the larger passive area outside the wear track. The high cathode/anode area relationship will accelerate the corrosion reaction. During sliding movement between NAB and SDSS, both metals will acquire a certain current to be protected due to degraded passive layer. The current density was as such problematic to obtain due to the difficulty of knowing the area to use as a denominator in the calculations. For comparison, the current measured during long term corrosion experiments when cathodically polarized is given below. Current demand arising during sliding between NAB and SDSS was measured to be 10 mA, compared to 0.3 mA measured before sliding commenced. During tribotest between NAB and xylan coated SDSS an average current was measured to be 0.63 mA. This current is assumed to be a combination of the degradation of the passive layer on NAB and the protective ability of xylan coating being reduced as a result of the coating being continuously degraded.

Lower current was measured during sliding of the NAB cylinder against xylan coated SDSS having a damaged area compared to when sliding against intact xylan coated SDSS. These results imply that a larger degraded area must be present to markedly affect the current demand. Precipitation of calcareous deposits on the exposed SDSS is believed to be the reason for this. This emphasizes how the surface roughness also may affect the current demand. The surface of the NAB cylinder showed a more discontinuous wear track after sliding against the surface having damaged xylan coating. A negligible current was measured when having a damaged area inside the wear track. This is explained by a smaller part of the NAB cylinder being in contact with the surface during sliding. This was confirmed during the inspection of the NAB cylinders.

Average cathodic current demand measured during long term corrosion experiments for SDSS, NAB and xylan coated SDSS were as follows:

Polarized with intact coating : $I = 0.081mA$

Polarized with damage : $I = 0.094mA$

Polarized SDSS : $I = 0.49mA$

Polarized NAB : $I = 0.26mA$

4.2.4 Uncertainties During Experiments Performed

As a consequence of the impossibility to obtain NAB spheres, dry tribotests were performed by sliding 316 SS spheres against a xylan coated SDSS. It is assumed that in dry conditions, the tribological performance of xylan coating will be reflected in a similar way as if using NAB spheres. NAB cylinders were used for tribocorrosion experiments performed in seawater. This gave inconclusive results in regards to COF. This is believed to be caused by the surface roughness affecting the line contact more than point contact due to a larger area. More accurate results would be expected if using NAB spheres also for tribocorrosion testing. These results emphasize the difficulty of testing sliding contacts with larger contact area due to the interference of surface roughness.

The sliding speed is estimated by Wavefoil to be 3.4 m/s during the extension and retraction of the foils. Reciprocal tests were performed at 0.01 m/s while continuous pin-on-disk tests were performed at 0.01 m/s and 0.1 m/s. It is not possible to test with this kind of speed expected during operation in a tribometer, hence in regard to velocity, the experiments conducted are not conservative.

The contact load that the materials are exposed to is unknown therefore the COF and the extent of wear observed are only an indication of what can be expected if the contact load is between 2 N and 77 N. The Hertz contact pressure calculated for line contact and for point contact revealed that the maximum pressure that can be expected depends on the type of contact. Though based on observations made at the Tribology lab it is assumed that the xylan coating acts as a thin, this cause some uncertainty.

Tribotesting was performed by using sphere and cylinder sliding against a flat surface. In order to easier conclude with what to expect during operation of the power screw and nut, tests should have been performed by using a small-scale xylan coated SDSS power screw and a connecting NAB nut should have been tested.

4.3 Full-Scale Pilot Module

In spite of the uncertainties presented above in Section 4.2.4, a good correlation is found between results obtained during experiments performed and observations made on the full-scale module. When analyzing results obtained during experiments it is clear that the coating will partially or completely degrade due to cathodic disbonding. The xylan surfaces being cathodically protected for 110 days showed a notable amount of bubble formation which was easily removed from the surface. Sliding motion between the xylan coated SDSS power screw and NAB nut will occur during the extension and retraction of the foils. The sliding motion is expected to further

accelerate the removal of the coating. This may also increase the resistance against movement and cause increased wear due to wear particles from the coating being trapped between the sliding surfaces. Observations made of the components in the foil module after being operated for 43 days revealed that the xylan coating was partly degraded, see Figure 3.17. The degradation may be a combination of cathodic disbonding observed by long term corrosion experiments and mechanical degradation of the xylan coating observed after performing tribotests.

Based on the results presented in this thesis it is further believed that the sliding contact will consist of an uncoated SDSS power screw against NAB nut after some time. During sliding contact, non-compatible metals should be used to prevent adhesive forces from arising. As Cu and Fe are only partially compatible, the adhesive forces will be moderate. Sliding contact between NAB and SDSS will experience increased friction when cathodically protected due to calcareous deposits forming on the SDSS surface. Deposits are assumed to be removed during extension and retraction of the foils. While when the foils ate in the same position over a longer period calcareous deposits will re-precipitate on the surface.

High current demand was measured when sliding NAB against the SDSS surface when cathodically protected, and a current demand close to 10 mA can be expected during operation of the foils depending on the degree of coating degradation. However, this level of the current demand will only occur in a short period. Corrosion products were observed on the Sacrificial anodes mounted on the NAB nut. The current demand is assumed to decrease with time being cathodically polarized. The initial current demand measured for NAB was 300 mA/m^2 while after being polarized for 157 days the current demand was 75 mA/m^2 attributed to calcareous deposits. Higher current demand is therefore expected to go from the sacrificial anodes when first immersed in seawater. 186 anodes are assumed to be needed to obtain full protection for 25 years to protect the SDSS power screw and NAB nut. When assuming the coating will provide protection for some time a CBF of 0.84 was used. This gave a total amount of anodes of 160. The amount of anodes calculated is only a rough estimation as the coating is sensitive to cathodic disbonding and is assumed to detach faster during sliding. Higher current density demand, when exposed to flowing seawater, is taken into account. However, how much this will affect the current density with regards to increased limiting current density and degrading deposits is unknown. In addition, if fouling occurs on the NAB surface as a consequence of being cathodically protected, high corrosion rate can occur between the sediments as previously explained in Section 4.1.3.

Chapter 5

Conclusion

5.1 Conclusion Regarding Corrosion Findings

Long term corrosion experiments were performed at SeaLab NTNU. SDSS and NAB were submerged in fresh seawater from Trondheim harbour for 157 days, while xylan coated SDSS for 110 days. The main objective was to study how SDSS and NAB behave being immersed in seawater when cathodic protected. The SDSS power screw and NAB nut have an area difference of approximately 7 in the foil module, therefore the galvanic current arising when in electric contact was also of interest.

Based on results obtained during long term corrosion experiments, the following conclusions can be made:

- SDSS experience ennoblement when immersed in seawater. This is attributed to biofilm formation enhancing the cathodic efficiency of the surface. Ennoblement was also observed on the NAB surface, where the first ennoblement is assumed to be a result of biofilm formation.
- When cathodic polarized to $-1050 \text{ mV}_{\text{Ag}/\text{AgCl}}$ over time, a current demand of $80 \text{ mA}/\text{m}^2$ and $75 \text{ mA}/\text{m}^2$ was measured for SDSS and NAB, respectively. Calcareous deposits formed on the surface will provide corrosion protection by hinder O_2 reaching the SDSS and NAB

surface.

- Cathodically polarized NAB did not display any signs of fouling after being immersed in seawater for 110 days. This may though develop to be a problem at a later point.
- Galvanic coupling between SDSS and NAB creates a significant current going from NAB to be reduced on the SDSS surface when having an area difference of ≈ 3 . The corrosion rate was calculated to be 0.28 mm/year. More extensive localized corrosion attacks on NAB is expected in the foil module due to the cathode/anode area difference of ≈ 7 if not cathodic protected.

Properties of the xylan coating in seawater were unknown when the experiments were initiated. Thus the ability of the coating to protect SDSS when submerged was of special interest. Experiments were performed in natural seawater to obtain information about the protective ability of the coating. Samples with intact coating and with a 2 cm² damage was coupled to a Zn-anode holding an average potential of -1080 mV_{Ag/AgCl}.

The conclusions regarding xylan coated SDSS that can be made is as follows:

- The xylan coating has a certain porosity allowing seawater to reach the SDSS surface and will create an electrochemical potential. Intact xylan coating required an average current of 16 mA/m² to be polarized to -1080 mV_{Ag/AgCl}. Hence, the coated surface will also require current from the anodes.
- The xylan coating is sensitive to cathodic disbonding when cathodically polarized. Extensive bubble formation was observed on samples being coupled to the Zn-anode for 110 days.
- No delamination of the coating was observed around the edge of the coating, thus the main cathodic disbonding will occur as a result of seawater diffusing through the coating. Calcareous deposits formed on the exposed area is assumed to lower the cathodic reaction such that the surface vicinity is not alkali enough for cathodic disbonding to occur.
- Calculations performed gave a total current demand corresponding to a total amount of 186 anodes when using Coral A-5 Al-nodes to protect SDSS and NAB for 25 years. By using a CBF of 0.84 on the xylan coated power screw a the total amount of anodes needed for protection was estimated to be 160.

5.2 Conclusion Regarding Tribological Findings

Tribological experiments were conducted at the Tribology lab at NTNU. The dry tribological performance of the xylan coating has been tested. Tribocorrosion experiments were performed by sliding a NAB cylinder over SDSS and xylan coated SDSS at OCP and when cathodic polarized

to $-1050 \text{ mV}_{\text{Ag}/\text{AgCl}}$. The materials will be cathodic protected during the lifetime of 25 years. Thus the experiments performed when cathodically polarized are of special interest.

Based on results obtained during experiments performed the following conclusions about the general tribological performance of the materials can be made:

- The xylan coating appears to be a thin coating, where the contact will exhibit the hardness and elastic modulus of the substrate while the lubrication property of the thin coating will provide low friction.
- Based on the comparison between results from dry reciprocal tribotest and dry continuous pin-on-disk test, the outer part of the power screw will experience higher COF and also higher wear rate. This is assumed to be due to adhesive forces acting during the change in sliding direction. While the middle part of the power screw will experience lower friction and also wear rate.
- EDS of the spheres revealed that a more extensive transfer layer was formed after pin-on-disk tribotest. Also, a higher load applied, up to 10 N, appears to promote a more well-formed transfer layer. The transfer layer was not detected in the same extent on the cylinder, indicating that seawater prevents adhesion of transfer particles.
- Lower COF was measured during reciprocal tribotest in seawater when comparing COF measured in dry reciprocal tribotest. Seawater is assumed to hinder adhesion between the asperities, preventing the formation of junctions. NAB sliding against xylan coating in seawater when cathodic protected is expected to have a COF between 0.2 and 0.3 depending on the surface roughness.
- The low energy surface of xylan is assumed to prevent calcareous deposits being formed on its surface. The COF when cathodic protected will mainly be affected by deposits formed on the NAB surface. Friction during sliding between SDSS and NAB will be more affected by deposits as they will form on both surfaces. A COF of approximately 0.4 can be expected depending on the extent of deposits formed.
- It is assumed that the contact will consist of uncoated SDSS power screw sliding against the NAB nut after some time as a result of cathodic disbonding of the coating. The sliding contact is, in addition, assumed to accelerate the removal of the coating.
- During sliding, the combination of electrochemical and mechanical degradation will increase the current demand needed for protection. The current demand will be a combination of the current needed to protect SDSS and NAB. The current demand from sacrificial anodes is expected to increase in the period were the wear tracks are activated.

Chapter 6

Further Work

This chapter provides a list of experiments that the author believes would give valuable information to obtain a better insight in the expected degradation if further experiments are to be performed. The following experiments could be of interest:

- Crevice corrosion between xylan coated SDSS and NAB and also SDSS and NAB as the threads will create a crevice when foils are placed in the same position over longer period of time.
- For better tribological insight, a small-scale xylan coated SDSS power screw with connected NAB nut should be used.
- The tribological experiments should be performed with NAB sphere in dry condition and in seawater when cathodic protected to better compare the results and the tribological performance of the coating.
- To see the affect of being sensitive to cathodic disbonding in regards to wear and degradation of the coating during sliding, xylan samples should be cathodic polarized over time before exposed to sliding.
- How well a transfer layer reduces the friction compared to having seawater present to prevent adhesion.
- Other coatings should be investigated in order to find a better solution in regards to cathodic disbonding.

Bibliography

- [1] Wavefoil. <https://www.wavefoil.com/>. Online; accessed 30.01.2019.
- [2] E. McCafferty. *Thermodynamics of Corrosion: Pourbaix Diagrams*, pages 95–117. Springer New York, New York, NY, 2010. ISBN 978-1-4419-0455-3. doi: 10.1007/978-1-4419-0455-3_6. URL https://doi.org/10.1007/978-1-4419-0455-3_6.
- [3] I Richardson. Guide to nickel aluminium bronze for engineers. https://www.copper.org/applications/marine/nickel_al_bronze/pub-222-nickel-al-bronze-guide-engineers.pdf, 2016. Online; access: 08.03.2019.
- [4] E Bardal. *Corrosion and Protection*. Springer, 1st edition, 2003. Engineering Materials and Processes.
- [5] E Bardal. *Korrosjon og korrosjonsvern*. Tapir akademiske forlag, 2nd edition, 1994.
- [6] J. A Collins, Bucby. H, and Staab. G. *Mechanical Design of Machine Elements and Machines*. John Wiley Sons, Inc, 2010.
- [7] Anton van Beek. *Advanced Engineering Design: Lifetime Performance and Reliability*, volume -1. 01 2006. ISBN 9081040618.
- [8] Szucs. M, Krallics. G, and Lenard. J. G. The stribek curve in cold flat rolling. 10:99–107, 2017.
- [9] W. G Stachowiak and W. A Batchelor. *Engineering Tribology*. Butterworth-Heinemann, 1st edition, 1993.
- [10] Heanija Super-Metals. Duplex stainless steel (uns 32750). <https://super-metals.com/wp-content/uploads/2015/03/duplex-2507.pdf>. Online; accessed 08.03.19.
- [11] DuPont Fluoroproducts. Teflon® ptfe fluoropolymer resin. http://www.rjchase.com/ptfe_handbook.pdf. Online; accessed 28.03.2019.

-
- [12] DMH Dichtungs und Maschinenhandel GmbH. Dmh 600 ptfe virgin mechanical, physical and thermal properties. https://www.dmh.at/files/attachments/15259/432041_DB_DS_DMH_600_PTFE_rein.pdf. Online; accessed 28.03.2019.
- [13] eFunda. Aisi type 316. http://www.efunda.com/Materials/alloys/stainless_steels/show_stainless.cfm?ID=AISI_Type_316&prop=all&Page_Title=AISI%20Type%20316. Online; accessed 18.05.2019.
- [14] H. N Krogstad. *Corrosion of Ni-Al bronze in seawater-immersed permanent magnet motors*. PhD thesis, Norwegian University of Science and Technology, 2017.
- [15] Eirik Bøckmann, Audun Yrke, and Sverre Steen. Fuel savings for a general cargo ship employing retractable bow foils. *Applied Ocean Research*, 76:1 – 10, 2018. ISSN 0141-1187. doi: <https://doi.org/10.1016/j.apor.2018.03.015>. URL <http://www.sciencedirect.com/science/article/pii/S0141118717304091>.
- [16] Eirik Bjørge Haugan, Monika Næss, Cristian Torres, Roy Johnsen, and Mariano Iannuzzi. Effect of tungsten on the pitting and crevice corrosion resistance of type 25cr super duplex stainless steels. *CORROSION*, 73, 08 2016. doi: 10.5006/2185.
- [17] Chantal Compere and Nathalie Lebozec. Behaviour of stainless steel in natural seawater, 12 1997.
- [18] A Bergel, D Fèron, and A Mollica. Catalysis of oxygen reduction in pem fuel cell by seawater biofilm. *Electrochemistry Communications*, 7(9):900–904, 2005.
- [19] M. J Schofield and R. D Kane. Defining safe use limits for duplex stainless steels. In *Duplex stainless steels*, volume 1. 1991.
- [20] R. E Johansson and H. L Groth. Corrosion fatigue and fatigue data for duplex stainless steels. In *Duplex stainless steels*, volume 1. 1991.
- [21] Norwegian Technology Center. Norsok standard m-001: Materials selection. 2002.
- [22] R. J. K Wood. Erosion-corrosion interactions of copper and aluminium alloys. In D Fèron, editor, *Corrosion behaviour and protection of copper and aluminium alloys in seawater*, pages 19–24. Woodhead Publishing Limited and CRC press LLC, 2007.
- [23] A Schüssler and H. E Exner. The corrosion of nickel-aluminium bronzes in seawater-i. protective layer formation and the passivation mechanism. *Corrosion Science.*, 34(11): 1793–1802, 1993.
- [24] R Johnsen. Experience with the use of copper alloys in seawater on the norwegian continental shelf. In D Fèron, editor, *Corrosion behaviour and protection of copper and aluminum alloys in seawater*, pages 62–72. Woodhead Publishing Limited and CRC press LLC, 2007.

-
- [25] H. N Krogstad and R Johnsen. Corrosion properties of nickel-aluminium bronze in natural water, effect of galvanic corrosion coupling to uns s31603. *Corrosion Science.*, 34(11): 1793–1802, 2016.
- [26] R.S. Oakley, J.C. Galsworthy, G.S. Fox, and K.R. Stokes. 7 - long-term and accelerated corrosion testing methods for cast nickel–aluminium bronzes in seawater. In D. Féron, editor, *Corrosion Behaviour and Protection of Copper and Aluminium Alloys in Seawater*, European Federation of Corrosion (EFC) Series, pages 119 – 127. Woodhead Publishing, 2007. ISBN 978-1-84569-241-4. doi: <https://doi.org/10.1533/9781845693084.3.119>. URL <http://www.sciencedirect.com/science/article/pii/B9781845692414500071>.
- [27] J Birn and I Skalski. Corrosion behavoiur of non-ferrous alloys in seawater in the polish marine industry. In D Fèron, editor, *Corrosion behaviour and protection of copper and aluminium alloys in seawater*, pages 3–16. Woodhead Publishing Limited and CRC press LLC, 2007.
- [28] J. N Al-Hajji and M. R Reda. The corrosion of copper-nickel alloys in sulfide-polluted seawater: The effect of sulfide concentration. 34(1):163–177, 1993.
- [29] B. C Syrett. The mechanism of accelerated corrosion of copper-nickel alloys in sulphide-polluted seawater. *Corrosion Science.*, 21(3):187–209, 1981.
- [30] R Francis. Coupling of superduplex stainless steel and cast nickel–aluminium bronze in sea water. 34(2):139–144, 1999.
- [31] Det Norske veritas. Cathodic protection design. 2011. DNVGL-RP-B401.
- [32] O. Ø Knudsen and J. I Skar. *Cathodic disbonding of epoxy coatings - Effect of test parameters*. Number 08005. 1 2008. Corrosion 2008, Conference and Expo.
- [33] Morten Solnørdal, Stig Wästberg, Gustav Heiberg, and Odd Hauås-Eide. Hydrogen induced stress cracking (hisc) and dnv-rp-f112. *Measurement and Control*, 42:145–148, 06 2009. doi: 10.1177/002029400904200504.
- [34] Det Norske veritas. Duplex stainless steel - design against hydrogen induced stress cracking. 2018. DNVGL-RP-F112.
- [35] Roy Johnsen, Bård Nyhus, and Stig Wästberg. Hydrogen induced stress cracking (hisc) of stainless steels under cathodic protection in seawater: Presentation of a new test method. pages 55–67, 01 2009. doi: 10.1115/OMAE2009-79325.
- [36] F Abd El Aleem, I. S Al-Mutaz, and A Al-Arifi. *Corrosion and Scale Formation Problems in Water Systems*. 2011.
- [37] K Zakowski, M Szocinski, and M Narozny. *Study of the formation of calcareous deposits on cathodically protected steel in Baltic sea water*, volume Anti-Corrosion Methods and Materials. 3 2013. doi: 10.1108/00035591311308065.
-

-
- [38] T.R. Jack. Biological corrosion failures. *ASM Handbook*, 11:881–898, 01 2002.
- [39] J. F Watts. Mechanistic aspects of the cathodic delamination of organic coatings. *Journal of Adhesion*, 31:1:73–85, 1989. URL <https://doi.org/10.1080/00218468908048215>.
- [40] S. J Morrow. Materials selection for seawater pump. 2011. Turbomachinery Laboratory, Texas AM University.
- [41] R Francis. The erosion corrosion resistance of zeron 100, 2008. Engineering division.
- [42] Chengjie Li, Min Du, and Xin Cui. Influence of seawater flow velocity on the morphological characteristics of calcareous deposits formed by cathodic protection. 1 2015. doi: 10.2991/cmcs-15.2015.28.
- [43] A. I Muñoz and N Espallargas. Tribocorrosion mechanisms in sliding contacts. In *Tribocorrosion of passive metals and coatings*, volume 1, pages 118–152. 2011.
- [44] M Torbacke, ÅK Rudolphi, and E Kassfeldt. *Lubricants-Introduction to Properties and Performance*. John Wiley Sons, 1st edition, 2014.
- [45] Pradeep L. Menezes, Michael Nosonovsky, Satish V. Kailas, and Michael R. Lovell. *Friction and Wear*, pages 43–91. Springer New York, New York, NY, 2013. ISBN 978-1-4614-1945-7. doi: 10.1007/978-1-4614-1945-7_2. URL https://doi.org/10.1007/978-1-4614-1945-7_2.
- [46] K Kato. Friction and wear of passive metals and coatings. In D Landolt and S Mischler, editors, *Tribocorrosion of Passive Metals and Coatings*, chapter 3, pages 65–99. 10 2011. Nihon University, Japan.
- [47] H Butt, K Graf, and M Kappl. *Physics and Chemistry of Interfaces*, volume -1. 08 2004. ISBN 9783527404131. doi: 0.1002/3527602313.
- [48] F. P Bowden and D Tabor. The area of contact between stationary and between moving surfaces. 1939.
- [49] Alper Tasdemirci and M Kemal. On elastic contact stresses in a thin hard coating/an elastic substrate system. 06 2019.
- [50] Kongjie Jin, Zhuhui Qiao, Shuai Wang, Shengyu Zhu, Jun Cheng, Jun Yang, and Weimin Liu. The effects of main components of seawater on the tribological properties of cu-9al-5ni-4fe-mn alloy sliding against aisi 52100 steel. *RSC Adv.*, 6, 01 2016. doi: 10.1039/C5RA19719H.
- [51] Virginio Quaglioni and Paolo Dubini. Friction of polymers sliding on smooth surfaces. *Advances in Tribology*, 2011, 10 2011. doi: 10.1155/2011/178943.
- [52] Nikolai Myshkin and Alexander Kovalev. Adhesion and friction of polymers. *Polymer Tribology*, 03 2009. doi: 10.1142/9781848162044.0001.

-
- [53] O Ajayi and K.C. Ludema. Mechanisms of transfer film formation during repeat pass sliding of ceramic materials. *Wear*, 140:191–206, 11 1990. doi: 10.1016/0043-1648(90)90083-M.
- [54] M. H. Cho. The role of transfer film and back transfer behavior on the tribological performance of polyoxymethylene in sliding. *Journal of Mechanical Science and Technology*, 2009.
- [55] Shibo Wang, Li Pan, and Qian Li. Tribological behaviors of polytetrafluoroethylene composites under dry sliding and seawater lubrication. *Journal of Applied Polymer Science*, 130(4):2523–2531, 2013. doi: 10.1002/app.39454. URL <https://onlinelibrary.wiley.com/doi/abs/10.1002/app.39454>.
- [56] Yunxia Wang and Fengyuan Yan. Tribological properties of transfer films of ptfe-based composites. *Wear*, 261:1359–1366, 12 2006. doi: 10.1016/j.wear.2006.03.050.
- [57] R Johnson and C.B. Von Der Ohe. Tribocorrosion in marine environments. *Tribocorrosion of Passive Metals and Coatings*, pages 441–474, 10 2011. doi: 10.1016/B978-1-84569-966-6.50016-6.
- [58] B. B Zhang, J. Z Wand, J. Y Yuan, and F. Y Yan. Tribocorrosion behavior of nickel aluminum bronze in seawater: Identification of corrosion-wear components and effect of ph. 69:106–114, 2017. *Materials and Corrosion*.

Appendices

Appendix A

Calculations to Obtain Number of Sacrificial Anodes Required

Calculations of Average Anode Mass Needed for Cathodic Protection.

Amount of sacrificial anodes needed to protect the power screw and nut was calculated by following the recommended practice for cathodic protection design created by DNV, DNV-RP-B401 [31]. Current density used for these calculations are a conservative value based on values measured during long term experiments. 200 mA/m^2 is used for SDSS and NAB in order to have a conservative approach in regards to flowing seawater affecting limiting current density and also the presence of calcareous deposits.

According to DNV-RP-B401 in case of large structures of uncoated metal, the initial and final current density demand must be calculated in addition to the middle current density. Calculations were performed by using initial and final current density and gave an insignificant amount of anodes needed to obtain protection. Hence, calculations in this thesis will be based on the mean current demand and the amount of sacrificial anodes calculated will be based on this current to be protected throughout the lifetime of 25 years. The current densities used are given in Table

A1.

Table A1: Current densities used during design.

Parameters measured	SDSS	NAB
Initial current demand	350 mA/m ²	300 mA/m ²
Final current demand	90 mA/m ²	70 mA/m ²
Mean current density	200 mA/m ²	200 mA/m ²

Area of the materials to be protected are given by Wavefoil, see Table A2.

Table A2: Area to be protected in m²

Area to be protected	
SDSS	3.5m ²
NAB	0.46m ²
Xylan coated SDSS	3.5m ²

Al-anodes, Coral A-5 from Skarpenord with a rectangular shape are installed to protect the SDSS power screw and NAB nut against corrosion. Specifications provided by the supplier are given in Table A3.

Table A3: Parameters obtained from the supplier, Skarpenord.

Parameters from the supplier	
Dimensions	L=140 mm, W=70 mm, H=20 mm
Capacity	2585 Ah/kg
Closed circuit potential	-1090 mV _{Ag/AgCl}

Other relevant information obtained from DNV-RP-B401 and ISO 15589-2 are shown in Table A4.

Table A4: Other parameters obtained from DNV-RP-B401 and ISO 15589-2

Parameters	
Seawater resistance	0.2 ohm at 3.5 % NaCl and T= 10 °C
Protecting potential NAB	-800 mV _{Ag/AgCl}
Protecting potential SDSS	-500 mV _{Ag/AgCl}

Anodes Needed to Protect NAB Nut

Equation A.1 gives the current needed to protect NAB when both area and current density are known.

$$\begin{aligned}
 I_c &= A_c * i_c \\
 I_{c_{mean}} &= A_c * i_c \\
 &= 0.46m^2 * 0.2A/m^2 \\
 &= 0.092A
 \end{aligned}
 \tag{A.1}$$

I_c gives the cathodic current needed to sustain the potential for NAB at -1050 mV_{Ag/AgCl} by using the cathodic area A_c and conservative current density, i_c . Due to high flow rate of seawater during movement of the vessel, higher cathodic current is expected. As a more conservative choice, the mean current density is calculated by using 200 mA/m² for SDSS and NAB.

Anode mass needed for protection during a lifetime of 25 years is obtained from Equation A.2 by using the mean current demand calculated in Equation ?? when assuming a current density of 200 mA/m².

$$M_a = \frac{I_c t_f * 8769}{u \epsilon} \tag{A.2}$$

where t_f is the lifetime in years, u is the anode utility factor, and ϵ is the anode capacity in Ah/kg.

$$\begin{aligned}
 M_a &= \frac{0.092A * 25years * 8769}{0.9 * 2595Ah/kg} \\
 &= 8.7kg
 \end{aligned}
 \tag{A.3}$$

8.7 kg anode mass is needed for protection throughout 25 year lifetime when assuming a current demand of 200 mA/m² due to higher flow rate. According to the supplier the net mass of each anode is measured to be 0.4 kg. Hence the total amount of anodes needed is 22.

Anodes Needed to Protect SDSS Power Screw

The same procedure is done when calculating amount of anodes needed to protect SDSS as for NAB above. SDSS has an area of $\approx 3.5 \text{ m}^2$. Due to high flow rate of seawater during movement of the vessel, a more conservative current demand of 200 mA/m^2 has been chosen throughout the lifetime.

$$\begin{aligned} I_{c_{mean}} &= A_c * i_c \\ &= 3.5 \text{ m}^2 * 0.2 \text{ A/m}^2 \\ &= 0.7 \text{ A} \end{aligned} \tag{A.4}$$

Anode mass needed for protection during a lifetime of 25 years is obtained from Equation A.5 by using the mean current demand calculated in Equation A.4 when assuming a current density of 200 mA/m^2 .

$$M_a = \frac{I_c t_f * 8769}{u \epsilon} \tag{A.5}$$

where t_f is the lifetime in years, u is the anode utility factor, and ϵ is the anode capacity in Ah/kg. The mean current calculated is used to find the anode mass.

$$\begin{aligned} M_a &= \frac{0.7 \text{ A} * 25 \text{ years} * 8769}{0.9 * 2595 \text{ Ah/kg}} \\ &= 65.7 \text{ kg} \end{aligned} \tag{A.6}$$

65.7 kg anode mass is needed for protection throughout 25 year lifetime when assuming a current demand of 200 mA/m^2 due to higher flow rate. By using anodes with a net mass of 0.4 kg, the total amount anodes needed for protection are 164.

Anodes Needed to Protect Xylan Coated SDSS Power Screw

Coating breakdown factor is used to approximate the current density needed to protect the coated materials in regards to its isolation performance. The mean coating breakdown factor is found by using Equation A.7. The xylan coating is assumed to be a Category I coating with one layer epoxy paint a nominal dry film thickness (DFT) of 20 μm . This gives parameters $a=0.1$ and $b=0.1$. The power screw and nut is designed to have a lifetime of 25 years.

$$\begin{aligned}f_{cm} &= a + b * \frac{t_f}{2} \\ &= 0.1 + 0.1 * \frac{25 \text{ years}}{2} \\ &= 1.35\end{aligned}\tag{A.7}$$

When the coating factor exceeds 1, a breakdown factor of 1 should be used further. This shows that the coating will be degraded from the SDSS surface within the 25 years lifetime. If the CP system is designed to have a longer lifetime than the calculated lifetime of the coating, Equation A.8 can be used.

$$\begin{aligned}f_{cm} &= 1 - \frac{(1 - a)^2}{2b * t_f} \\ &= 1 - \frac{(1 - 0.1)^2}{2 * 0.1 * 25 \text{ years}} \\ &= 0.84\end{aligned}\tag{A.8}$$

The average current is then calculated from Equation A.9.

$$\begin{aligned}I_c &= A_c * i_c * f_c \\ &= 3.5 \text{ m}^2 * 0.2 \text{ mA/m}^2 * 0.84 \\ &= 0.59 \text{ A}\end{aligned}\tag{A.9}$$

The amount of anodes needed is then calculated by using Equation A.10.

$$\begin{aligned}M_a &= \frac{I_{ctf} * 8769}{u\epsilon} \\M_a &= \frac{0.59A * 25years * 8769}{0.9 * 2595Ah/kg} \\&= 55kg\end{aligned}\tag{A.10}$$

55 kg anode mass is needed when assuming a coating breakdown factor of 0.84. The amount of anodes needed then corresponds to 138.

Appendix B

Hertzian Contact Pressure

Calculations

Calculations of the depth of maximum shear stress for point and line contact.

Table B1: Material properties for materials creating the contacts of interest.

Material	E-modulus	Poisson ratio
SDSS	200 GPa	0.3
NAB	125 GPa	0.32
PTFE	0.54 GPa	0.42
316 SS	193 GPa	0.3

Point contact Between a 316 SS Sphere and Xylan Coated SDSS Surface

During point load tests, 316 SS was tested against xylan coated SDSS during dry sliding. When considering elastic contact, reduced radius of curvature (R') and reduced elastic modulus (E')

$$\begin{aligned}
P_{max} &= \frac{3W}{2\pi * a^2} & &= \frac{3 * 10N}{2\pi * 0.33mm^2} \\
&= \frac{3 * 2N}{2\pi * 0.19mm^2} & &= 43.8MPa \\
&= 26.5MPa
\end{aligned} \tag{B.4}$$

Maximum shear stress and the depth of maximum shear stress is found by using Equation B.5 and Equation B.6.

$$\begin{aligned}
\tau &= 0.33P_{max} & &\tau = 0.33P_{max} \\
&= 0.33 * 26.5MPa & &= 0.33 * 43.8MPa \\
&= 8.7MPa & &= 14.5MPa
\end{aligned} \tag{B.5}$$

$$\begin{aligned}
z &= 0.63a & &z = 0.63a \\
&= 0.63 * 0.19mm & &= 0.63 * 0.33mm \\
&= 0.12mm & &= 0.208mm \\
&= 120\mu m & &= 208\mu m
\end{aligned} \tag{B.6}$$

Point Contact Between a 316 SS Sphere and SDSS Surface

Depth of maximum shear stress between 316 SS sphere and SDSS is found by using the same approach as above. Reduced radius of curvature (R') and reduced elastic modulus (E') are calculated by using equations given in Equation B.7 and in Equation B.8, respectively.

$$\begin{aligned}
\frac{1}{R'} &= \frac{1}{R_x} + \frac{1}{R_y} \\
\frac{1}{R'} &= \frac{2}{R_a} \\
\frac{1}{R'} &= \frac{2}{3mm} \\
R' &= 1.5mm
\end{aligned}
\qquad
\begin{aligned}
\frac{1}{E'} &= \frac{1 - 0.3^2}{2} \frac{1}{193GPa} + \frac{1 - 0.3}{200GPa} \\
\frac{1}{E'} &= 0.0046GPa \\
E' &= 215GPa
\end{aligned}
\tag{B.7}$$

$$\begin{aligned}
\frac{1}{E'} &= \frac{1 - 0.3^2}{2} \frac{1}{193GPa} + \frac{1 - 0.3}{200GPa} \\
\frac{1}{E'} &= 0.0046GPa \\
E' &= 215GPa
\end{aligned}
\tag{B.8}$$

The elastic semi contact area when applying 2 N and 10 N is found in Equation B.9.

$$\begin{aligned}
a &= \left(\frac{3WR'}{E'} \right)^{\frac{1}{3}} \\
&= \left(\frac{3 * 2N * 0.0015m}{215GPa} \right)^{\frac{1}{3}} \\
&= 0.035mm
\end{aligned}
\qquad
\begin{aligned}
&= \left(\frac{3 * 10N * 0.0015m}{215GPa} \right)^{\frac{1}{3}} \\
&= 0.059mm
\end{aligned}
\tag{B.9}$$

The maximum pressure is then found by using Equation B.10 for 2 N and 10 N.

$$\begin{aligned}
P_{max} &= \frac{3W}{2\pi * a^2} \\
&= \frac{3 * 2N}{2\pi * 0.035mm^2} \\
&= 779MPa
\end{aligned}
\qquad
\begin{aligned}
&= \frac{3 * 10N}{2\pi * 0.059mm^2} \\
&= 1371MPa
\end{aligned}
\tag{B.10}$$

Maximum shear stress is found by using Equation B.11 and the depth of maximum shear stress by using Equation B.12 when applying 2 N and 10 N.

$$\begin{aligned}
 \tau &= 0.33P_{max} & & = 0.33 * 1371MPa \\
 &= 0.33 * 779MPa & & = 452MPa \\
 &= 257MPa & &
 \end{aligned} \tag{B.11}$$

$$\begin{aligned}
 z &= 0.63a & & = 0.63 * 0.059mm \\
 &= 0.63 * 0.035mm & & = 0.037mm \\
 &= 0.022mm & & = 37\mu m \\
 &= 22\mu m & &
 \end{aligned} \tag{B.12}$$

Same calculations were performed for 65 N and 77 N following same approach as shown above. For 316 SS against xylan the maximum contact pressure was calculated to be 52 MPa and 56 MPa for 65 N and 77 N, respectively. This gave a depth of maximum shear stress of 490 μ m and 510 μ m. For 316 SS against SDSS, maximum contact pressure was 1.58 GPa and 1.63 GPa for 65 N and 77 N, respectively. The depth of maximum shear stress was then calculated to be 80 μ m and 90 μ m.

Line Contact Between a NAB Cylinder and Xylan Coated SDSS Surface

Same equations for finding reduced radius of curvature and reduced elastic modulus is used for line contact as for point contact, see calculations above. Radius of curvature of the sample is infinite as it is a flat surface, while for cylinder the radius is 4 mm. Reduced R (R') and reduced E (E') are found by using Equation B.13 and Equation B.14, respectively.

$$\begin{aligned}\frac{1}{R'} &= \frac{1}{4mm} + \frac{1}{\infty} \\ \frac{1}{R'} &= \frac{1}{4mm} \\ R' &= 4mm\end{aligned}\tag{B.13}$$

$$\begin{aligned}\frac{1}{E'} &= \frac{1}{2} \left[\frac{1 - 0.32^2}{125GPa} + \frac{1 - 0.42^2}{0.54GPa} \right] \\ E' &= 1.3GPa\end{aligned}\tag{B.14}$$

Half width of the contact rectangle is used to calculate the elastic contact area for line contact performed by using Equation B.15.

$$\begin{aligned}b &= \left(\frac{4WR'}{\pi l E'} \right)^{\frac{1}{2}} \\ &= \left(\frac{4 * 10N * 0.004m}{\pi * 0.0075m * 1.3GPa} \right)^{\frac{1}{2}} \\ &= 0.072mm\end{aligned}\tag{B.15}$$

Where i is the half contact length of the contact area. Then the elastic contact area is used to find the maximum contact stress by using Equation B.16.

$$\begin{aligned}P_{max} &= \frac{W}{\pi bl} \\ &= \frac{10N}{2\pi * 0.072mm * 7.5mm} \\ &= 5.89MPa\end{aligned}\tag{B.16}$$

Maximum shear stress is found by using Equation B.17 along with the depth, z , of maximum shear stress.

$$\begin{aligned}
 \tau_{max} &= 0.3 * P_{max} & z &= 0.78 * b \\
 &= 0.3 * 5.89MPa & &= 0.78 * 0.072mm \\
 &= 1.8MPa & &= 0.056mm \\
 & & &= 56\mu m
 \end{aligned} \tag{B.17}$$

Line Contact Between a NAB cylinder and SDSS Surface

Same equations for finding reduced radius of curvature and reduced elastic modulus is used for line contact as for point contact, see calculations above. Reduced R (R') and reduced E (E') are found by using Equation B.18 and Equation B, respectively.

$$\begin{aligned}
 \frac{1}{R'} &= \frac{1}{4mm} + \frac{1}{\infty} \\
 \frac{1}{R'} &= \frac{1}{4mm} \\
 R' &= 4mm
 \end{aligned} \tag{B.18}$$

$$\begin{aligned}
 \frac{1}{E'} &= \frac{1}{2} \left[\frac{1 - 0.32^2}{125GPa} + \frac{1 - 0.3^2}{200GPa} \right] \\
 E' &= 170GPa
 \end{aligned} \tag{B.19}$$

Half width of the contact rectangle is used to calculate the elastic contact area for line contact performed by using Equation B.20.

$$\begin{aligned}
b &= \left(\frac{4WR'}{\pi i E'} \right)^{\frac{1}{2}} \\
&= \left(\frac{4 * 10N * 0.004m}{\pi * 0.0075m * 170GPa} \right)^{\frac{1}{2}} \\
&= 0.0063mm
\end{aligned} \tag{B.20}$$

Where i is the half contact length of the contact area. Then the elastic contact area is used to find the maximum contact stress by using Equation B.21.

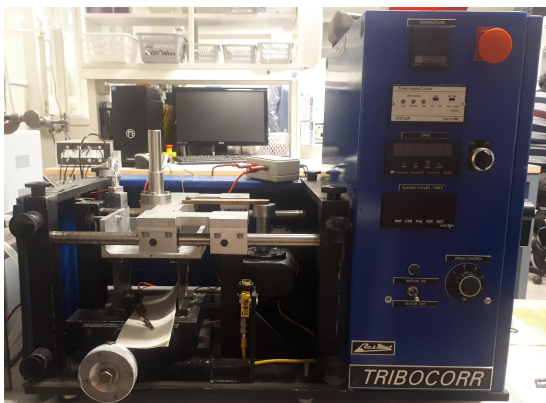
$$\begin{aligned}
P_{max} &= \frac{W}{\pi b l} \\
&= \frac{10N}{2\pi * 0.0063mm * 7.5mm} \\
&= 33.7MPa
\end{aligned} \tag{B.21}$$

The maximum shear stress is found by using Equation B.22 along with the depth, z , of maximum shear stress.

$$\begin{aligned}
\tau_{max} &= 0.3 * P_{max} & z &= 0.78 * b \\
&= 0.3 * 33.7MPa & &= 0.78 * 0.0063mm \\
&= 10.1MPa & &= 0.0049mm \\
& & &= 4.9\mu m
\end{aligned} \tag{B.22}$$

Appendix C

Photographs of the Experimental set-up



(a) ResMat tribometer used for dry reciprocal tribotests performed at different loads.



(b) Pin-on-disk tribometer used for dry continuous tribotests at different loads and speed.

Figure C1: Photographs of the tribometers used at Tribology lab at NTNU.

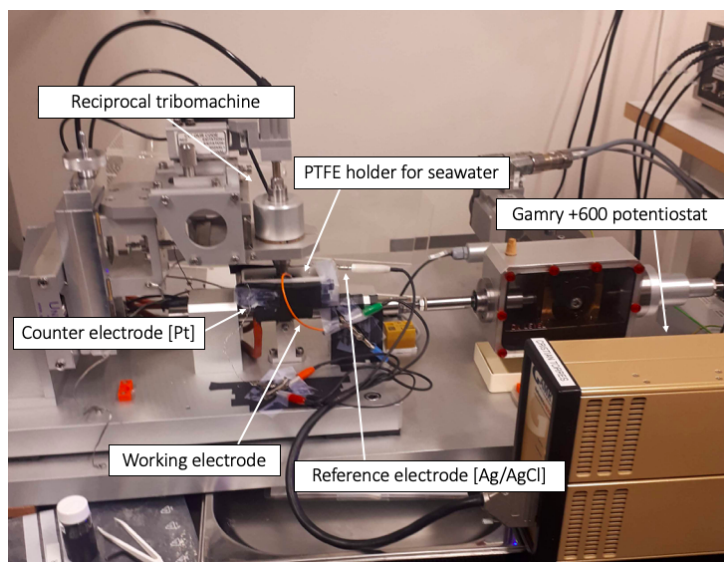


Figure C2: TE-38 tribometer used for tribocorrosion experiments performed at OCP and when cathodically polarized.

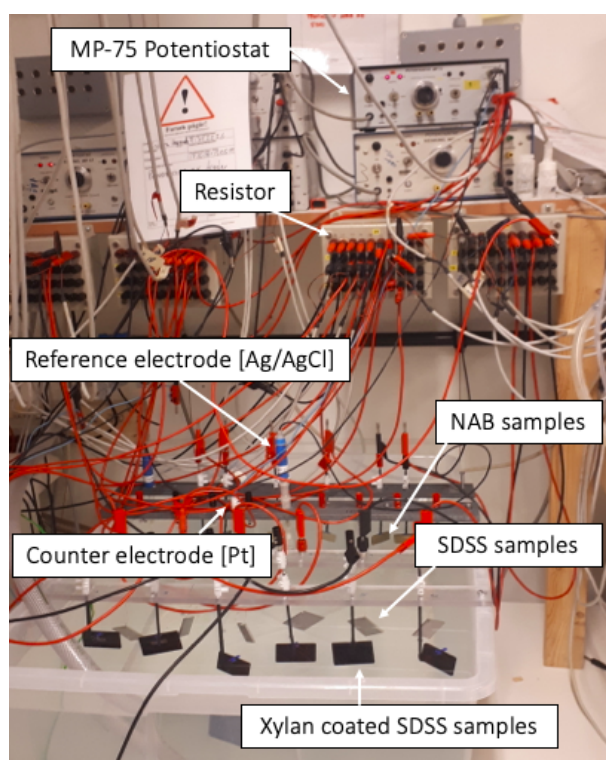
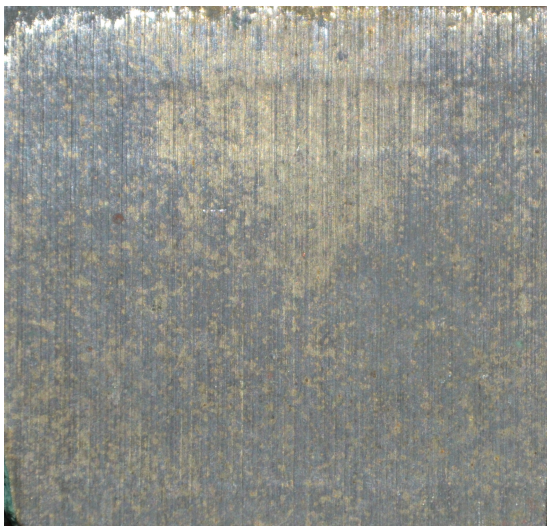


Figure C3: Photograph of the experimental set-up during long term experiments performed at SeaLab.

Appendix D

Photographs of the Material Surfaces

After Corrosion Experiments



(a) NAB surface after freely exposed in seawater for 157 days.

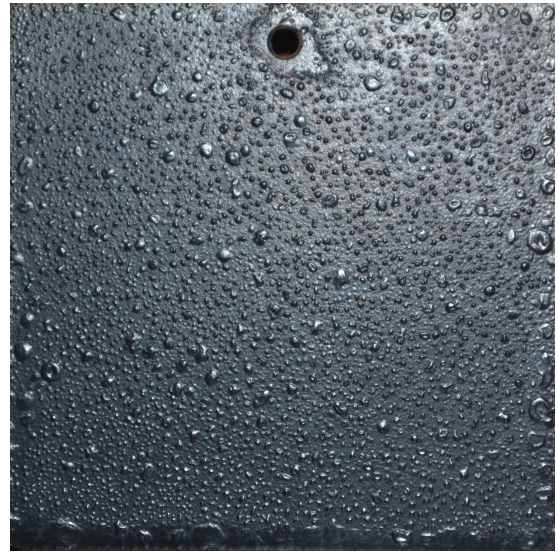


(b) NAB surface after cathodic polarized to $-1050 \text{ mV}_{\text{Ag}/\text{AgCl}}$ for 157 days.

Figure D1: Photographs showing NAB surfaces after corrosion experiments performed for 157 days at SeaLab.

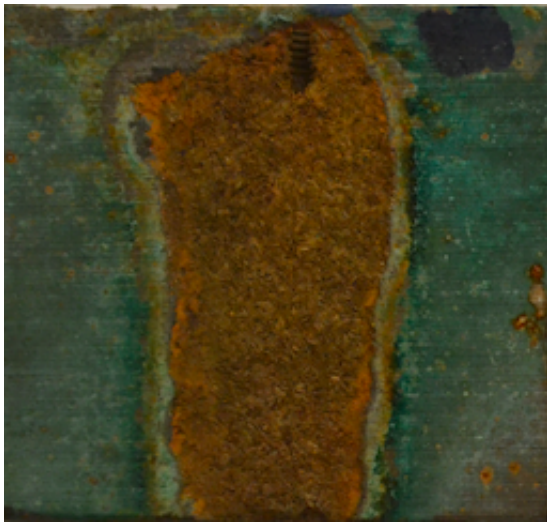


(a) Xylan surface after cathodic polarized by being coupled to a Zn-anode for 110 days.

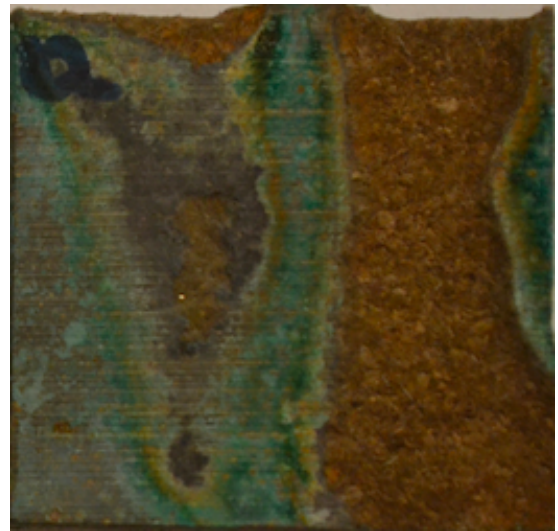


(b) Xylan surface with a 2 cm^2 damage after cathodic polarized by being coupled to a Zn-anode for 110 days.

Figure D2: Photographs of the xylan coated SDSS surfaces after long term corrosion experiment.



(a) Surface of NAB after being in electrical contact with SDSS for 157 days in seawater.



(b) Surface of NAB after being in electrical contact with SDSS for 157 days in seawater.

Figure D3: Photographs of the surfaces after long term corrosion experiment in electrical contact with SDSS with a SDSS/NAB area difference of ≈ 3 .

Appendix E

Datasheet for Xylan 1052



PRODUCT DATA SHEET

XYLAN® 1052/F1900 BLACK

1. GENERAL INFORMATION

Product description	Organic solvent based, high temperature, coating formulated for high-pressure, low-speed wear applications where long-term lubrication is required under extreme pressures i.e. up to 150,000 psi (10,500 kg/cm ²).
Specific end use(s)	High pressure, low speed. wear applications.
Supplier/Manufacturer	Whitford Ltd., 11 Stuart Road, Manor Park, Runcorn, Cheshire WA7 1TH England

2. PRODUCT SPECIFICATIONS

Solids, theoretical:	30.72 ± 1.5	% by weight	19.02 ± 1.0	% by volume
Relative density:	1.15 ± 0.02	g/l	9.63 ± 0.17	lbs/US Gal
Coverage, theoretical:	6.59	m²/kg @ 25 microns	7.81	m²/lit @ 25 microns
	70.93	ft²/kg @ 1 mil	309.97	ft²/US gal @ 1 mil
Viscosity:	45 - 50 seconds in a BS 4 viscosity cup at 23°C.			
Operating temperature:	-195°C - +280°C Continuous -195°C - +285°C Intermittent			
Flash point	Closed cup: 35°C			
VOC content:	798	g/l	799	g/l (less water)
	6.66	lbs/US Gal	6.67	lbs/US Gal (less water)

3. SUBSTRATE PREPARATION

Final product quality and performance depends on careful substrate preparation. Contaminated substrates may cause poor adhesion or defects in the final dry film. Each item to be coated must be free of all contaminants e.g. oil, grease, detergent, rust and blast media. Substrate preparation should be based on the design requirements of the item. If you are unsure which process is best suited to your needs please contact a Whitford representative for advice. The following are the recommended substrates and substrate preparation used with this coating:

Substrates:	Most common metals.
Substrate preparation:	Degrease. Light grit blast. An Ra (mean roughness) of 1.5 - 3.5 microns, measured using surface roughness measuring equipment is recommended. Typically use 80 - 100 mesh (150 - 200 micron) iron free, aluminum oxide grit. Since the Ra value achieved depends on the actual substrate, initial trials are recommended to establish the optimum grit size and air pressure for each substrate type. A heavyweight zinc phosphate, is recommended on mild steel.
Optional primer:	None required, but to improve overall performance may be used with Xylar 1, Xylar 2, Xylan 4090.

4. PREPARATION OF COATING MATERIAL

Mixing prior to use:	It is imperative that the material is adequately mixed before use. The material should be high speed / shear mixed before use to eliminate any settling. Avoid creating foam while mixing. Check that there is no sediment on the bottom of the container.
Recommended application viscosity:	The viscosity of this material will rise slowly over time but it can normally be applied in a viscosity range of 45 - 70 seconds in a BS 4 viscosity cup at 23°C.

4. PREPARATION OF COATING MATERIAL

Viscosity adjustment:	This material is generally suitable for application as supplied. Addition of any solvent will effect the specifications of the product. If absolutely necessary adjust viscosity with Whitford Solvent 91. Add thinner in 2% increments, while mixing, until the desired application characteristics are obtained. Take care not to add too much thinner as low viscosity may produce rapid settling, runs and sags or low film thicknesses.
Other information	This material is sieved before dispatch from our factory but as an added precaution we recommend that you filter it through a 150 mesh (100 micron) sieve prior to use.

5. RECOMMENDED APPLICATION TECHNIQUE

Application information/ technique:	This product is designed primarily for spray application. Consult with a Whitford representative if other types of application are being considered. Use a spray gun with a siphon cup or pressure pot. Select a fluid nozzle and air cap that meet application needs. Whitford UK uses a DeVilbiss GTI HD spray gun with a Pro 200-14 fluid nozzle and a GTI Pro T1 air cap. The air supply line should be equipped with traps to remove water and oil. Drain and service these traps frequently.
Recommended Dry Film Thickness/coat:	15 ± 5 microns. 0.6 ± 0.2 mil.
Substrate temperature:	<45°C
Number of coats recommended:	Typically 1 but it is possible to apply multiple coats. Flash off between coats if applying multiple coats.
Clean-up solvent:	Whitford Solvent 91.

6. FLASH OFF AND CURE SCHEDULE

Please note that oven temperatures can be very different to substrate temperatures and the following cure conditions apply to PEAK SUBSTRATE TEMPERATURE.

Flash-off conditions:	Dry at 50 - 100°C (120 -212°F) if not applied to a warm substrate.
Optimum cure schedule:	20 mins. @ 240°C (465°F)
Minimum cure schedule:	20 mins. @ 220°C (430°F)
Maximum cure schedule:	5 - 10 mins. @ 345°C (650°F)

7. TYPICAL CURED FILM PROPERTIES

Evaluate the coating according to the following specifications:

Dry film thickness (Whitford TM114A):	>15 microns. >0.6 mil.
Cure Test (Whitford TM115B):	No white precipitate or stain.
Appearance (Whitford TM120A):	
Gloss - 60° meter (Whitford TM121A):	Semi-gloss / satin finish.
Adhesion - Knife (Whitford TM132A):	No adhesion loss.
Adhesion - Crosshatch & Tape (Whitford TM132C):	No adhesion loss.

XYLAN® 1062/F1900 BLACK

8. SHELF LIFE, STORAGE AND HANDLING

Shelf life: 12 months

Storage: Store between the following temperatures: 5 - 35°C. Turn container(s) upside down or high speed / shear mix the material(s) every month to maintain quality and minimize settling. Containers that have been opened must be carefully resealed and kept upright to prevent leakage.

Avoid breathing vapours, spray or mists. Wash hands before eating, drinking or smoking. Wear appropriate personal protective equipment. Avoid direct contact with the human body. See SDS for more information.

Prepared by lbentley@whitfordww.com

NON-WARRANTY: The information presented in this publication is based upon the research and experience of Whitford. No representation or warranty is made, however, concerning the accuracy or completeness of the information presented in this publication. Whitford makes no warranty or representation of any kind, express or implied, including without limitation any warranty of merchantability or fitness for any particular purpose, and no warranty or representation shall be implied by law or otherwise. Any products sold by Whitford are not warranted as suitable for any particular purpose to the buyer. The suitability of any products for any purpose particular to the buyer is for the buyer to determine. Whitford assumes no responsibility for the selection of products suitable to the particular purposes of any particular buyer. Whitford shall in no event be liable for any special, incidental, or consequential damages.

Appendix F

Datasheet for SDSS

Business Unit / QCM
Avesta Works / Johan Nordström

Date / Datum / Date
10-Mar-2017

Lot / Ladung / Charge No
NO/148472

Acknowledged ID / Bestätigung / Commande ID
6610/300392951

Your ref. / Ihre Ref. / Votre ref. 821163 Ove Mæhle.	Requirements, Anforderungen, Exigences ASTM A 240M-16a ASME BPVC SEC II PART A SA-240/SA-240M 2015 EN 10088-2:2014 EN 10028-7:2016 NACE MR0175/ISO 15156-3:2015 EN 10088-4:2009 NORSOK Standard M-630, Ed 6, MDS D55, Rev 5 EN ISO 9445-2
Buyer, Besteller, Acheteur Sverdrup Steel AS Strandsvingen 2 NO 4032, Stavanger NORWAY	
Consignee, Empfänger, Lieu de livraison Sverdrup Steel AS	

Mark of Manufacturer Zeichen des Lieferanten Signe de producteur 	Process Erzählungsart Mode de fusion E+AOD	Inspector's stamp Zeichen des Sachverständigen Poinçon de l'expert 	Grade, Werkstoff, Marke Outokumpu Forta SDX 2507 UNS S32750 1.4410
--	---	--	---

Product, Erzeugnis, Produit
Stainless Steel Cold Rolled, Coil-Plate
finish 2E, pickled, cut edge

Line Reihe Ligne	Item Position Poste	Heat-Lot No Schmelz-Lot Nr Coulée n° - Lot No	Size Abmessungen Dimensions	Pieces Stückzahl Nombre	Quantity / Unit Menge / Einheit Quantité / Unité
1	4	570167-005	3,00 x 1500 x 3000 mm	19	2022 kg

Chemical composition - Chemische Zusammensetzung - Composition chimique

Heat	C	Si	Mn	P	S	Cr	Ni	Mo	Cu	N
	.017	.38	.75	.029	.001	25.02	6.87	3.79	.27	.276

Radioactive contamination check acc. IAEA recommendations: Approved

Test results - Prüfergebnisse - Résultats des essais (1N/mm² = 1 MPa) F = Front - Anfan - Début B = Back - Ende - Fin T = Transverse - Quer - Travers

Test Ref	Temp	RP 0.2	RP 1.0	RM	A5	2"	HB	FEB
	°C	N/mm²	N/mm²	N/mm²	%	%	HB	%
Min	+20	550		795	25	15		35.0
Max				1000			310	55.0
F T	+20	720	802	917	34	32	270	50.0
B T		729	801	912	33	32	270	46.0

Corrosion acc. EN ISO 3851-2C: Approved
Material conforms to NACE MR0175/ISO 15156 in supplied condition
PREN: Cr + 3,3Mo + 16N = 41.9
Heat treatment / Solution annealed: Material temp minimum 1160 °C / Quenched (forced air + water)
All supplied items fulfill the heat treatment requirements, including time, temperature and speed, acc. to the qualified procedure
QTR No: 2507 - 2014
Corrosion acc. ASTM G 48-A 50 °C - 24H: Approved
Intermetallic phases and/or precipitates acc. to NORSOK MDS D55 Rev. 5: No indications
Steel grade verification (PIM-spectroscopic): Approved
Marking, visual insp. and gauge measurement: Approved
Certified acc. Pressure Equipment Directive (2014/68/EU) by TÜV CERT-Certification body for pressure equipment of the TÜV NORD Systems; notified body, reg-no. 0045.
Microstructure acc to ASTM A 923-A: Approved

Outokumpu Stainless AB
Business Unit Special Coil
BOX 74, S-774 22 AVESTA
SWEDEN
Regioffice: Stockholm SWEDEN, Regno: 056001-6748

Telephone: + 46 (0)226 811 73
Fac: + 46 (0)226 816 46
V.A.T no: SE596001674801

This material is found to comply with order requirements

Jakob Johansson
Authorized Inspector



Appendix G

Datasheet for Al-Anodes

TECHNICAL DATA

CORAL[®] 'A' **HIGH GRADE**

Al-In-Zn alloy

Chemical composition according to NORSOK specification no. M-503, rev. 2 and certified according to DNV Type Approval program, IOD-90-TAI, November 1982.

The chemical composition and performance data of CORAL[®] 'A' High Grade alloy are as follows:

Elements

Analysis (% by weight)

Zn	3,5 – 5,0
In	0,015 – 0,025
Cu	max. 0,003
Fe	max. 0,09
Si	max. 0,10
Others (each)	max. 0,020
Al	Remainder

Specific gravity

2,78 kg/dm³ (theoretically)

Performance data in ambient sea water

Capacity	2585 Ah/kg
Consumption rate	3,39 kg/A.yr
Closed circuit potential	-1,09 volt v.s. Ag/AgCl/sea water

Performance data in sea bottom sediments (mud)

	<u>0-20°C</u>	<u>40°C</u>	<u>60°C</u>	<u>80°C</u>
Capacity (Ah/kg)	2400	1750	1150	600
Consumption rate (kg/A.yr)	3,65	5,00	7,62	14,6
Closed circuit potential (volt v.s. Ag/AgCl/sea water)	-1,05	-1,03	-1,01	-1,00

VERSION 1/03 – SKARPENORD CORROSION a.s, NORWAY